2007

# Using power spectra to look for anisotropies in ultra-high energy cosmic ray distributions

Megan Alicia McEwen
*Louisiana State University and Agricultural and Mechanical College*

# USING POWER SPECTRA TO LOOK FOR ANISOTROPIES IN ULTRA-HIGH ENERGY COSMIC RAY DISTRIBUTIONS

A Dissertation

Submitted to the Graduate Faculty of the
Louisiana State University and
Agricultural and Mechanical College
in partial fulfillment of the
requirements for the degree of
Doctor of Philosophy

in

The Department of Physics and Astronomy

by
Megan McEwen
B. Arts, Columbia College, Columbia University, New York, NY, 1999
December, 2007

*To my amazing husband, Tom.*

# Acknowledgments

I am very grateful to my loving and supportive family, to coffee vendors everywhere, and to Wade for making me a cubicle.

# Preface

The work presented in this thesis has been done during the period from August, 2003 till June, 2007 at the Department of Physics and Astronomy, Louisiana State University, under the supervision of Dr. James Matthews.

This thesis contains work on the experimental study of ultra-high energy comic rays (UHECR). In Chapter 1, I give the general introduction to this subject, giving an outline both of the general study of cosmic rays, and of the work done in this thesis. In Chapter 2, I give the general history of the study of cosmic rays, including a discussion of possible methods of acceleration. In Chapter 3, I introduce the Pierre Auger Obvservatory (PAO), the data from which will be analyzed in this work. Chapters 4-5 cover the research done for my major work–submitted to Astroparticle Physics in June, 2007–as well as the modeling done for two talks given to the PAO during its semiannual meetings in March and November, 2006.

- M. McEwen Angular Power Spectra of Ultra-High Energy Cosmic Rays Traveling Through The Galactic Magnetic Field Astropart. Physics
- M. McEwen "C(l) Signatures of Galactic Magnetic Field Clustering" Malargue, Argentina (2006).
- M. McEwen "Computing C(l) Values for Full- and Half-Sky Exposures" Malargue, Argentina (2006).

Ultra-high energy cosmic rays are still a mystery today. As the largest cosmic ray detector ever constructed, the PAO hopes to increase the statistics, thereby

providing us with more information as to their origins and compositions. Chapter 6 shows a method of weighting possible source distributions after taking particle trajectories' bending through magnetic fields into account. These weighted distributions can then yield angular power spectra which can be easily compared to the data obtained by the PAO. These spectra contain valuable information about the anisotropy of observed distributions, and comparing the data's spectrum signatures to that of possible sources can help solve the mystery of where UHECR come from.

# Table of Contents

# List of Figures

# Abstract

The origins and compositions of ultra-high energy cosmic rays (UHECR) remain a mystery to this day. The Pierre Auger Observatory (PAO) is being constructed now in the hopes that it will help solve this mystery by detecting more UHECR than any previous experiment. In this dissertation, I will discuss this experiment, and analyze the data collected so far by comparing it with simulated data from possible source distributions. In these simulations, I will track antiprotons, along with other possible cosmic ray primaries, through various models of galactic and extragalactic magnetic fields. Once they reach a certain distance, I will record their positions on the sky. These final positions will determine the weight of that position on the sky. This weight will then be applied to possible source distributions, and the particles will be reinjected back to the earth's surface, and the simulated arrival directions will be analyzed. I will be using the method of calculating spherical harmonics coefficients to analyze the data. The method of using these angular power spectra is an attempt to provide a common language for model builders and experimentalists. Anisotropies of any size are easily detected using these coefficients, making them an ideal way to look at observed events that might not be coming from single, point sources. I will compare the results of this analysis with data obtained by the PAO by calculating spherical harmonics coefficients. After comparing the events collected to date by the PAO with three possible source distributions–isotropic, Active Galactic Nuclei, and nearby galaxies–I have observed that the data looks consistent with either nearby galaxies or AGNs as

sources. However, there does exist an extra dipole moment inherent to a half-sky exposure, such as the PAO currently has, which adds in an uncertainty that fundamentally limits the capabilities of large-scale anisotropy analysis. In the absence of clear point-like sources, construction of a detector in the Northern hemisphere will be necessary in order to know the origins of UHECRs with any confidence.

# Chapter 1: Introduction

## 1.1 Introduction to the Dissertation

Although discovered generations ago, the origins and nature of cosmic rays remain mysterious. The mechanisms by which they are formed, along with their exact origins, have proven difficult to pin down. Part of the problem in determining the latter stems from the lack of an exact knowledge of both the galactic magnetic field (GMF) and extragalactic magnetic field (EGMF), which cause the trajectories of charged particles to curve. The highest energy cosmic rays are extremely rare, detectable at earth at a rate only of the order of $\mathrm{km}^{-2}\mathrm{century}^{-1}$. The so-called GZK effect, first pointed out by Greisen [1], and by Zatsepin and Kuzmin[2], limits the distances at which these particles can travel. At energies above about $3 \times 10^{19}$ eV, protons begin to interact with the cosmic microwave background (CMB) in reactions such as

$$p + \gamma_{CMB} \rightarrow \pi^0 + p \tag{1.1}$$

Heavier nuclei also experience severe losses due to photodisintegration at similar energy thresholds. The result is that unless cosmic ray particles originate within d $\sim$ 50 Mpc, the flux at ultra high energies should be greatly suppressed. The fact that they have been observed, without an obvious source within 50 Mpc, underlines the importance of and interest in collecting sufficient statistics to study their arrival directions more effectively.

Furthermore, the distribution of arrival directions thus far recorded appears to be isotropic. Since there has yet to be collected a statistically compelling number of events at the highest energy, however, this apparent isotropy could be misleading [3][25]. We can estimate the angular deflection *observed* at earth of a proton traveling through a constant magnetic field as

$$\sin\theta \approx \theta = 2.7^\circ \, \frac{L_{\mathrm{kpc}} B_{\mu\mathrm{G}}}{E_{19}} = 2.7^\circ \, \frac{L_{\mathrm{Mpc}} B_{\mathrm{nG}}}{E_{19}}. \tag{1.2}$$

where $E_{19}$ is the energy in units of $10^{19}$e, $L$ is the straight-line distance to the source in units of either kpc or Mpc, and $B$ is the magnetic field strength either in $\mu$G or nG units. Estimates of extra-Galactic fields are often around $10^{-12}$G ($B_{\mathrm{nG}} = 0.001$)[5]. The deflection from the Galactic field therefore is probably much larger than that from extra-Galactic fields, for sources within the GZK-survival radius of about 50 Mpc. But extra-Galactic fields are very poorly known. If they are significantly stronger, or if there are regions with stronger fields, then the deflections due to the EGMF may be much greater than anticipated.

Since the deflection within the Milky Way Galaxy (MWG) is relatively small at these energies, and because we don't see multiple, uniform possible sources in the sky, the question of what produced them initially becomes more difficult to answer. For ultra-high energy particles (UHECRs), we can expect an almost direct arrow to their origins. For the purpose of this analysis, we will assume that the primary UHECR particles are protons, electrons, gamma rays, or iron nuclei, though, in reality, the chemical composition of the primaries is uncertain. We will concentrate only on the GMF deflecting the particles in question. The aim of this work is to provide a technique by which to evaluate the anisotropy of a distribution of arrival directions in order to compare to expectations based on some assumed source distributions, magnetic fields, and energies.

On of the biggest obstacles to the study of UHECR has traditionally been their

low flux. Occuring only in amounts $\simeq$ a few handfuls km$^{-1}$ century$^{-1}$, there have only been a very small number of events recorded by experiments to date. Proposed to be the largest cosmic ray detector ever built, the Pierre Auger Observatory (PAO) was created to solve this problem. Spanning 3000 km$^2$ in both the Southern and Northern hemispheres upon completion, the PAO will use two methods of detection to harness information about these elusive particles. 1600 surface detectors (SDs) will process extensive air showers (EAS) incident upon the ground, while 4 fluorescence detectors (FDs) will look over the SD array, searching for the nitrogen fluorescence in the atmosphere inherent to EAS. These two methods will act as an internal cross-check for event detection and calibration. Once fully functional, the PAO will offer a brand new way to look at UHECR, and quite possibly the best statistics by which to do so.

In order to evaluate the anisotropies in the distributions detected and simulated, we have calculated their angular power spectra. This method of analysis [6] is based on the simple fact that any distribution of discrete points on a sphere can be represented by a sum of spherical harmonics. The intensity of these events can then be shown to be:

$$I(\theta,\phi) = \sum_{\ell=1}^{\infty} \sum_{m=-\ell}^{\ell} a_{\ell m} Y_{\ell m}(\theta,\phi)$$

where the coefficients $a_{\ell m}$ are obtained from the observed intensity by

$$a_{\ell m} = \int I(\theta,\phi) Y_{lm}(\theta,\phi) d\Omega$$

The angular power spectrum, or $C_l$ values, is represented by taking the average of the spherical harmonics' coeffecients mentioned above.

$$C_l = \frac{1}{2l+1} \sum_{m=-l}^{l} a_{lm}^2$$

We can use the values of $C_l$ to determine not only whether or not anisotropy exists

in any given collection of points, but also the scale of it. The values of $C_l$ are sensitive to variations over angular scales of about $1/l$ radians. Therefore, by studying which $C_l$ values are heightened or suppressed in a given distribution, we can determine what kind of anisotropy we're looking at, whether it be a large-scale dipole or small-scale clustering. As such, this is a powerful analysis tool for large-scale searches for anisotropy.

In order to trace the particles, we will use the method of reverse trajectory, by which we will inject anti-protons from the earth's surface through a magnetic field model, then record their final positions on a spherical shell of a given radius. These final positions will be evaluated to "weight" the initial distribution, and the particles will be assigned these weights. Once properly weighted, the particles will be reinjected to the earth's surface, and their $C_l$ values will be recorded. We will do this for three source distributions: (i) isotropic sources, (ii) AGNs as sources, and (iii) nearby galaxies as sources.

After evaluating the anisotropies of these various source distributions, we will then compare the results to the data thus far obtained by the Pierre Auger Observatory. By comparing signatures of the $C_l$ values, we will then draw conclusions about the primary particles likely causing the extensive air showers, the most thorough method of detecting them, and their most likely sources.

# Chapter 2: The History of Cosmic Rays

## 2.1 Introduction

In 1912, Victor Hess [26] discovered, through a series of balloon flights, cosmic radiation. Because the radiation increased with altitude, he concluded that the source of the radiation must be extraterrestrial. And so, the study of cosmic rays was born.

## 2.2 Cosmic Ray Discoveries

Because of the high energies of these cosmic rays, early particle physicists were able to make new and exciting advances. There are forces in the galaxy accelerating particles to energies unattainable by earth-bound accelerators. As a result, these high energy particles hitting the earth became the ”fathers” of as-yet undiscovered, short-lived, and exotic particles. For instance, Dirac proposed the idea of an anti-electron, or positron. He postulated that there exists a sea of electrons with negative energy states and that, if an electron leaves said sea, there will be a hole. This hole will correspond to a positively-charged particle with the same mass as an electron, or a positron. This theory was proven, however, by Anderson in 1931 [8], who did so using cosmic rays. Anderson and Hess later shared the 1936 Nobel Prize for their research.

Likewise, Yukawa proposed the existence of a particle associated with the

strong nuclear force. However, two groups studying cosmic rays thought they had found the particle first. Both Anderson/Neddermeyer and Street/Stevenson [9] announced the discovery of the particle in 1937. However, in 1947 it was proven that there are actually two particles with similar masses associated with the strong nuclear force, and that both abound in cosmic ray air showers: the muon and the pion. The pion turned out to be the particle Yukawa had proposed over a decade earlier.

In December of 1947, a completely different particle was discovered through cosmic ray research. It had more than double the mass of pions and behaved very differently from any previously discovered particles. It was called the kaon, and was the first in a series of similar discoveries of particles produced on a short time scale (lifetime is around $10^{-23}$ s.), but decayed relatively slowly (at around $10^{-10}$ s.). These particles were all created using the strong nuclear force, but decayed through weak nuclear interactions. Because of the odd behavior, they were dubbed the ”strange” particles. And so the idea of ”strangeness” (and, later, strange quarks) was born.

This potential for studying high energy particles without having to generate them, along with this ground-breaking research in particle physics, fueled the interest in cosmic rays. Obviously, the study of cosmic rays was worthwhile; the difficulty in it lay in detecting these high energy particles. Direct detection is possible for particles with energies up to 1-10 TeV. This detection is done through high altitude detectors (such as balloons), and is relatively easier than detecting higher energy particles since the flux of the radiation is much higher at lower energies. Because flux is dependent both on intensity of radiation and size of detector, then, one can detect a high number of lower energy cosmic rays using a fairly small detector. Though the intensity of the radiation is always dropping, above around 1000 TeV it drops more drastically; the only option left is to increase the size of the detector. In 1938, Pierre Auger made a ground-breaking discovery

which would enable the study of cosmic rays to grow [10]: He recorded coincidences in arrays of particle counters. In other words, he and his group were able to record multiple counter coincidences at the same altitude while using electronics with microsecond timing. From this, he deduced that these coincidences must be due to a sort of pancake of particles arriving at the detectors simultaneously, and the idea of the extensive air shower (EAS) was born. These EAS's are caused by high energy cosmic rays interacting with the atmosphere. These interactions cause a cascade of particles to fall to the earth's surface at the same time, in the sort of "pancake" shape predicted. From electromagnetic cascade theory, he deduced that the energies of these particles must be around $10^{15}$ eV.

In 1953, Bassi et. al. [11] used timing information from arrays of scintillation detectors to reconstruct the original direction of the cosmic ray. This provided, then, a direct link between the observed shower at the earth's surface and the cosmic ray incident on the atmosphere. In 1962, Suga and Chudakov said that the atmosphere, then, could be used as a large scintillator for air shower detection, which would yield more information about high energy particles that had been difficult to study before. Consequently, in 1963, Linsley [12] used the Volcano Ranch array to report the first $10^{20}$ eV cosmic ray. This energy corresponds to about 16 Joules of energy packed into one nucleus. Five years later, Tanahashi detected an air shower with an incident cosmic ray of the energy $10^{19}$ eV using a different method: fluorescence in the atmosphere [13]. Volcano Ranch also recorded a fluorescence event later, which coincided with an event detected by the ground array [14]. This was the first "hybrid" event: an event recorded by two different methods of detection at the same time and at the same location. This is the technique that the Pierre Auger Observatory–named for the father of air shower detection–will implement.

## 2.3 Cosmic Ray Physics

Even though the study of cosmic rays is 100 years old, the most fundamental questions about them have yet to be answered. What they are and where they come from is still not entirely known. To put the former problem in a more technical manner, the chemical composition and energy spectrum of these particles is still an open question at energies $\geq 10^{15}$ eV, at the so-called "knee" of the spectrum, which is clearly illustrated in Figure 2.1.

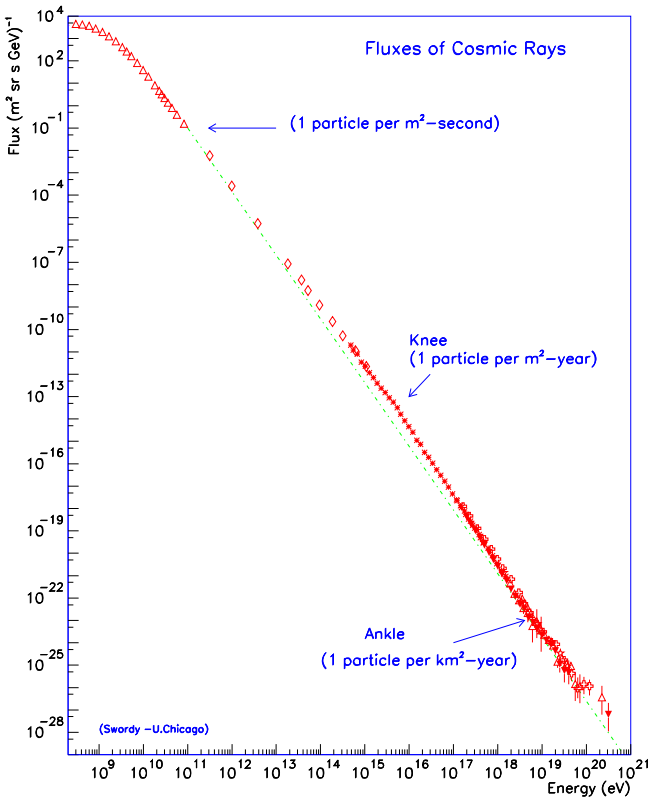


Figure 2.1: Cosmic Ray Spectrum. Figure from [15]

The latter is also an interesting question, since the manner of these particles' acceleration through space, as well as their initial creation, is still somewhat a mystery. Finally, the study of the distribution of cosmic rays observed at the earth's surface, along with the study of the distribution of cosmic ray sources, can

tell us about the magnetic fields encountered by these particles, as well as giving us more information about their acceleration to the earth's surface.

Obviously, each of these areas of study are interdependent on one another. The source of a cosmic ray is related to its chemical composition, the manner of acceleration is related to the final energy spectrum, and the distribution of particles once they arrive at the earth's surface is necessarily related to both the composition and the energy. For example, if the particle at the earth were "pointing" directly back to its source, we would know it is a neutral particle, and is therefore unaffected by the extragalactic magnetic field (EGMF) or the galactic magnetic field (GMF). To use another example, if the particles are discovered to be heavy nuclei, the source must be something that would have both access to heavy nuclei and the capability to accelerate them to fantastic energies.

The energy spectrum contains much information necessary to form any conclusions about the cosmic rays observed at the earth's surface, as well as their propagation thereto. Overall, the power spectrum appears to follow a basic power law, but has two major signatures: the "knee," which occurs at around $10^{15}$ eV, and the "ankle," which occurs at around $10^{18}$ eV. Obviously, then, the sources in question must generate a power law spectrum. The two signatures, however, imply significant departures from that spectrum that could be due to differences in chemical composition, location of sources, or both. The energy density has been calculated to be $1eV/cm^3$, while the energy density of starlight and GMF's are around $0.6eV/cm^3$ and $0.2eV/cm^3$, respectively [16]. This calculation shows, then, that these cosmic rays must be non-thermal, due to the large amount of energy that would be required. They must, therefore, be either accelerated or created.

## 2.4 Composition

Between 0.1 - 100 TeV, direct detection of cosmic rays can yield valuable information about their composition. This detection is done through spectrometers and calorimeters, and they measure the composition of these lower energy cosmic rays to be about 50% protons, 25% alpha particles, 13% CNO, and 13% iron nuclei. If compared in more detail to the solar system abundances known, it can be seen that cosmic rays are deficient in H and He, though why this is has yet to be fully understood. Two possible reasons are that heavy elements are easier to ionize and accelerate, or that the source composition is reflected by the cosmic rays coming from it. Li, Be, B, Sc, Ti, V, Cr, and Mn are all over-abundant, however, given our models. This is easier to understand, given the spallation of C and O for the first group (Li, Be, and B) and Fe spallation for the second (Sc, Ti, etc.).

At higher energies, the flux is too low to measure composition directly. Therefore, indirect measurements must suffice. These measurements are done through ground arrays and fluorescence detectors, as said previously. A commonly used method for composition studies is by using the depth of shower maximum ($X_{max}$) as measured by fluorescence detectors, which is related directly to the primary composition of cosmic rays. Using data from the HiRes detector, measured $X_{max}$ data has been compared to simulated $X_{max}$ values for protons and iron nuclei using different hadronic models [17]. The data seems to point to a mixed composition of these high energy cosmic rays, with a tendency toward lighter nuclei for the highest energies.

## 2.5 Sources

The sources of cosmic rays, especially the highest energy ones, are still a mystery. One possibility is that cosmic rays are protons or nuclei which are then acceler-

ated up to their observed energies by the source itself. Such a possibility is called a "bottom-up" method. Another possibility is that the cosmic rays are created at these energies in the first place, either from the decays of super heavy dark matter or by massive particles released by topological defects or some other exotic phenomenon. These theories are known as top-down models. I will be focusing on the former model for this chapter, or the bottom-up models.

Particle acceleration can occur in one of two ways: directly, or through a statistical process. Direct acceleration occurs through a strong electromagnetic field, for example, if there exists a strong rotating magnetic field which results in a large electromotive force, or EMF. This force both, then, traps the particle and accelerates it to high energies. However, this method of acceleration does not yield a power law energy spectrum, and also necessarily occurs in regions of high matter or radiation density in space where energy losses could occur quickly. Where optical photons are dense, meson photoproduction, photonuclear fission, and pair creation can occur easily, thereby depleting the cosmic rays of their initial energy by the time they reach the earth. This would not only effect the energy spectrum, but would obviously also affect the final composition of the cosmic rays.

Fermi [18] also proposed a so-called statistical acceleration process. In this process, the build-up of energy is slow and takes place over a long period of time. It takes place in collisions with magnetic clouds or in shockwaves from supernovae, active galactic nuclei (AGN's), or gamma-ray bursts (GRB's). This process would force a power law spectrum, as opposed to the direct acceleration model.

Collisions with magnetic clouds, as originally proposed by Fermi, accelerate particles through repeated collisions with plasmas. During these collisions, the particles can either gain or lose energy. Since the acceleration goes as the square of the velocity of the magnetic cloud ($\delta$ E/E = $\beta^2$), the process is known as second-order Fermi acceleration. It is a slow process, and the energy loss (mainly caused by the radiation generated when the particles' trajectories bend) is large for slow

particles. This makes it difficult to efficiently accelerate particles to the observed energies.

Shockwave acceleration is much more efficient as an acceleration mechanism. This type of acceleration is linear with the speed of the shockwave ($\delta$ E/E = $\beta$), and is therefore known as first-order Fermi acceleration. Since it is a linear relation, particles can be accelerated more quickly than in the second-order case. As a shockwave passes through gas or dust, it creates a density gradient at the shock front. This then creates kinetic energy in the medium, and there will be a resulting net motion as the wave passes. The particles can diffuse and randomly travel through the medium, in which they will have a probability to hit the shock front and be accelerated. They could then back-scatter downstream, thereby passing the shock front again and gaining more energy. This acceleration will continue until the energy losses match the energy gains. This stop-time will depend on ambient conditions. The final results will be a power law spectrum for the particles emerging from the shock front.

In a paper by Drury [19], it was shown that the maximum energy attainable through this type of diffusive shock acceleration is:

$$E = kZeBR\beta c \tag{2.1}$$

where B is the magnetic field of the shockwave, R is the size of the shock region, $\beta$c is the shock speed, and k is an efficiency factor, related to efficiency. For example, in the case where the acceleration is limited by the age of the shock (and not the particle's escape from the region), k = 3/20. If one assumes $k = \beta = 1$, optimal acceleration is reached. This would lead to the equation of highest possible attainable energy, given R and its associated B:

$$E = 0.9ZBR \tag{2.2}$$

where E is expressed in EeV, B is in $\mu$G, and R is in kpc. Given these equations, we can estimate the conditions necessary to accelerate a given particle to a certain energy.

Obviously, there are only a few objects capable of accelerating cosmic rays to the highest energies that have been observed. Another difficulty in figuring out the sources of these particles is that the objects capable of this sort of acceleration are located far away from the earth. During a particle's trip from one of these objects, it would necessarily interact with the cosmic microwave background radiation (CMBR), and would lose its high energy before we observed it. Also, charged particles would be bent in the EGMF (and GMF), thereby making the source identification more difficult.

## 2.6 Propagation

Particles traveling through space to reach the earth will definitely interact with the CMBR, but may also interact with other ambient radiation, dust, or gases. These interactions would change both the composition and the energy of the observed cosmic rays. For example, assuming the cosmic ray is a heavy nucleus, such as iron, there is a probability that the nucleus will photodisintegrate or pair create on the CMBR as follows:

$$A + \gamma_{2.7K} \rightarrow (A-1) + N \tag{2.3}$$

$$A + \gamma_{2.7K} \rightarrow (A-2) + 2N \tag{2.4}$$

$$A + \gamma_{2.7K} \rightarrow A + e^{+} + e^{-} \tag{2.5}$$

Each of these interactions would lessen the energy of the observed particle. Also, the nucleus may interact with the infrared photon background, although

this is only important for primary cosmic rays with energies less than $5 \times 10^{19}$ eV. The interaction of the particle with the CMBR (and its subsequent energy loss) is more important for energies above $5 \times 10^{19}$ eV [20]. Energy loss due to pair creation is dominant in the energy range in between these two values. For example, the typical attenuation length for Fe and Si in the aforementioned energy range (i.e. between 40-100 EeV) is between 10 - $10^3$ Mpc [21]. This attenuation length is comparable to that of nucleons at around the same energy. This results in an observed energy spectrum that differs from the energy spectrum at the source, since it would contain features due to the aforementioned interactions, and would also contain fewer high energy particles than were originally created. We would also observe more light nuclei than existed originally at the source.

Shortly after the discovery of the CMBR, Greisen [**?**], Zatsepin, and Kuz'min [**?**] first computed an actual cutoff for protons undergoing such interactions with the CMBR, named the GZK cutoff. For instance, a particle of energy $5 \times 10^{19}$ eV will "see" a CMBR photon as a 300 MeV photon, which means it would exist at the threshold for photopion production. The temperature of the CMBR is 2.74 K [22](corresponding to an energy of $2.36 \times 10^{-4}$ eV), the threshold energy becomes about $10^{20}$ eV for protons to undergo the following interaction:

$$p + \gamma_{2.7K} \rightarrow \Delta^+ \rightarrow N + \pi^+ \tag{2.6}$$

$$p + \gamma_{2.7K} \rightarrow \Delta^+ \rightarrow p + \pi^0 \tag{2.7}$$

Assuming the cross-section for the delta resonance to be $10^{-28}$ cm$^{-2}$, and the photon density to be $420(1 + z^3)$cm$^{-3}$, the mean free path for this interaction is around 8 Mpc. In each interaction, the proton will lose about 20% of its energy. After a certain distance, the energy of the proton will decrease to an energy below the delta resonance threshold no matter what its original energy was at the source.

At lower energies, protons can also pair create with the CMBR as:

$$p + \gamma_{2.7K} \rightarrow p + e^{+} + e^{-} \tag{2.8}$$

This effect is smaller, since the energy loss per interaction is much smaller than the previously discussed interaction. Still, it may contribute to the shape of the final observed energy spectrum below the GZK cutoff if the primary particles are protons from relatively distant sources.

If the primary cosmic ray is a photon, this pair creating with the CMBR will be the dominant form of energy loss. Above $4 \times 10^{14}$ eV, this attenuation due to pair creation is important, whereas attenuation due to pair creation with the radio background dominates energy losses above $2 \times 10^{19}$ eV [23]. The attenuation length for photons with an energy of about $10^{20}$ eV is 10-40 Mpc, depending on the radio background photon density.

## 2.7 Extensive Air Showers

Once the cosmic ray reaches the earth, the method of detection depends on the energy of the incident particle. For low energies, 0.1-100 TeV, direct detection methods can be used due to the comparatively large flux of these particles. Once higher energies are reached, though, the flux decreases markedly, and the detection of the particles is better accomplished by looking for the extensive air showers which occur when the cosmic ray interacts with the molecules in the atmosphere. The resultant air shower can be observed through the fluorescence caused by electrons and positrons exciting the nitrogen in the atmosphere, or by measuring the shower particles incident upon the ground.

## 2.8 Electromagnetic Cascade

When a cosmic ray enters the atmosphere, it collides with a nitrogen or oxygen nucleus, producing pions as well as the fragments of the original nucleus. Among the pions created, about one third will be neutral pions, which subsequently decay into two so-called "decay" photons. This effect is clearly illustrated in Figure 2.2.

Assuming that an initial photon has an energy $E_0$ and travels a distance R before creating an electon/positron pair, the resulting particle will have an energy of E = $E_0$/2. The electron/positron pair must then travel another distance R before they bremsstrahlung and generate one photon each. This photon will take half the initial energy of the electron or positron. After a distance of nR, finally, there will be $2^n$ particles, each with an energy of $E_0/2^n$. This process will continue until the average energy of the particles is below a critical energy, $E_c$. For electrons and positrons, $E_c$ is the energy where the cross section for bremsstrahlung is smaller than the cross section for ionization. For photons, however, $E_c$ is the energy where Compton scattering is the dominant interaction, rather than pair production.

For high energies, the length for pair production, $\epsilon_o$, is approximately equal to the radiation length for bremsstrahlung. If R is the distance at which the probability of pair production or bremsstrahlung is 1/2, the $R = \epsilon_o/ln2$. The number of distances, then, for the shower to travel in order to reach the maximum number of particles is:

$$N_{max} = \frac{E_0}{E_c}$$

$$X_{max} \propto ln\frac{E_0}{E_c}$$

The depth of the shower maximum ($X_{max}$), or the depth at which the number of charged particles reaches a maximum ($N_{max}$), is proportional to the log of the initial energy, while $N_{max}$ is proportional to the energy of the incident particle.

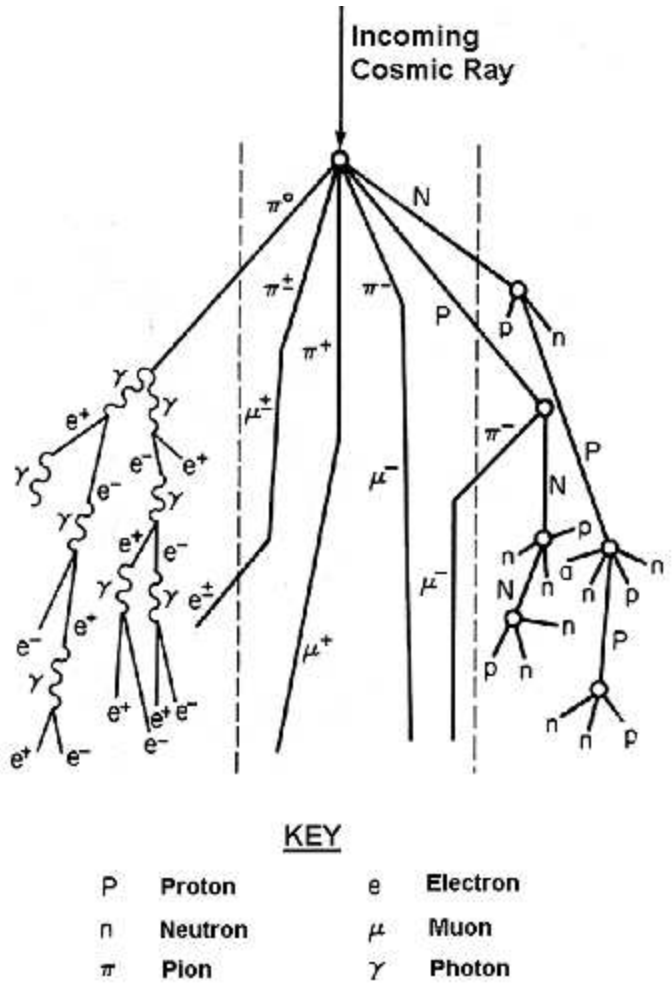


Figure 2.2: Electromagnetic Air Shower

## 2.9 Hadronic Cascade

An extensive air shower initiated by a hadron is just a superposition of electromagnetic cascades from neutral pion decays fed by a hadronic core. In addition to electromagnetic cascades, charged pions will either interact strongly or decay to muons. These decays occur in the region in which the probability to decay is greater than the probability to interact. The majority of the muons which then arrive at the ground detectors are created in the initial stages of the extensive air shower. Deep in the shower development, electrons and positrons are created by

the decay of muons. Therefore, the electromagnetic cascade is not fully attenuated deep in the shower development; it will persist due to the muon decays.

Since the neutral pions are fed by the hadronic core, $X_{max}$ will depend on the hadronic interaction model, as well as the cosmic ray's initial composition. Protons have a longer mean free path (MFP) in the atmosphere than an iron nucleus, for example. Also, since energy is divided amongst nucleons as $E_0$/Z for a cosmic ray of initial energy $E_0$, the average energy per nucleon will be much lower for heavier nuclei than light ones. This will result in a shallower $X_{max}$ for iron than for a proton, but one that will fluctuate less. The study of $X_{max}$, then, is integral to the understanding of the primary cosmic ray composition.

## 2.10 Conclusions

The field of cosmic ray physics has had a distinguished past, present, and a still-evolving future. Many basic questions have yet to be answered definitively, such as the nature of the rays or their sources. The end goal will be to discover the composition of these rays, determine their sources, and define their acceleration methods. The energy spectrum, specifically the knee and ankle thereof, is indicative of the source distribution. Whatever the source of the UHECR's, the fact that their energies exceed the GZK cutoff indicate that they come from nearby. This could mean that there are top-down sources of ultra-high energy cosmic rays, or that there are enormous acceleration mechanisms that have gone undetected so far, located relatively close to Earth.

The method of detecting ultra-high energy cosmic rays depends on the properties of the extensive air showers. Fluorescence detectors depend on the development of the electromagnetic cascade, with the energy of the incident particle being related to $N_{max}$ and the composition related to $X_{max}$. Ground detectors sample the shower at one particular depth, thereby gathering information about the lateral

distribution of the shower's particles. Some of the observables on the ground also relate directly to the energy and composition of the incident cosmic rays.

# Chapter 3: The Pierre Auger Observatory

## 3.1 Introduction

The Pierre Auger Observatory (PAO) has been conceived of as a way to solve the mystery of the origin and nature of ultra-high-energy cosmic rays. The design incorporates two proven measurement techniques: detecting the nitrogen fluorescence generated in the atmosphere by an extensive air shower, as well as measuring the particles that reach the ground. This hybrid technique, as seen in Figure 3.3, of detecting extensive air showers is part of what sets PAO apart.

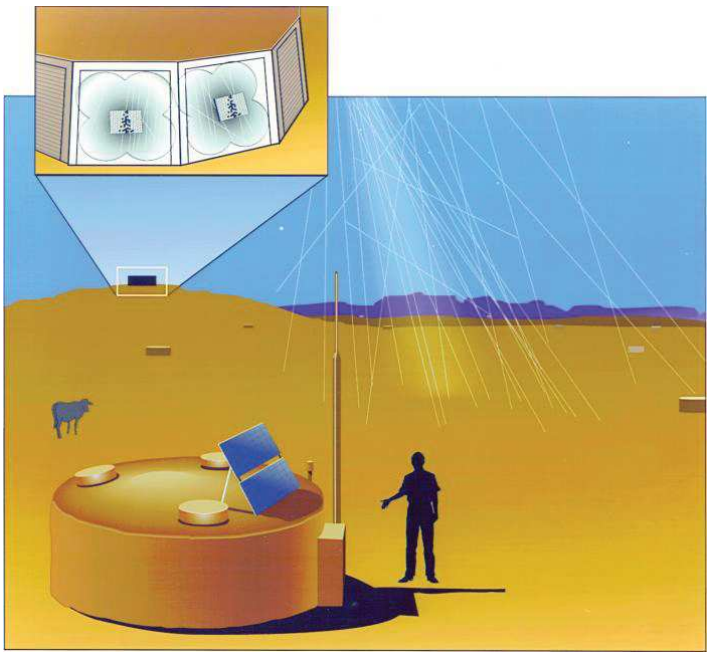

Figure 3.1: Hybrid Nature of PAO Detector

The size of the observatory is also unprecedented [24].

The PAO will have an array of water Cherenkov detectors that will cover 3000 $km^2$ that will encompass 1600 tanks, as seen in the plan in Figure 3.2. . Each will be spaced 1.5 km apart from one another, forming a triangular "cell."

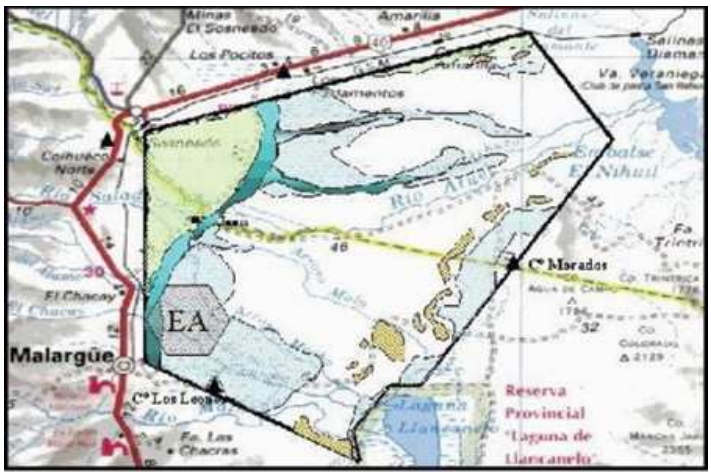


Figure 3.2: Map of Southern PAO Detector

Surrounding the surface detector array will be 4 fluorescence telescopes which will scan the sky directly above the array for the nitrogen fluorescence inherent to extensive air showers passing through the atmosphere. Each will view up to 30 degrees in elevation and 180 degrees in azimuth. The surface detectors (SD's) will operate 24 hours a day, 365 days a year, then, whereas the fluorescence detectors (FDs) can only operate a small fraction of the time, due to their need for clear, moonless nights. Thus, for a small subset ( $\simeq 10\%$) of cosmic rays, the air showers will be recorded with both techniques.

Since each method of detection has systematic errors associated with it, the hybrid nature of the observatory will be valuable in cross-checking estimated energies and arrival directions internally. The hybrid results will also provide more information in determining particle type by comparing results to hadronic interaction models. To use the two types of detectors as cross-checks for one another's errors, we must first understand the systematic errors of each.


Figure 3.3: Hybrid Detector

The fluorescence detector energy measurement relies on the photon yield, or the number of photons fluoresced per unit length for an electron in the electromagnetic air shower (EAS). Any systematic error in this measurement will then propagate to the energy estimate made using fluorescence data. Another possible source of systematic error using fluorescence detectors comes from the need for an accurate determination of atmospheric conditions at the time of a given cosmic ray shower. Since the light that reaches the detector must travel through kilometers of atmosphere, the atmosphere will necessarily attenuate the intensity of the light. The attenuation length must be known to calculate the number of photons created at a given location in the air shower. Without an accurate estimation of atmospheric influence on this attenuation length, the estimate for the energy or arrival direction of the cosmic ray shower could be vastly different than reality.

Another possible source of systematic error lies in calculating the absolute number of photons at the detector. The signal measured from the readout elec-

tronics must be converted into an absolute number of photons at the detector. All of these possible errors are constantly being assessed. The atmospheric monitoring and absolute calibration of the detector will be discussed further in this chapter.

The SD is calibrated by the constant flux of single, uncorrelated muons from low energy showers. Thus, the possible errors described above do not apply to the ground array. However, there are systematic uncertainties in the energy estimates from these surface detectors. These uncertainties arise mainly from the unknown composition of the cosmic ray and hadronic models used in the Monte Carlo simulations.

The main difference, then, between the uncertainties listed for fluorescence and those for the ground array are that the fluorescence errors may be reduced through careful measurements, while the uncertainty in the composition and hadronic models in the simulations remains regardless of the care taken in calibrating and monitoring the detector. Thus, the two techniques in the PAO have different systematics and different systematic errors. By combining the data from both, we will be able to constrain the problem such that the uncertainties will be minimal.

## 3.2 The Fluorescence Detector

As electrons and positrons pass through the air, they excite the nitrogen in the air, which then fluoresces. We can then study the shower development from this fluorescence by charting it at different atmospheric depths. From this analysis, the depth of shower maximum ($X_{max}$) and the number of charged particles at shower maximum ($N_{max}$) can be calculated. The PAO will have 4 fluorescence detectors (FD) overlooking the SD that will measure these parameters. Since the principal purpose of the FD is to measure the longitudinal profile of the shower development (i.e. $X_{max}$ and $N_{max}$), there is a certain minimum resolution in atmospheric depth

necessary for any useful results to be derived. A resolution of 20 g/$cm^2$ is desirable to distinguish between iron and proton primaries which have a mean $X_{max}$ that differs by $\simeq$100 g/cm$^2$. An energy resolution of 10% is achieved by certain signal to noise measurements which also lead to a 20 g/cm$^2$ resolution

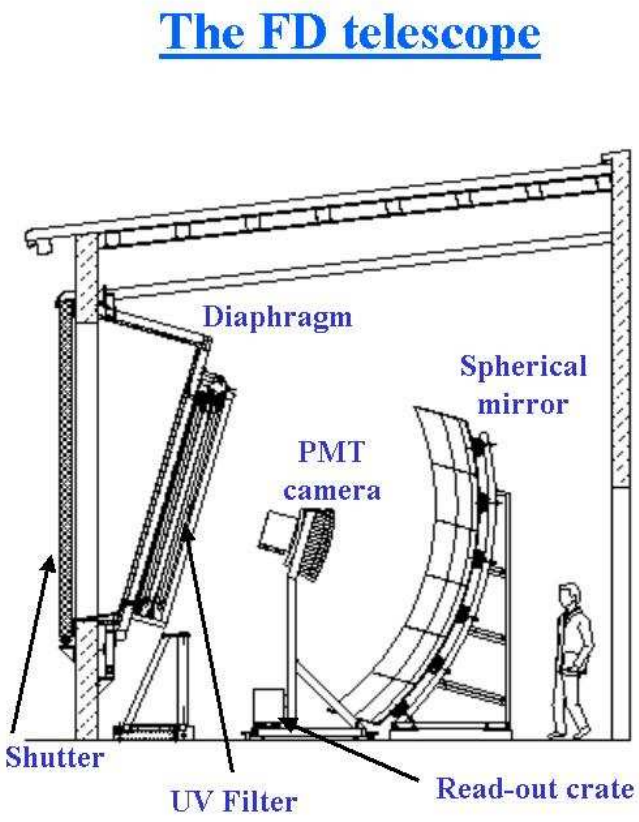


Figure 3.4: Sketch of Fluorescence Detector

The base design of the FD, as seen in Figure 3.4, meets these objectives. Each FD building, or "eye", has six telescopes, each composed of 440 pixels. Each pixel covers a 1.5 degree area of the sky. The pixels are arranged in a 22x20 matrix so that the resulting coverage is 30 degrees in azimuth and 28.6 degrees in elevation. This "fly's eye" design is shown in Figure 3.5. The light detector for each pixel is a hexagonal photomultiplier tube (PMT) that is sampled by a 12-bit ADC every 100 ns.

Figure 3.5: Camera of Fluorescence Detector

There is a data acquisition system at each ”eye” that records all the data from these six cameras and checks to see if the raw pixel information meets certain geometric requirements. If so, a trigger is created. This data is then transferred to a central data acquisition system (CDAS) for the entire observatory that checks for coincidence with the SD (or another FD ”eye”), then builds the events from the trigger data from all the detectors. The design of the telescope is driven by the desire to increase the signal to noise ratio while maintaining good angular resolution. However, due to cost considerations, the pixel size cannot exceed 1.5 degrees. A good geometric reconstruction is necessary to determine correctly the longitudinal profile, which then determines the $X_{max}$ accuracy. Fluorescence light enters the telescope through a 1.1 m radius diaphragm and is collected using a 3.5 m. x 3.5 m. spherical mirror, as seen in Figure 3.6.

Schmidt optics are used to eliminate coma aberration, which is a problem in spherical mirrors covering a large solid angle. Each telescope diaphragm has a UV transparent filter that restricts the incoming light to the range of wavelengths in fluorescent light ($300 \leq \lambda \leq 420$ nm). This filter also reduces night-sky noise.

To correctly determine the size (i.e. number of electrons) of the shower at a

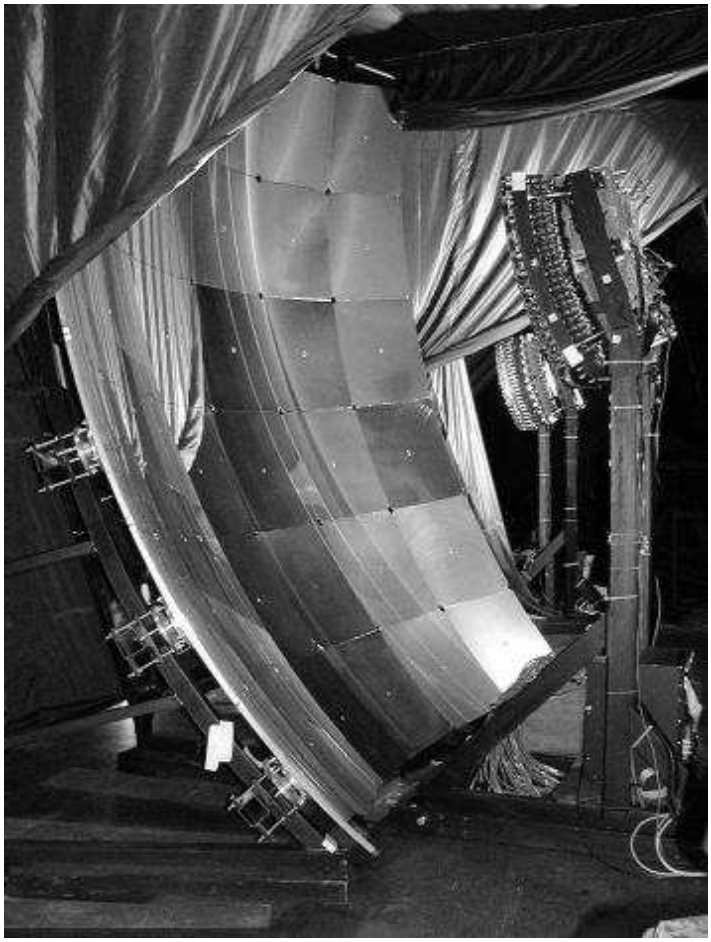

Figure 3.6: Fluorescence Detector

given depth of development, there are several factors that must be accounted for. First, the number of photons emitted per meter via nitrogen fluorescence for an electron that travels through a certain distance in the atmosphere, or the photon yield, must be known. Next, the attenuation of this fluorescent light through scattering in the atmosphere must be measured and corrected for. Finally, the calibration of the detector must be such that for a given pixel the integrated signal can be converted into an absolute number of photons. The photon yield has been measured by independent experiments. We have used those values in our data analysis. The atmosphere must be monitored during data taking to parameterize attenuation lengths and scattering due to aerosols. The absolute calibration of the detector itselfis done 3 or 4 times a year, but there is a relative calibration that

is run nightly to monitor any changes in the system. The absolute calibration of the FD is an end-to-end calibration, in that it accounts for all the components of the system from mirrors to PMTs to the readout electronics. The calibration is done with a diffuse light source that is 2.5 m in diameter and is placed in the aperture of the telescope. The light intensity and uniformity are measured in the lab. The light intensity is measured using NIST-calibrated (National Institute of Standards and Technology) photodiodes while the uniformity is measured using a CCD (charge coupled device) camera. The diffuse light source is able to uniformly illuminate all the pixels in the camera with a known light intensity. Knowing the light intensity at the pixel makes it possible to calculate the conversion from integrated signal to number of photons incident on the pixel. This calibration currently has 12% uncertainties. It is not possible to perform this calibration every night as it is labor and time intensive, and therefore steals valuable time away from observing.

The calibration must be monitored on a nightly basis to track any changes in the performance of the telescopes and correct for these changes in the data analysis. Calibration monitoring is accomplished using an array of LED and a diffuser located at the collector mirrors. Light pulses are fed into the pixels and, at the same time, a portion of the light is directed into a calibrated photodiode to monitor the light source. Correcting for the stability of the LED array, any changes in the response of the optical system (mirror, PMT, and readout) can be monitored on a nightly basis. From the absolute calibration of the optical system in the telescope, there is still a need to correct for the distance the light travels to the telescope, in order to calculate the absolute number of photons emitted at the shower axis.

Atmospheric conditions must be monitored closely, specifically the aerosols in the air and atmospheric depth and temperature profiles. Aerosols can strongly effect the propagation of fluorescence light in the atmosphere. Several methods

are used to characterize the aerosols present in the air at any given time during data taking. Backscatter LIDARs are steerable UV lasers located at each FD eye. Each LIDAR has a PMT that detects the backscattered light from the UV laser pulses. The timing information from the PMT gives information about the aerosol content of the air at any given spot along the path of the laser. This system is able to check various locations and directions in the sky and eventually will be able to "shoot the shower". Every time a large event is recorded by a FD, the LIDAR will shoot laser pulses along the reconstructed track to measure the backscattered light and calculate the attenuation length along the path of the shower. There are also cloud monitors and star monitors to detect clouds and track the stars and any changes in their intensity due to changing atmospheric conditions.

In addition to the aerosol content of the atmosphere, it is important to know the atmospheric depth and temperature profiles. Photon yield has both a small pressure and temperature dependence, which change with altitude. In the past, a parameterized atmosphere was assumed in analyzing data based on the assumption that atmospheric conditions were relatively stable. In Malargue, meteorological radio soundings have been performed as well as monitoring ground based weather stations to understand the atmosphere. Radiosondes are launched with helium balloons above the PAO and data is taken every 20 m in altitude until reaching 25 km above sea level. The profiles are recorded and then compared to the parameterization used previously. If the parameterized values are used instead of the measured profiles, $X_{max}$ values change on average 15 g/cm$^2$ while energy changes less than $1\%$.

A useful tool to cross-check the calibration and atmospheric monitoring is the central laser facility (CLF). The CLF, as indicated by the name, is located in the center of the array. It has a steerable UV laser with an optical fiber that injects a portion of the calibrated, pulsed laser light into a surface detector. The CLF is used to check angular reconstruction, atmospheric conditions, the relative timing

between the SD and FD, and the calibration of the telescopes. The pulsed laser light is scattered by the air and is detected in the FD providing a ”test beam” to cross-check all important quantities in determining the properties of an extensive air shower.

## 3.3 The Surface Detector

The surface detector is made up of 1600 individual particle detectors. Each particle detector is a water Cherenkov detector that is a cylindrical tank with a top area of 10 $m^2$ and a height of 1.5 m, as seen in Figure 3.7. Each detector is completely independent from all other detectors and is driven by two 12 V batteries that are recharged by solar panels. Each detector communicates with the central data acquisition system (CDAS) via a wireless communications system. Thus, when a detector is deployed in the array, it can begin data taking immediately, regardless of the status of other detectors.

The water Cherenkov detector, also called a tank or station, is filled with purified water to a height of 1.2 m, or 12 cubic meters of purified water for each tank. The water is contained within a bag that has a diffuse reflective “Tyvek” bag interior with three windows on top. In these windows sit three 9” PMTs used to detect the Cherenkov light when particles pass through the detector. The signal from each PMT is split into two channels, a high gain and a low gain channel. The high gain channel comes from tapping the last anode in the PMT anode chain and amplifying it by a factor of 40. The low gain channel is the signal straight from the dynode. These signals are then passed through filters and read out by a flash analog to digital converter (FADC) that samples at a rate of 40 MHz. Thus, each station has six signals associated with it, two from each PMT. The relative timing between tanks, as well as the absolute event times for each station, comes from a GPS system located on each tank, and the timing resolution is better than 20 ns.

Figure 3.7: Surface Detector

The design of the station allows detection of a wide range of signal sizes, from a few to around 105 photoelectrons, limited by FADC saturation. It is this dynamic range that allows the calibration of the station to occur using single particles while still detecting, without readout saturation, large extensive air showers that deposit thousands of particles in a station. The dynode to anode ratio of a tank is the ratio of the high gain to low gain signals, and is routinely monitored. It is necessary to measure and monitor this ratio to be able to extend the calibration values, small signals typically, to the detected signals of large air showers. Monitoring this ratio is also necessary for the health of the PMT and readout electronics. Calibrating the stations is accomplished via atmospheric muons. Nature provides these particles at a rate which allows frequent calibration of the stations. Each physics signal is measured in units of vertical equivalent muon (VEM or $Q_{VEM}$), which is the charge deposited by a vertical, through-going (one that does not stop inside the tank) muon in a station. In nature, the muons (and other particles) come from many different directions so the calibration is done by setting a low threshold, 3 PMT coincidence trigger for the station and making a histogram of the charge deposited. The relationship between the peak in the charge histogram ($Q_{peak,VEM}$) and the charge deposited by a vertical through-going muon ($Q_{VEM}$) can

be studied in a reference tank and is expected to vary little between detectors because it is a geometrical factor. Arneodo, et al, performed this study by using a muon telescope as a trigger for the reference tank. They determined the factor to be $Q_{peak,VEM}$ = 1.05 $Q_{VEM}$. Local station triggers are not set using integrated FADC traces because of strict timing requirements. To calculate the sum of a trace would require too many clock cycles on the CPU and would retard the data taking of a station. Thus, local triggers are set using the maximum pulse height in FADC channels. Channels in the FADC are a measure of the photocurrent from the PMTs.

A vertical through-going muon induces a certain maximum photocurrent in the PMTs ($I_{VEM}$), and the trigger is set relative to that value. The procedure is the same as determining $Q_{VEM}$. A histogram is made of maximum pulse heights using a low threshold 3-fold coincidence trigger which is then compared to a histogram of maximum pulse heights for only vertical through-going muons. The relationship between the peak of the pulse height histogram (Ipeak, VEM) and the average maximum pulse height for a VEM ($I_{VEM}$) follows the relationship between $Q_{peak}$, VEM and $Q_{VEM}$. The trigger is set relative to $I_{VEM}$, but it is desirable that this trigger is similar, if not the same, for all stations in the array in units of FADC channels. This is desirable to achieve a similar dynamic range in all the stations and uniform triggering. A similar trigger level is achieved using a rate-based calibration method.

For a given station, the voltages on the PMTs are adjusted so that the rates of events with a peak signal above a threshold are identical. The target rate is approximately 100 Hz and the threshold is 150 channels above baseline. From a reference tank, a 100 Hz rate at 150 channels above baseline corresponds to $I_{VEM}$ being 50 channels above baseline. Requiring that all the PMTs satisfy the above condition, the end to end gains of the PMTs are roughly identical, where the end to end gain means that for an identical energy deposit in a tank, the electronic signal

(i.e. number of FADC channels) is identical. The trigger thresholds are dynamically changed when the station is operating. Changing temperatures, PMT and electronics drifts, or any other effects may change the triggering rate of a station. Assuming, to first order, that the rate of particles hitting the detector is constant, any significant change in the triggering rate can be attributed to changes in the station. To maintain a constant trigger rate, the threshold value for the trigger is changed dynamically, where the changes are on the order of a single FADC channel. This does not effect calibration, however, since absolute physics calibration is done using charge histograms as explained in the previous paragraphs. The changing trigger threshold ensures uniformity in the triggering across the array in that it compensates for any possible changes in the electronics or PMTs that would effect where the $Q_{VEM}$ is determined to be. As long as the individual station triggers are set such that the entire array is triggering on the same physical quantity (related to $Q_{VEM}$), uniform behavior can be expected which simplifies the calculation of important quantities such as the aperture and trigger efficiency. Since the trigger thresholds may change with time, it is necessary to monitor the calibration quantities. Calibration quantities are taken every 3 minutes and are sent back to CDAS every 6 minutes. These values can be monitored for each station in the array. In addition, high statistics ($\simeq$150,000 events) charge histograms are sent back to CDAS with every physics event, providing a method of checking the calibration when doing physics analysis.

## 3.4 Conclusions

The baseline design of the PAO is a hybrid detector for the highest energy cosmic rays. The hybrid technique will provide invaluable cross-checks between the fluorescence detection method and the ground particle detection method for extensive air showers. Each method has inherent systematic uncertainties, but also adds

another dimension of information. Using both detectors together should provide an illuminating look into ultra high energy cosmic rays. The bulk of the data will be taken using the array of surface detectors. A small subset ($\simeq$10%) will be events detected with both the FD and SD. This small subset will be used for determining systematic uncertainties in energy measurements, composition studies, and comparing hadronic interaction models. With these detectors, the puzzles behind the composition and origin of ultrahigh energy cosmic rays will begin to be resolved.

# Chapter 4: Magnetic Fields

## 4.1 Introduction

Observations have established that there exist magnetic fields throughout the known universe. Since cosmic rays can be charged particles, we must be able to understand the magnitudes and directions of these fields so that we can properly simulate the true trajectories of the rays, which must include bending due to magnetic fields encountered. The Extragalactic Magnetic Field (EGMF) is likely much weaker than the Galactic Magnetic Field (GMF), since the GMF exists in an area of much more concentrated matter and charge. However, since the particles travel for up to 50 Mpc, I will model the EGMF as well, in order to ascertain if such a relatively small field can still bend the particles measurably before they reach the galaxy. First, though, I will concentrate on the stronger of the two fields by modeling the GMF.

## 4.2 Galactic Magnetic Field

By looking at the Faraday rotation of the starlight in the galaxy, the GMF's large scale structure has been ascertained [28][5]. The regular component of the GMF can be represented by spiral fields with either a $2\pi$ or $\pi$ symmetries.

These models are called axisymmetric (ASS) or bisymmetric (BSS), respectively [29]. The BSS model is shown in Figure 4.1. The GMF also displays either dipole (A) or quadropole (S) parity across the galactic plane in the z-direction [28].

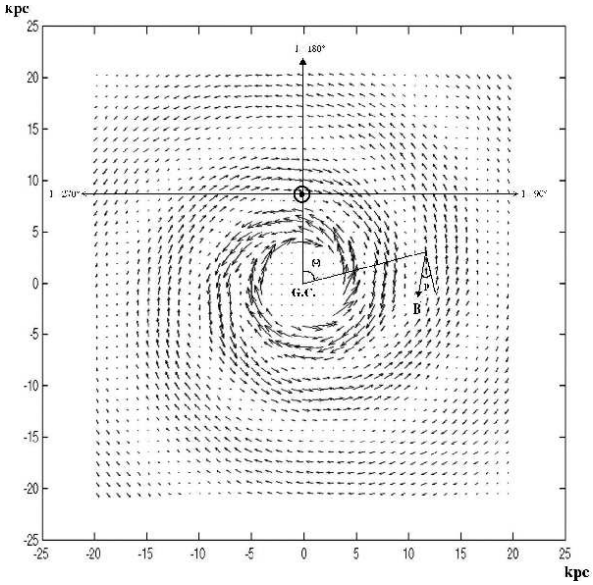


Figure 4.1: Spiral Structure of Galactic Magnetic Field [27]

In the bisymmetric model, at $l = 0^0$, there are two reversals of the GMF inherent to the model. The first occurs at a distance of 0.5 kpc, and the second at $\simeq 3$ kpc [30, 31]. This model of the field has a magnitude in the galactic plane of:

$$B(r, \theta) = B_0(r) cos(\theta - \beta \times ln(\frac{r}{r_0})) \tag{4.1}$$

We, however, have assumed the field to have $2\pi$ symmetry with no field reversals and a quadropole (even) parity across the galactic plane. This model is called the $ASS_S$ model. Therefore, at any point $(r, \theta)$ in the galactic plane, the magnitude of the field is defined to be:

$$B(r, \theta) = B_0(r) |cos(\theta - \beta \times ln(\frac{r}{r_0}))| \tag{4.2}$$

where $\beta$ = $\cot(p)$ = -5.67, where p = the pitch angle = $-10^o$. The r and $\theta$ components of the field are defined in terms of the pitch angle to be:

$$B_r = B(r, \theta) \times sin(p) \tag{4.3}$$

$$B_\theta = B(r,\theta) \times cos(p) \tag{4.4}$$

The GMF has been taken to be on the order or B $\simeq$ 2 $\mu$ G in the direction of galactic longitude (l) = $90^o$ at the solar system, which is at the galactocentric distance of R = 8.5 kpc. We take $r_0$ = 10.55 kpc, which is the galactocentric distance at which the magnetic field is the greatest at l = $0^o$, and $B_0(r)$ = $\frac{3R}{r}\mu G$ . To avoid the formula blowing up at the origin, the magnetic field has been forced constant within r = 4.0 kpc, such that $B_0(r_min)$ = 6.375 $\mu G$ [32].

Above and below the galactic plane, the field falls off exponentially as

$$|B(r,\theta,z)| = |B(r,\theta)|e^{\frac{-z}{z_0}} \tag{4.5}$$

where $z_0$ = 1 kpc for $|z| < 0.5$ kpc, and $z_0$ = 4 kpc for $|z| > 0.5$ kpc [29].

In addition to the above field, we have included a dipole component [33], such that:

$$B(x) = \frac{3.0 m_{gal} \sin(\theta)\cos(\theta)\cos(\phi)}{r^3} \tag{4.6}$$

$$B(y) = \frac{3.0 m_{gal} \sin(\theta)\cos(\theta)\sin(\phi)}{r^3} \tag{4.7}$$

$$B(z) = m_{gal}(\frac{1 - 3.0\sin^2\theta}{r^3}) \tag{4.8}$$

where $m_{gal}$ is the magnetic moment of the galaxy, and is valued at 184 $\mu$G kpc$^3$. The value of the magnetic field, then, is on the order of 0.3 $\mu$G within the solar system.

If we are to compare the effect of the dipole part of the field to the total, we can see the results in Figure 4.2, which was generated by sending a single particle straight into the plane of the galaxy, then tracking it out to 100 kpc. This ratio behaves as we would expect: the particle crosses the magnetic spiral “arms” in the

plane, as is evidenced by the slight squiggles in the plot. As expected also, the total ratio drops by 2 orders of magnitude as we go out from our initial position, at about 10 kpc, to the final, at 100 kpc.

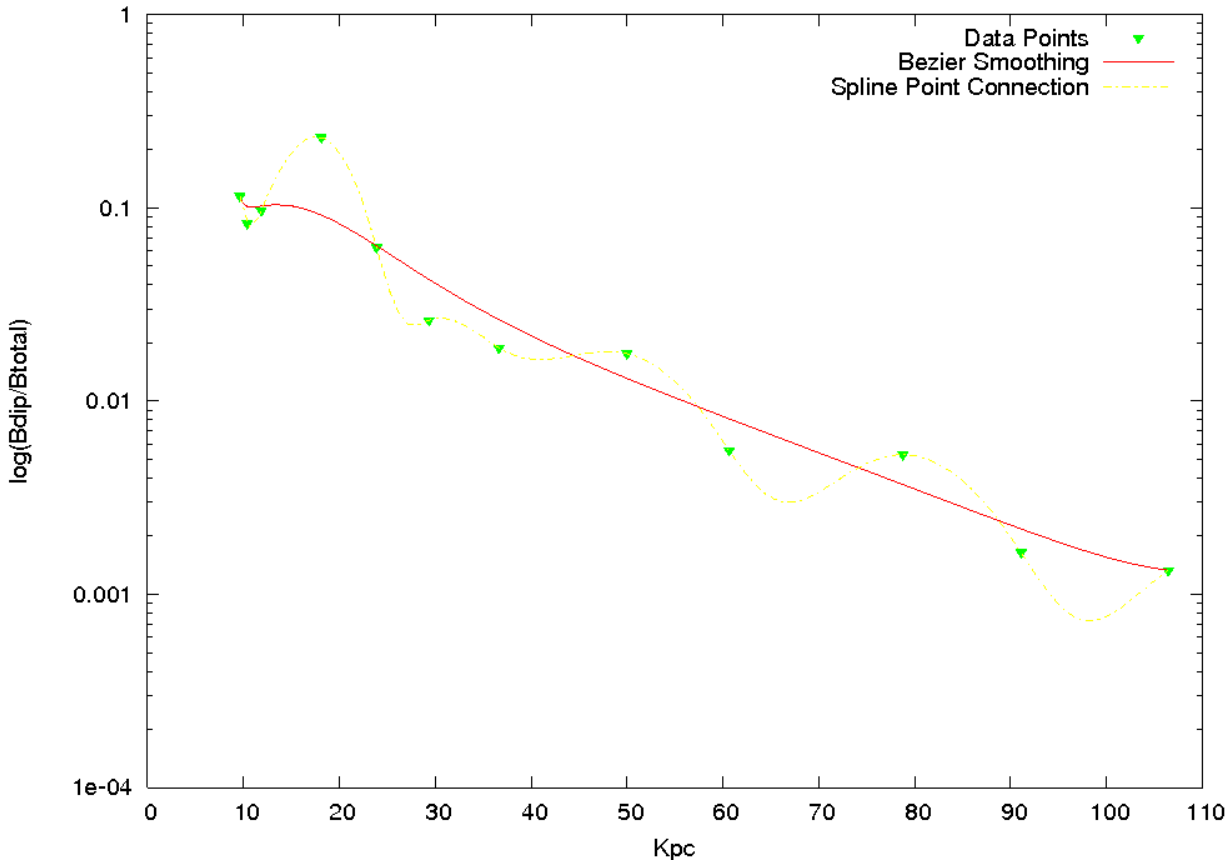


Figure 4.2: Ratio of B(dip)/B(tot)

## 4.3 Extragalactic Magnetic Field

It has been established that magnetic fields permeate the universe. These fields will obviously effect the trajectories of the charged particles therein. However, observations have also established there to be a small-but-pervasive magnetic field existent between the clusters of galaxies. This field could be evidence of a primordial field. This field grows as galaxies form. This growth, along with its omnipresence, begs the question: Could this field be contributing noticeably to the

trajectories of charged UHECR primaries as they travel to Earth?

Philip Kronberg, and others, have set a strict constraint on the large-scale extra-galactic magnetic field (EGMF) [5]. This upper limit is derived by studying the Faraday rotation of light coming to the earth from distant quasars. By studying the variation in the angle of polarization of radio emission of a variable astronomical object with a known frequency, Kronberg was able to set the upper limit of the EGMF to $10^{-9}$ G. There also exist weaker constraints on the EGMF, which are derived from synchrotron emission from nearby galaxy clusters (Kim 1989), as well as that of the cosmic microwave background (CMB), as defined by:

$$\frac{dE}{dt} = -\frac{2e}{3} r_0^2 B^2 \left(\frac{E}{m_e c^2}\right)^2 \tag{4.9}$$

$$\simeq -3.8 \times 10^7 (\frac{B}{10^{-9} G.})^2 (\frac{E}{10^{20}})^2 eV s^{-1} \tag{4.10}$$

where B = $|B_{EGMF}|$, $r_o$ = the classical electron radius, and $m_e$ = the mass of the electron.

Kronberg has recently revised this previous idea by adding that there could exist randomly-placed filaments of higher magnetic field. The magnitude of this field is less than $10^{-6}$ G. Therefore, we have two outside estimates for the magnitude of the EGMF: $10^{-12}$ G $\leq B_{EGMF} \leq 1$ $\mu$G.

In order to check if this primordial field will noticeably effect the observed trajectories of the UHECR in which we are interested, I set the magnetic field outside the immediate galactic neighborhood to be equal to either of these two extreme values. I then traced the trajectories of anti-protons through said constant fields, and out to 50 Mpc (the furthest distance from which the primaries could be coming, due to GZK constraints). I computed the power spectra for these results, as well as looked at the angular distribution on the sky that would be characteristic to each of these EGMF models. I compared these results to the same calculations

made if I simply extended the calculation of the GMF out to 50 Mpc. I found all of the results to be so similar, that I was sure that I could discount the bending done to the particles outside the galaxy as negligible when compared to the bending of the trajectories done by the GMF.

In order to ascertain that the simulation was working correctly, I then checked the values of the magnitude of B at 50 Mpc, given only the GMF calculation. I found them to be on the order of 1 $\mu$G - 1 nG.

## 4.4 GMF vs. EGMF

We can *estimate* the magnitude of the bending of a charged particle trajectory by first considering a simple case with a constant magnetic field. As shown below in Fig.4.3, take a source located a distance $L$ from the observer on earth emitting protons. A constant magnetic field $B$ is oriented into the plane of the page.

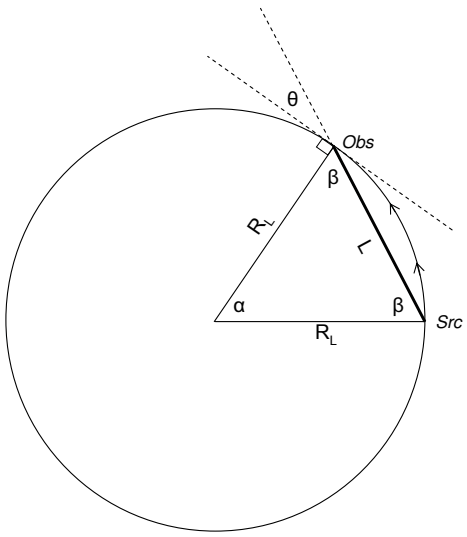


Figure 4.3: Circular trajectory of a charged particle in a magnetic field

Charged particles travel along a circular path with radius of curvature $R_L$, the Larmor radius. The angle $\alpha$ is the deflection angle of the particle trajectory with

respect to its initial trajectory. But note that the angle $\theta$ is the *observed deviation* of the arrival direction of the proton with respect to the line-of-sight direction to the source. The angle $\theta$ is what concerns us. It is simply related to $\alpha$: inspecting Fig.4.3, $\theta + \beta = 90^\circ$ and $\alpha + 2\beta = 180^\circ$, so $\alpha = 2\theta$.

The Larmor radius $R_L$ is easily obtained by inspecting the central-force which causes a circular path:

$$F = qvB = \frac{mv^2}{R_L}$$

$$R_L = \frac{mv}{qB} = \frac{p}{qB}$$

where $p$ is the proton momentum. Our concern is with extremely relativistic protons, so

$$R_L \approx \frac{E/c}{qB}$$

with $E$ the proton energy and $c$ the speed of light. To obtain this expression in a more convenient form, explicitly calculate $R_L$ for $E = 10^{19}\mathrm{e}$ and a magnetic field strength typical of the Galaxy, $B = 1\mu\mathrm{G}$ :

$$R_L \approx \frac{(10^{19}\mathrm{e})(1.6\times10^{-19}\mathrm{J/e})/(3\times10^{8}\mathrm{m/s})}{(1.6\times10^{-19}\mathrm{C})(1\mu\mathrm{G})(10^{-10}\mathrm{T}/\mu\mathrm{G})} = 3.33\times10^{20}\mathrm{m}\times\frac{1\mathrm{pc}}{3.085\times10^{16}\mathrm{m}} = 10.8\ \mathrm{kpc},$$

giving a simple formula for $R_L$:

$$R_L = 10.8\ \mathrm{kpc}\frac{E_{19}}{ZB_{\mu\mathrm{G}}} \tag{4.11}$$

where $E_{19}$ is the energy in units of $10^{19}\mathrm{e}$, $B_{\mu\mathrm{G}}$ is the magnetic field strength in $\mu\mathrm{G}$, and $Z$ is the charge of the particle in units of $e$ (for protons, $Z = 1$). An alternative form for much smaller fields follows trivially:

$$R_L = 10.8\ \mathrm{Mpc}\frac{E_{19}}{ZB_{\mathrm{nG}}} \tag{4.12}$$

with $B_{\mathrm{nG}}$ the field in nanogauss.

The observed angular deviation $\theta$ can be computed by inspecting Fig.4.3:

$$R_L \sin(\alpha/2) = L/2$$

or using the relation $\alpha = 2\theta$,

$$2R_L \sin\theta = L.$$

Then

$$\sin\theta = \frac{1}{2}\frac{L}{R_L} = \left(\frac{L}{21.6\mathrm{kpc}}\right)\frac{B_{\mu\mathrm{G}}}{E_{19}} = 0.046\frac{L_{\mathrm{kpc}}B_{\mu\mathrm{G}}}{E_{19}} \tag{4.13}$$

using Eq.4.11, with $L_{\mathrm{kpc}}$ the straight-line distance to the source in kpc. If the deviation is small,

$$\sin\theta \approx \theta = 2.7^\circ\ \frac{L_{\mathrm{kpc}}B_{\mu\mathrm{G}}}{E_{19}} = 2.7^\circ\ \frac{L_{\mathrm{Mpc}}B_{\mathrm{nG}}}{E_{19}} \tag{4.14}$$

showing the deviation when using either $(\mathrm{kpc}-\mu\mathrm{G})$ or $(\mathrm{Mpc}-\mathrm{nG})$ units. We now can compare the deviations expected due to Galactic and extra-Galactic fields. Suppose a $10^{19}\mathrm{e}$ proton travels from an extra-Galactic source at 50 Mpc through a presumably typical field strength of $10^{-3}\mathrm{nG}$ . Eq. 4.14 gives an observed deflection $\theta = 0.14^\circ$ [5]. But when it enters our Galaxy, it will traverse a typical distance of perhaps 5 kpc (an effective "source" distance of $L_{\mathrm{kpc}} = 5$) through a typical field strength of $2\mu\mathrm{G}$. The angular deviations from the Galaxy is then $\theta = 28^\circ$. Clearly the Galactic bending dominates the two effects.

The ratio of the extra-Galactic and Galactic deflections, $\theta_{EG}/\theta_G$, is

$$\frac{\theta_{EG}}{\theta_G} = \frac{L_{\mathrm{Mpc}}B_{\mathrm{nG}}}{L_{\mathrm{kpc}}B_{\mu\mathrm{G}}} = 0.005$$

using the field strengths and distances assumed above. Since it is very unlikely to observe any particles from distances greater than 50 Mpc due to the GZK effect, the dominant factor in the ratio is the relative strengths of the magnetic fields. The

strength of the Galactic field is reasonably well known, but the extra-Galactic field is understood much less well. If it were significantly stronger than $10^{-12}$G (i.e., $B_{\rm nG} \gg .001$), then the ratio of the two deflections may become comparable. The actual deviations are the subject of this thesis, and we'll simulate them in great detail. The previous discussion used an order of magnitude estimate to justify why we neglected the extra-Galactic field. It is a fair question to ask if that estimate is not good for the extra-Galactic case, since that field is likely not a constant over such vast distances.

Suppose we assume that the large-scale field is arranged into "cells". Inside of each cell the field is assumed to be constant, each cell's field has the same magnitude, but the orientation of the fields in the cells are all completely independent of each other. We assume that characteristic size of such cells are given by a "coherence length" parameter $\ell$. It is reasonable to take $\ell = 1{\rm Mpc}$.

Since the deflection in a very weak field is quite small over 1 Mpc (see Eq. 4.14 ), we can treat this as a series of independent small-angle scatterings as the particle traverses the arc length drawn in Fig. 4.3. In each cell, we can use the constant-field approximation that we just developed, but each cell's field is oriented differently. In such a random-walk, after $N$ steps or cell-traversals the average angular displacement will be $\sqrt{N}$ times the deviation in each individual step. This will actually give *less* net deviation at the end than if all the cells' fields were oriented the same, in which case the final deviation would be $N$ times the deviation of one cell.[1]

[1]This is similar to the well-known case of multiple scattering of charged particles, where the r.m.s. deflection is proportional to $\sqrt{x/X_\circ}$, with $x$ the thickness of material and $X_\circ$ the radiation length in that material; in other words the square root of the number of "steps" in units of radiation lengths [34]. Explicitly, the number of steps is approximately

$$N = \frac{s}{\ell}$$

where $s$ is the total length of path traveled from the source to the observer. If we assume as before that the net deflection is so small that the chord-length $L$ in Fig. 4.3 is approximately the same as the actual arc-length path, then the angular deviation in Eq. 4.14 should be modified to be $\sqrt{N}$

## 4.5 Origin of the Random Walk

Consider a two-dimensional random-walk. This is a series of steps, each of the same distance, but each one is randomly oriented with respect to the previous step. Do it as a sum of unit vectors (i.e., step size 1.0). A unit vector in the $xy$ plane has this form: $\hat{n} = (x, y) = (\cos\theta, \sin\theta)$ where $\theta$ is the angle of $\hat{n}$ from the $x$-axis. If these are randomly oriented, that is the same as saying that $\theta$ is a random number between zero and $2\pi$.

The magnitude of the vector is the square root of $|\hat{n}|^2 = \hat{n} \cdot \hat{n} = x^2 + y^2 = \cos^2\theta + \sin^2\theta = 1.0$. An equivalent representation of this vector can be as a complex number:

$$z = x + iy = \cos\theta + i\sin\theta = e^{i\theta}$$

then the square of the vector magnitude is simply

$$zz^* = e^{i\theta}\ e^{-i\theta} = 1.0$$

Suppose I add $N$ of these vectors together, the resultant is

$$Z = \sum_{j=1}^{N} e^{i\theta_j}$$

with squared magnitude

$$ZZ^* = \sum_{j=1}^{N} e^{i(\theta_j - \theta_j)} \quad + \sum_{j,k=1(j\neq k)}^{N} e^{i(\theta_j - \theta_k)} = \quad N \quad + \sum_{j,k=1(j\neq k)}^{N} e^{i(\theta_j - \theta_k)}$$

The second term has $(\theta_j - \theta_k)$, each angle of which is random. The difference

---

times the deviation over small cell (of size $\ell$) giving

$$\sin\theta \approx \theta = 2.7^\circ \left[\frac{L_{\rm Mpc}}{\ell_{\rm Mpc}}\right]^{1/2} \frac{\ell_{\rm Mpc} B_{\rm nG}}{E_{19}} = 2.7^\circ \frac{(\ell_{\rm Mpc} L_{\rm Mpc})^{1/2} B_{\rm nG}}{E_{19}}$$

So our previous discussion using constant extra-Galactic fields is still giving a fair order-of-magnitude estimate of the effects.

between two random numbers is also a random number, so call it $\phi$ and it is distributed just like $\theta$, over zero to $2\pi$. That sum is then just like taking averages of the components:

$$\sum e^{i\phi} \propto \langle \cos\phi \rangle + i \, \langle \sin\phi \rangle = 0 + i \, 0 = 0.$$

So that second term vanishes. Hence the resultant vector $Z$ has magnitude $\sqrt{ZZ^*} = \sqrt{N}$. This 2-d random walk on a plane applies to our problem with deflection angles too. Since the scattering angles are small, the deviations of one trajectory vector to the next on the surface of a sphere is like a little vector on a plane surface, just like above. The total deviation is then $\sqrt{N}$ times the magnitude of an individual scatter.

## 4.6 Active Galactic Nuclei

The leading candidates for the source of UHECR are large, energetic structures where strong shocks are expected to be found. The most well known of these are supernova remnants, which have long been suspected to generate cosmic rays. In 1995, Japan's ASCA X-ray Satellite reported positive observations of non-thermal X-ray emissions from the Supernova Remnant SN1006. The observed emission spectrum is consistent with synchrotron emission by accelerated charged particles. This report is widely seen as confirmation of supernova remnants as a known source of cosmic rays. The observed emission from SN1006, with some fine tuning of the emission models, can explain the existence of cosmic rays up to $\simeq 10^{15}$ eV. However, it is difficult to explain the existence of cosmic rays above $10^{18}$ eV, because supernovae are simply not large enough to maintain acceleration to the UHE regime. Furthermore, no positive correlation has been observed between the arrival directions of UHE cosmic rays and supernova remnants.

There are many larger objects in the sky where strong shocks are expected. For example, strong shocks are possible around colliding galaxies such as NGC

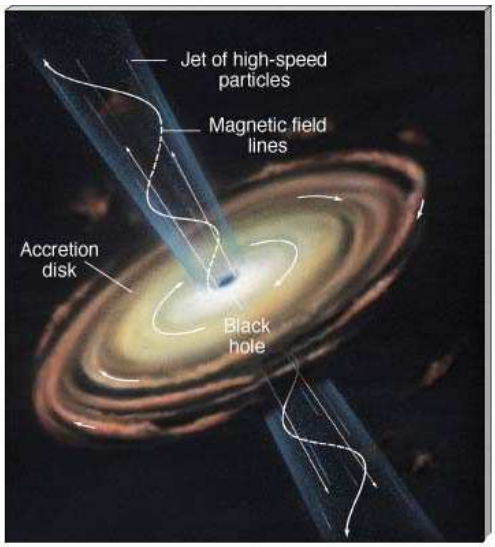


Figure 4.4: Active Galactic Nucleus

4038/9. However, there is no evidence to indicate these objects are sources of UHE cosmic rays. Another class of objects which are candidate sources of UHE cosmic rays are active galactic nuclei (AGN), which is represented by Figure 4.4. AGN is the generic name given to a class of galaxies which are suspected to have at their center a supermassive black hole. AGNs are typically accompanied by jets which can extend 15-30 kpc. Roughly one of every ten known galaxy has an AGN. It is therefore always possible to find an AGN within error of the arrival direction of most UHECR.

To accelerate a charged proton to $E = 10^{19}$eV one needs an electric potential difference of $10^{19}$eV over some spatial distance. If the distance is small, it is relatively easy to set up an electric field (i.e., the voltage divided by that distance) with such high intensity. Hillas [35] gave a useful way to get an order of magnitude estimate of the situation.

On the left side of Fig. 4.5 is a classic freshman-physics problem. A loop of wire is being pulled into a region where there is a constant magnetic field. The magnetic flux through the loop is increasing, causing an electric field to be induced

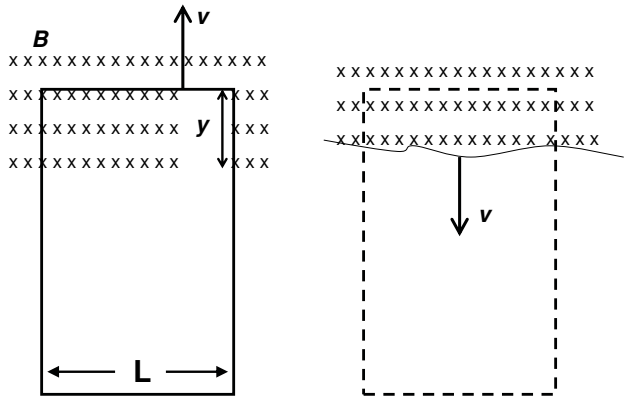


Figure 4.5: Left: a loop of wire being pulled into a region with a uniform magnetic field B into the page. Right: A shock wave with an embedded magnetic field moving into a region indicated by the (imaginary) lines.

around the loop, by Faraday's law. Notice the similarity with the situation on the right side of the figure: a plasma shock wave with an embedded magnetic field is entering a region of space indicated with the dotted lines. The geometry is the same, so Faraday's Law applies here too, and we will see an induced electromotive force as well.

The loop has a width $L$ and is being pulled in the $y$-direction at speed $v$. The magnetic flux through the loop $\Phi_B = B(Ly)$ is increasing as the overlap region $y$ increases. There is an induced voltage $\Delta V$ around one traversal of the loop according to Faraday's Law

$$\Delta V = \frac{d\Phi_B}{dt} = BL\frac{dy}{dt} = BLv$$

The energy of a particle with charge $q$ in the wire after it accelerates through one revolution is $q\Delta V = qBLv$. Comparing to the shock-wave situation on the right side of the Figure, Hillas gives his estimate for the maximum energy that can be

obtained when a particle of charge $Ze$ is accelerated by shock-waves:

$$E_{max} = Ze(\beta c)BL$$

where $B$,$L$,$\beta$ are characteristic values for the field strength, size, and speed ($v = \beta c$) of the accelerating engine. Figure 4.6 plots the characteristic sizes ($L$) and field strengths ($B$) of a number of astrophysical objects.

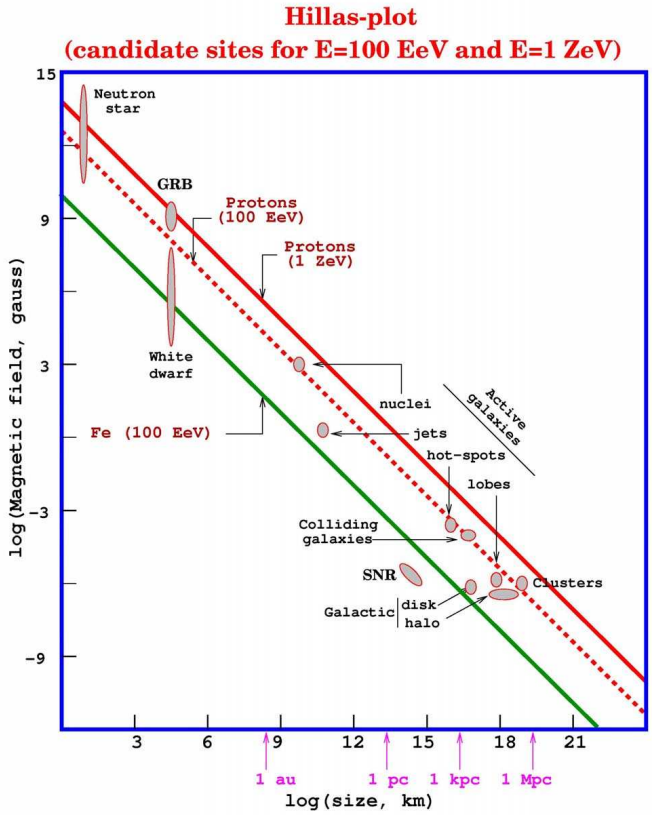


Figure 4.6: Size and magnetic field strength of possible sites of particle acceleration. Objects below the diagonal lines cannot accelerate particles beyond $10^{20}$ eV by shock acceleration. Dashed line is for protons (Z=1) and the lower solid line is for iron nuclei (Z=26), each for shock speed $\beta = 1$. Also shown (upper solid line) is the case for $10^{21}$eV (1 ZeV) protons.

It is clear that it is difficult to find objects capable of getting particles to $10^{20}$ eV. Active Galactic Nuclei and the jets sometimes found with them have the requisite size and field strength. Neutron stars have very strong fields and so also look

like they could do the job. But this argument has not taken into account the environments of the accelerator. The intense radiation in the neighborhood of a neutron star would likely prevent the escape of an accelerated proton - it tends to collide with the photons in the field and lose energy. The lobes at the tips of the jets from AGN seem like a better choice, as they are well away from the central engine and its own intense radiation fields. That's why AGNs - especially those with long radio jets with intense lobes - are favored sites for acceleration to 100 EeV and beyond.

## 4.7 Calculation of the Power Spectrum

Any collection of points on a sphere can be represented by a sum of spherical harmonics (assuming the whole sphere to be populated). The method of using power-spectra coefficients is an attempt to provide a common language for model builders and experimentalists. If cosmic ray sources are not bright point-sources, then this method gives a well-defined way for various models to be tested against data. Therefore, by analyzing these spherical harmonics, and their coefficients, we can draw conclusions about the anisotropy patterns of the distribution of $(\theta, \phi)$ we see. In general, the intensity function over the sphere is defined to be:

$$I(\theta, \phi) = \sum_{l=1}^{\infty} \sum_{m=-l}^{l} a_{lm} Y_{lm}(\theta, \phi) \tag{4.15}$$

where the coefficients $a_{lm}$ are then

$$a_{lm} = \int I(\theta, \phi) Y_{lm}(\theta, \phi) d\Omega \tag{4.16}$$

There are intrinsically imaginary parts to $Y_{lm}$, but these can be replaced by following [6]:

$$e^{im\phi} \rightarrow \begin{cases} \sqrt{2}sin(m\phi) & (m < 0) \\ 1 & (m = 0) \\ \sqrt{2}cos(m\phi) & (m > 0) \end{cases}$$

For the purposes of simulating real data, we'll assume a non-uniform exposure, $\omega_i$. We'll then be able to characterize the $a_{lm}$ values for a discrete set of N events as:

$$a_{lm} = \frac{1}{N}\sum_{i=1}^{N} \frac{1}{\omega_i} Y_{lm}(\vec{u}^i) \tag{4.17}$$

where $\omega_i$ is the relative exposure at arrival direction $\vec{u}^i$, and $N$ is the sum of the weights $\frac{1}{\omega_i}$.

The calculation of this exposure will be discussed later.

The intensity function can then be characterized for a discrete distribution of points as:

$$I(\theta, \phi) = \sum_{l=1}^{20} \sum_{m=-l}^{+l} a_{lm} Y_{lm} \tag{4.18}$$

The angular power spectrum, or $C_l$ values, is represented by taking the average of the spherical harmonics' coeffecients mentioned above.

$$C(l) = \frac{1}{2l+1} \sum_{m=-l}^{l} a_{lm}^2 \tag{4.19}$$

We can use the values of $C_l$ to determine not only whether or not anisotropy exists in any given collection of points, but also the scale of it. The values of $C_l$ are sensitive to variations over angular scales of about $1/l$ radians. Therefore, by studying which $C_l$ values are heightened or suppressed in a given distribution, we can determine what kind of anisotropy we're looking at, whether it be a large-scale

dipole or small-scale clustering. As such, this is a very powerful analysis tool for large-scale searches for anisotropy.

In the analysis in question, I have first tested this method of quantifying anisotropies by generating simple distributions of particles and looking at the $C_l$ values yielded. I used the random number generator included in the C++ standard library to generate random values for $cos(\theta)$ and $\phi$. The random number generator, rand(), produces a random number between 0 and a maximum constant defined by the implementation. In my package, the maximum value is 2147483647. I seed the random number generator with the system time, in order to ensure that each set of random numbers is different.

First, I generated a homogeneous distribution over the entire sky by using the random number generator in C++. I generated 1000 random values between 0 and 1 to represent the values of the cosine of the zenith angle, $\theta$ and between 0 and $2\pi$ to represent the values of the azimuthal angle, $\phi$. I then randomly selected half of the points and forced their $\cos(\theta) = -\cos(\theta)$. This yielded an even distribution of random points between $-1 \leq \cos(\theta) \leq 1$ and $0 \leq \phi \leq 2\pi$. By distributing the particles evenly throughout any given solid angle $(\cos\theta, phi)$, I could ensure that the entire celestial globe was covered evenly.

After generating this distribution, I took each particle and recorded its $(\cos\theta, phi)$ value and computed its $Y_{lm}$ for $0 \leq l \leq 20$ and $-l \leq m \leq +l$. The l values correspond to angular resolution on the sky as $l \simeq 1/\theta$ (in radians). Therefore, by setting the upper limit of l to be 20, I could be sure that I was only looking at the upper limit of angular resolution of the Pierre Auger Observatory, which is taken to be $\simeq 1\,\mathrm{deg}$. From these values of $Y_{lm}$, I used the above-mentioned formulae for a discrete distribution of points to compute the $a_{lm}$ and $C_l$ values. For the homogeneous distribution, I obtained the distributions of values seen in Figure 4.7.

There is obviously no signature of the $C_l$ values, which is what we expected, as per Figure 4.7. Now that it appears evident that this simple simulation is working

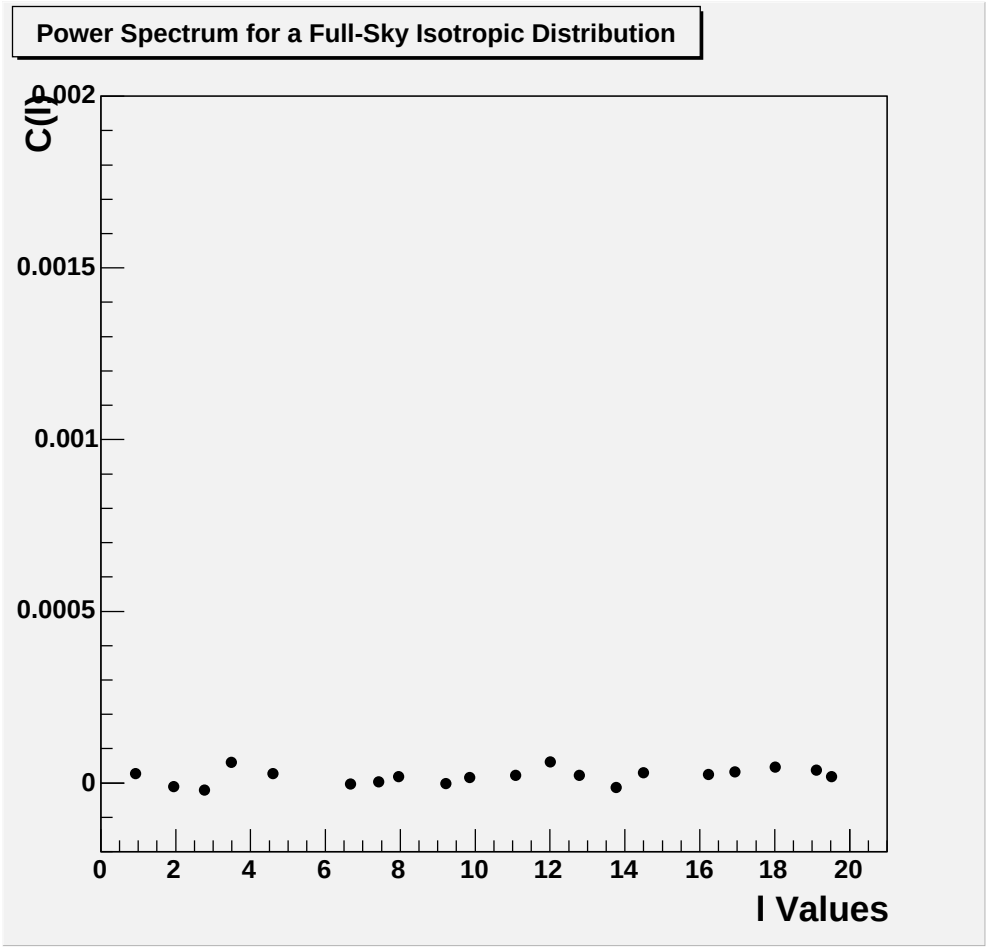


Figure 4.7: $C_l$ Values For a Homogeneous Full-Sky Distribution of Events

on a full-sky distribution, we have to make sure that the same analysis will yield the same results for a half-sky distribution. Since the detector currently under construction is only in the southern hemisphere, we can only see half the sky. Therefore, we need to know how this will affect the power spectra computed from the distribution of observed events.

Obviously, even a completely homogeneous distribution of points visible on only half the sky will appear anisotropic, and, more specifically, dipolar in nature. The distribution is simulated by using a simple procedure, in which I took the original homogeneous distribution that I generated and read in only points where $cos(\theta) \geq 0$. I then computed the $C_l$ values as usual and obtained Figure 4.8.

It is immediately obvious that this cut has made the sky look like a dipole, and

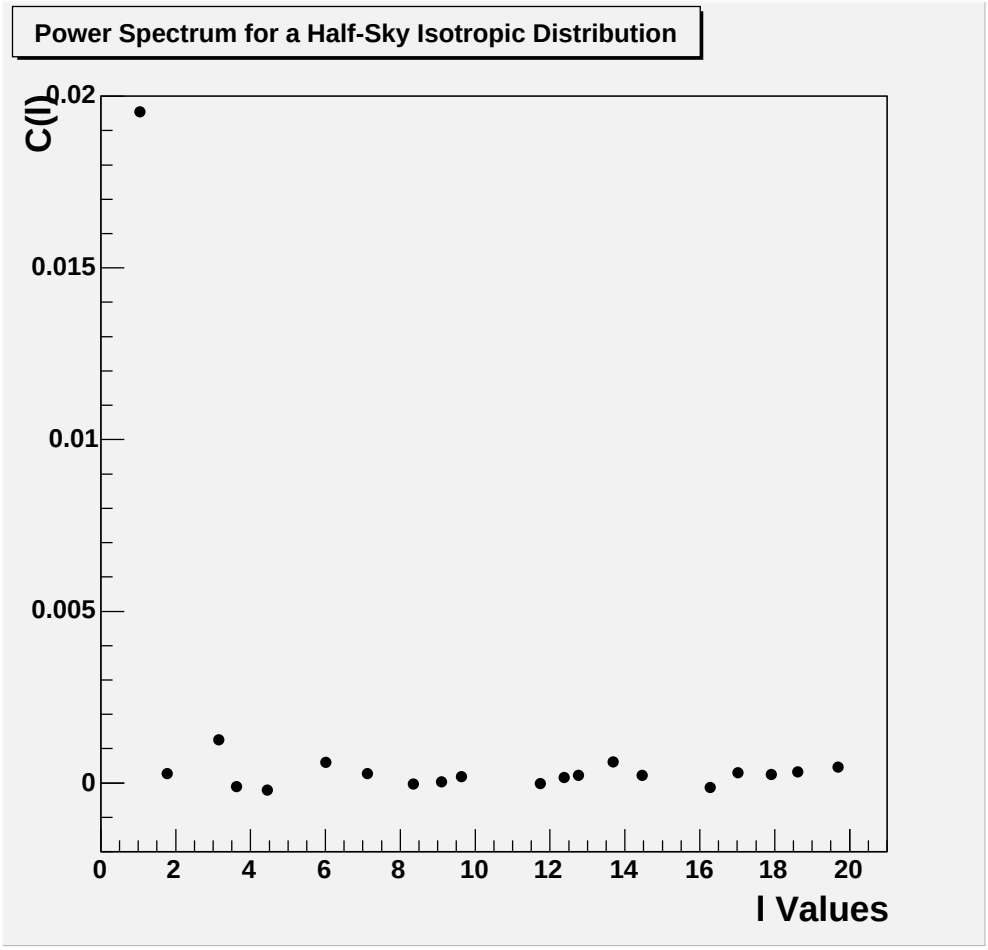


Figure 4.8: $C_l$ Values For a Homogeneous Half-Sky Distribution of Events

this is supported by the $C_l$ values, where the $l = 1$ value has greatly increased in comparison to the rest of the values.

The next logical step is to test an actual dipole distribution, which is simple to generate. For this, I simply re-generated the 1000 random points between $0 \leq \phi \leq 2\pi$ for the azimuthal angle and betweeen $0 \leq \cos(\theta) \leq 1$ for the zenith angle. This time, I took $\sqrt{\cos(\theta)}$ to be the zenith angle, in order to force a dipole-like distribution. To cover the entire sky, I assigned $\cos(\theta) = 2.\cos(\theta) - 1$. This kept the dipole distribution, but forced it to go from $-1 \leq \cos(\theta) \leq 1$. I then computed the $Y_{lm}$ values again, and from them computed the $a_{lm}$ and $C_l$ values again. The $C_l$ distribution became that seen in Figure 4.9.

After testing these two distributions, I generated a quadropole. This distribu-

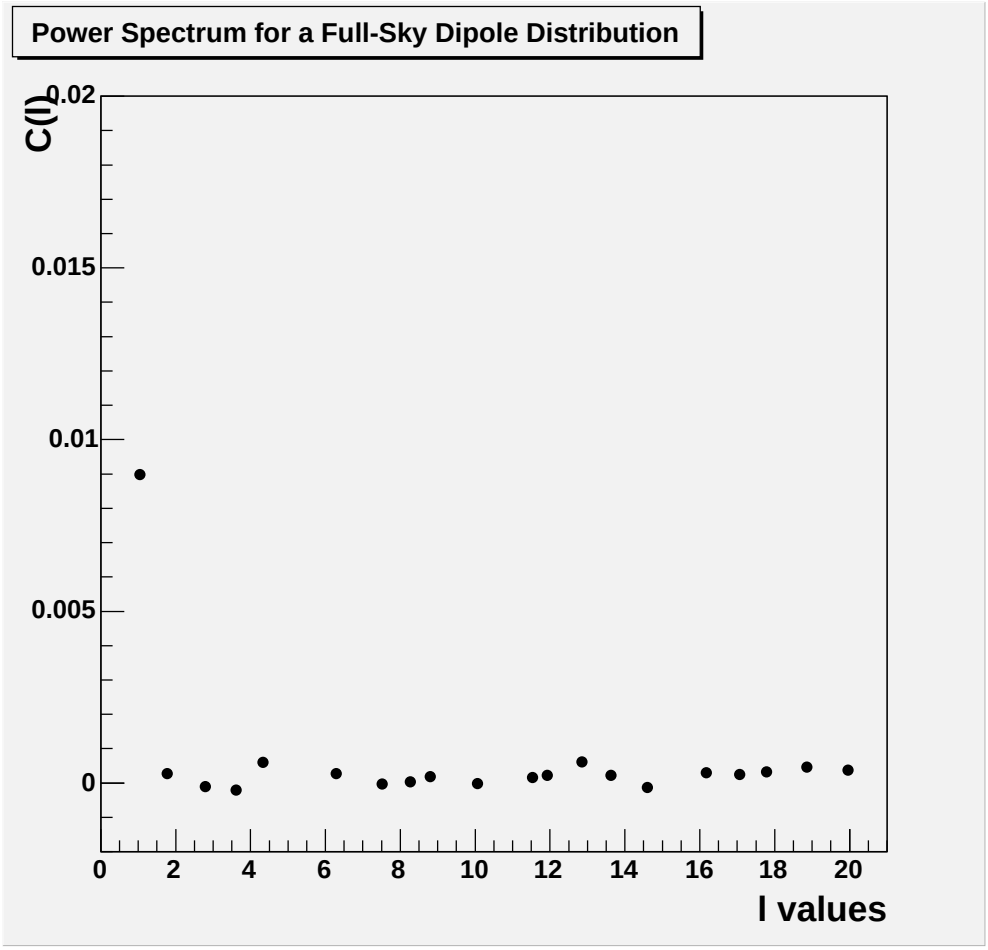


Figure 4.9: $C_l$ Values For a Full-Sky Dipole Distribution of Events

tion can be easily approximated by taking the cube root of the random values for $cos\theta$. Again, I forced the distribution into a full-sky set of points by randomly generating a number between 0 and 1, then comparing it to the points. If the value of $cos(\theta)$ was lower than the random number, I made it negative. This forces around half of the particles to have their initial solid angle value switched from $cos\theta$ to $-cos\theta$. I obtained the following results. For the values of $C_l$, I obtained Figure 4.10.

For the $a_{lm}$ values, I obtained the values in Figure 4.11.

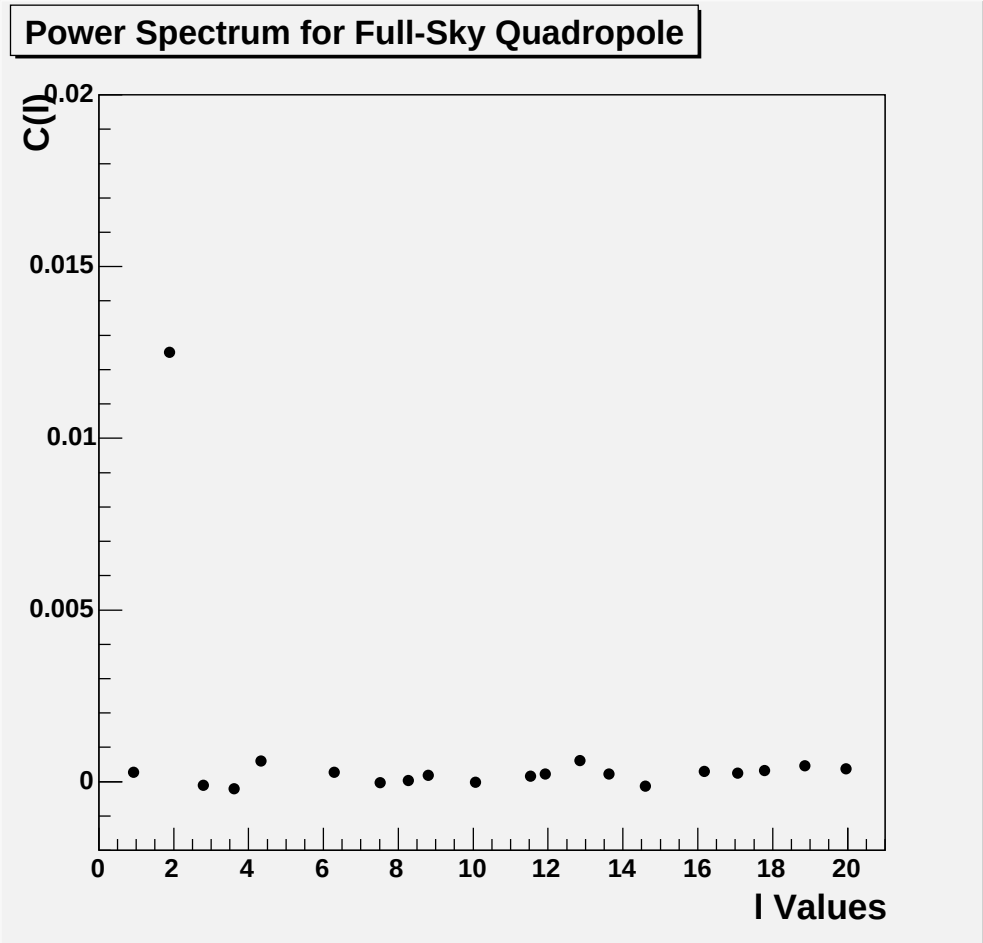


Figure 4.10: $C_l$ Values For a Full-Sky Quadrupole Distribution of Events

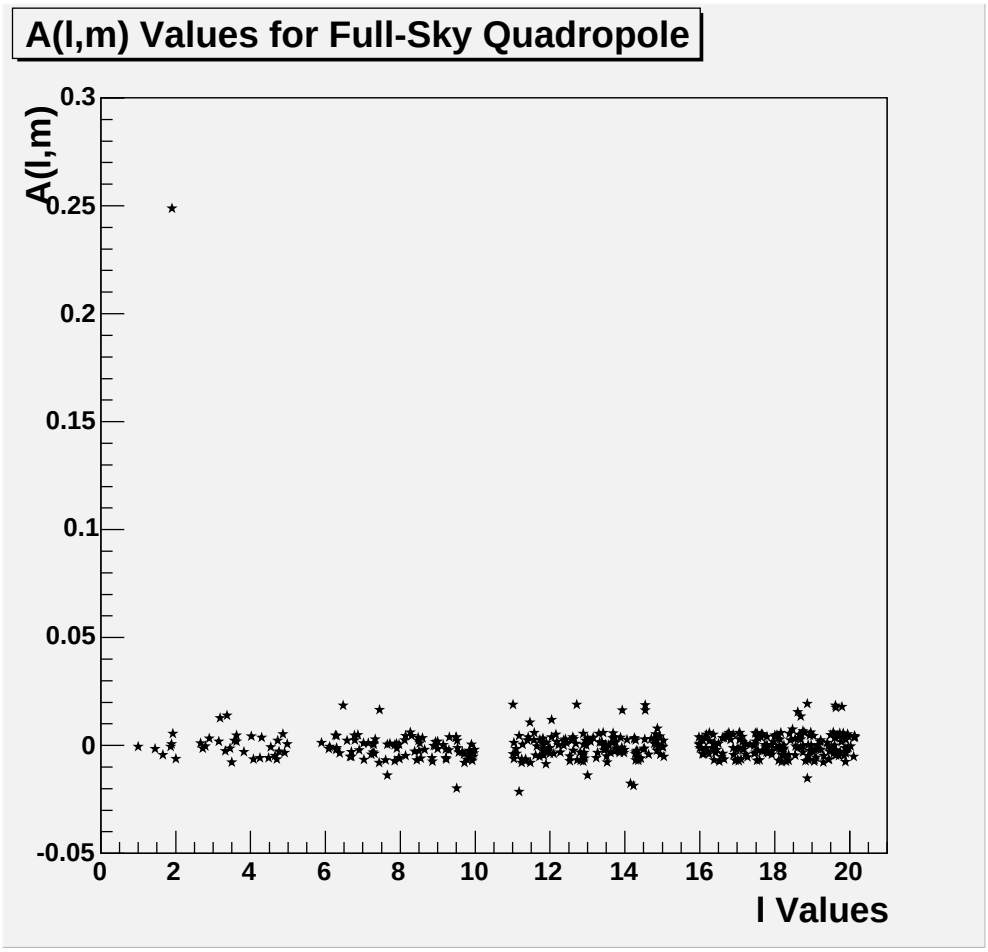


Figure 4.11: $a_{lm}$ Values For a Full-Sky Quadrupole Distribution of Events

# Chapter 5: Propagation

## 5.1 The Simulation

In order to trace the trajectories of particles through the universe, we have employed the standard practice of tracing the reverse trajectories of antiprotons [36, 37]. In the method, we generate a random, flat distribution of negatively-charged protons at the earth's surface (9.202 kpc removed from the galactic center, taken for these purposes to be along the y axis). We then assign them random initial orientations before injecting them into the galaxy. An Aitoff projection of the initial positions of the particles is shown in Figure 5.1.

Simply using the Lorentz force equation,$F = q(v \times B)$ we can find the force exerted by the assigned magnetic field which is felt by the particles as they travel.

It is then a simple matter to integrate the equations of motion for charged particles, in order to trace their trajectories, and obtain:

$$\frac{\Delta\vec{p}}{\Delta t} = \frac{qc^2}{E}(\vec{p} \times \vec{B}) \approx \frac{qc}{|\vec{p}|}(\vec{p} \times \vec{B}) \tag{5.1}$$

$$\frac{\Delta\vec{x}}{\Delta t} = \frac{c^2\vec{p}}{E} \approx \frac{c\vec{p}}{|\vec{p}|} \tag{5.2}$$

as long as $\Delta x$ is not too large [38], and in the ultra-relativistic limit. By adding this small increment to the previous value of x (or by adding $\Delta p_x$ to $p_x$), we find the next position or momentum, respectively.

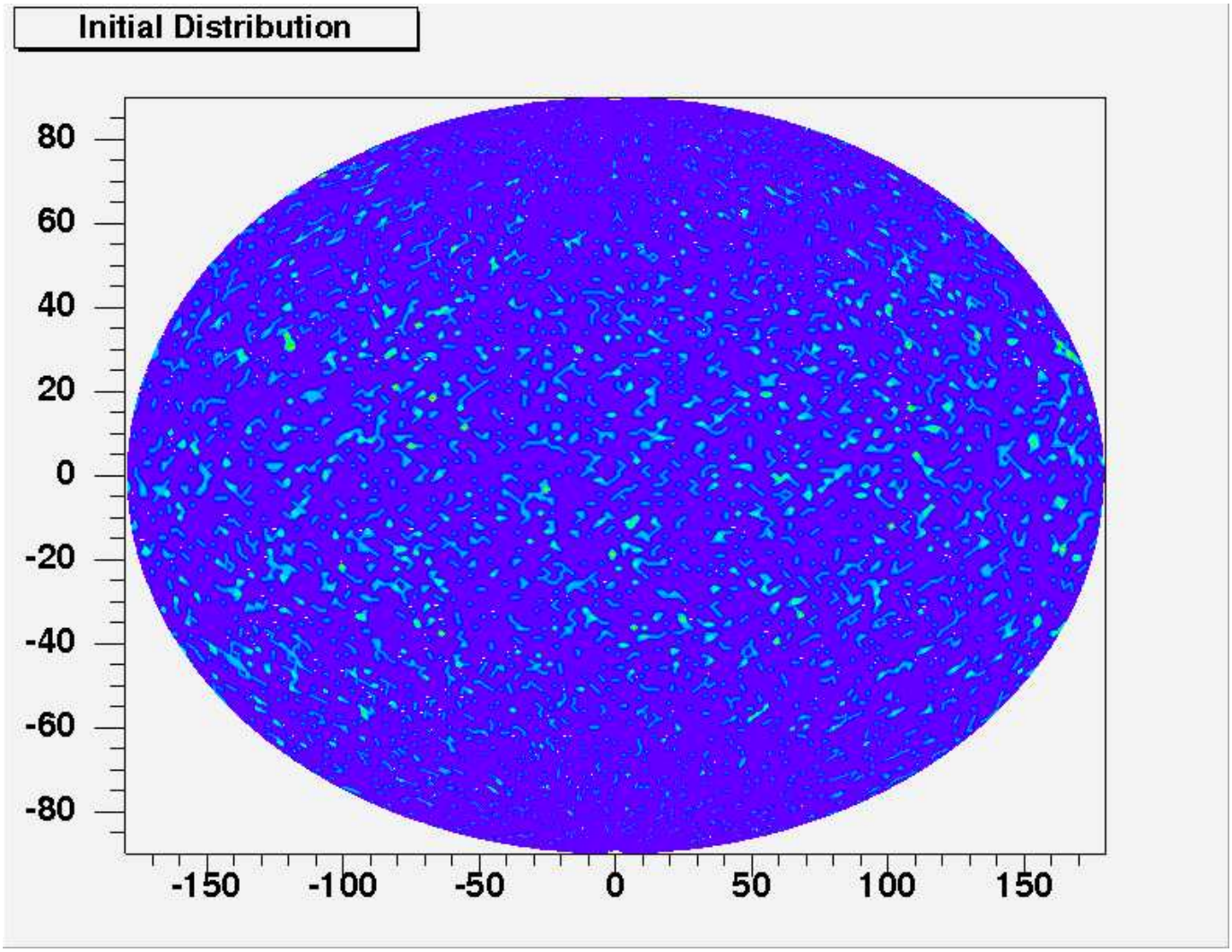


Figure 5.1: Initial Positions of Particles – Aitoff Projection

Since $F = m\ddot{x}$, it can be approximated to be equal to the change in the particle's momentum or velocity over a very small period of time. In other words, one can approximate the change in momentum of the particle over a small distance to be:

$$\vec{p}_{new} - \vec{p}_{old} = \left(\frac{c^2 \times \Delta t}{E}\right)(\vec{p} \times \vec{B}) \tag{5.3}$$

The calculation of $\Delta$t is straightforward. I simply calculate the magnitude of the magnetic field at any given point. The radius of curvature for any particle feeling only that constant magnetic field would be:

$$r_{curve} = \frac{1}{q}\frac{p_{mag}}{B_{mag}} \tag{5.4}$$

I define then a small ratio. When multiplying this ratio by $r_{curve}$, we can then define the size of the "step" taken by the particle. Simply, then, $\Delta t = \Delta s/c$. After many trials to see how small the ratio needed to be in order to be both accurate and efficient, I settled on $10^{-2}$.

Once the new momentum is found by the above method, it is a simple matter to compute the new position of the particle, using

$$\Delta x = \Delta t \times \left(\frac{c \times p_x}{p_{tot}}\right) \tag{5.5}$$

$$\Delta y = \Delta t \times \left(\frac{c \times p_y}{p_{tot}}\right) \tag{5.6}$$

$$\Delta z = \Delta t \times \left(\frac{c \times p_z}{p_{tot}}\right) \tag{5.7}$$

I then compute magnitude of the position of the particle, since $r = \sqrt{x^2 + y^2 + z^2}$. I defined the final value of r to be various distances, from as close as 25 kpc to as far as 50 Mpc. Taking the particles out to a distance of 100 kpc, we obtain the full-sky distribution of particles visible in Figure 5.2.

## 5.2 Exposure of the Detector

In general, for a cosmic ray observatory, exposure is a function of declination on the celestial sphere. The measurement of the exposure (in $km^2/yr.$) gives the time-integrated effective collecting area for a given flux from a given sky position. For the purpose of this dissertation, I will concern myself with what's known as the relative exposure. The relative exposure is a dimensionless function on the sphere with a maximum value of 1. It is, therefore, equivalent to computing the exposure at the point in question, then dividing that exposure by the maximum exposure on

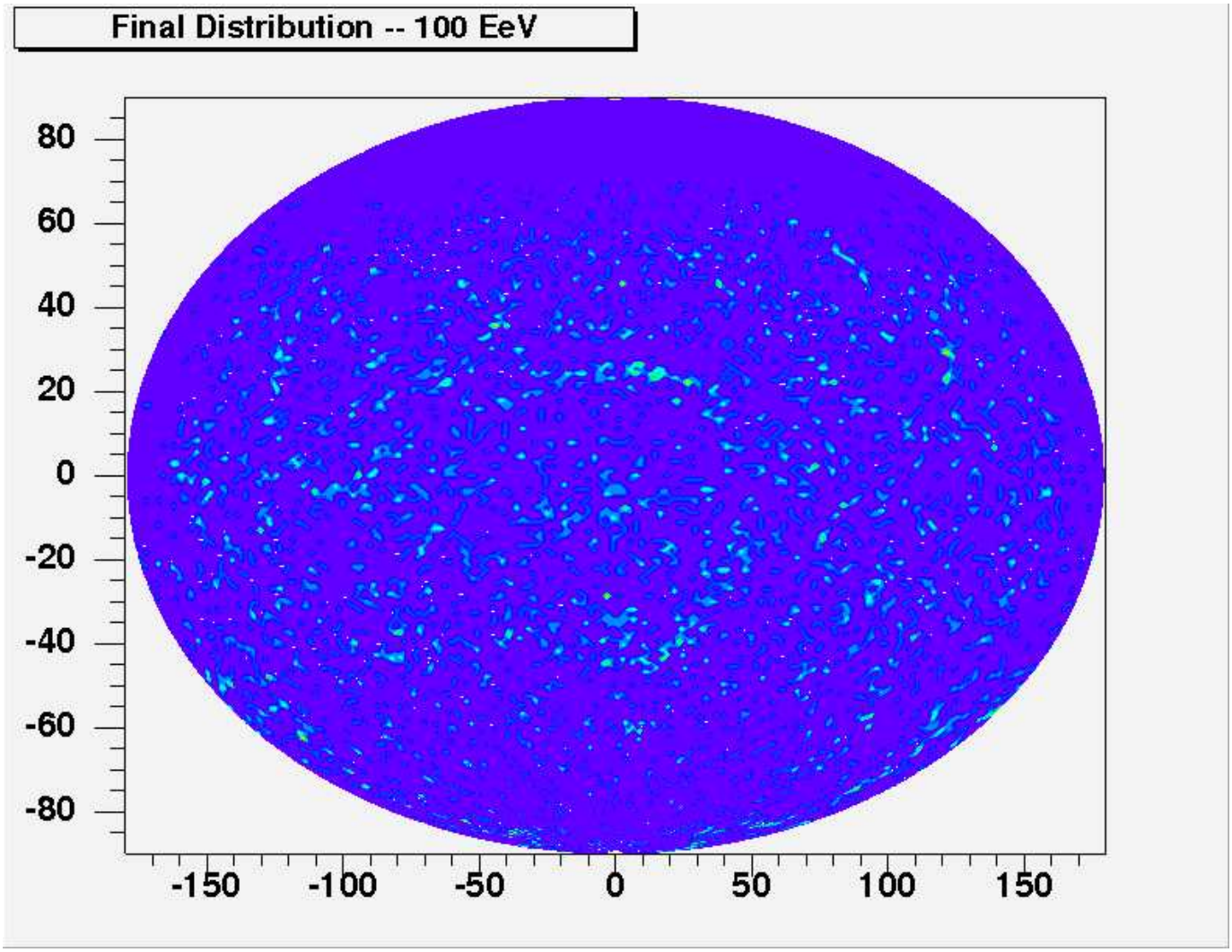


Figure 5.2: Final Positions of Particle – Aitoff Projection

the sky. In other words, if we are to calculate the relative exposure at any point on the sky, the value will be between 0 and 1. In the more general sense, "exposure" refers to the total exposure integrated over the celestial sphere, and is in units of $km^2 sr^{-1} yr^{-1}$. In practice, the observatory's exposure varies with energy, and should be re-evaluated for each energy bin. My concern is only in the post-GZK cutoff range, and so the exposure need only be calculated for that energy bin.

Since the energy spectrum is defined by the number of observed events divided by total exposure, one can use the measured spectrum to get the expected number of cosmic rays for any given total exposure. In the case of the Auger surface ar-

rays, the continuous acceptance is approximately $10,000 km^2 sr\ yr$, independent of energy above $10^{19}$ eV. After operating for 5 years, they will have a total exposure of $70,000 km^2 sr\ yr$. The integral cosmic ray intensity above $10^{19}$ eV is approximately 0.5 $km^2 sr\ yr$, and it falls roughly like $E^2$ (perhaps less rapidly, but the energy dependence is not well determined above $6 \times 10^{19}$ eV.) Using this simple $E^2$ dependence gives the following estimates for Auger cosmic ray counts after 5 years: 35,000 above $10^{19}$ eV, 2200 above $4 \times 10^{19}$ eV.

Cosmic ray air shower detectors steadily operational for a full year will have a uniform exposure in right ascension, $\alpha$. Such a detector, taken to be at latitude $a_0$ with full detection efficiency for $\theta \leq \theta_{max}$ will have a relative exposure dependent on declination as:

$$\omega(\delta) \propto \cos a_0 \cos\delta \sin \alpha_{max} + \alpha_{max} \sin a_0 \sin\delta \tag{5.8}$$

where $\alpha_{max}$, the local hour angle at which the zenith angle becomes equal to $\theta_{max}$, is given by:

$$\alpha_{max} = \begin{cases} 0 & (\xi > 1) \\ \pi & (\xi < -1) \\ cos^{-1}\xi & (otherwise) \end{cases}$$

with

$$\xi \equiv \cos\theta_{max} - \sin a_0 \sin\delta \cos a_0 \cos\delta \tag{5.9}$$

where, for the Southern detector of the PAO, latitude is $a_0 = -35.5^0$ and the maximum value of $\theta$ for full detector efficiency is $\theta_{max} = 60^0$.

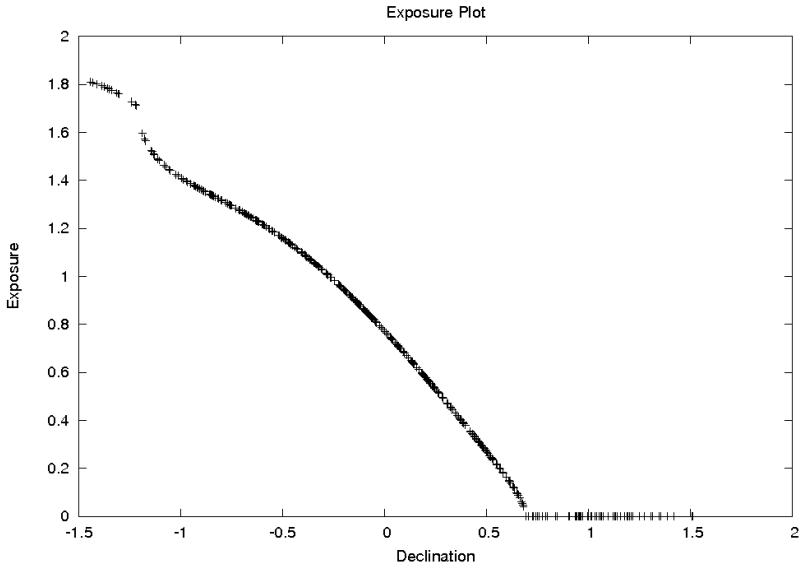


Figure 5.3: Exposure of the PAO Detector in Argentina

# Chapter 6: Results

## 6.1 Results of Simulations

The lowest energy particles tried, at E = $10^{19}$ eV, were markedly bent by the GMF. We found the distributions became both more skewed and sparse as we moved out in distance, tending to cluster on large scales.

We started out each time with a randomly generated distribution of points, as seen in Figures 6.1 and 6.2.

The trajectory of a single 10 EeV particle is shown in Figure 6.3, showing curvature which basically traces out the GMF in the plane of the disk. 5000 such particles were then released into the GMF and traced out to 100 kpc, yielding the final solid angle distribution seen in Figures 6.5 and 6.4.

The clustering level is easier to analyze for our purposes in Figure 6.4 than it is in Figure 6.5, so we will continue on using this type of plot to look at the clustering of particles at their final shells.

We can see that the particles have become clustered. At $10^{20}$ eV, of course, there is less curvature due to the magnetic field. However, there appears to be a slight suppression of particles in the direction of the GC due to the very high field there.

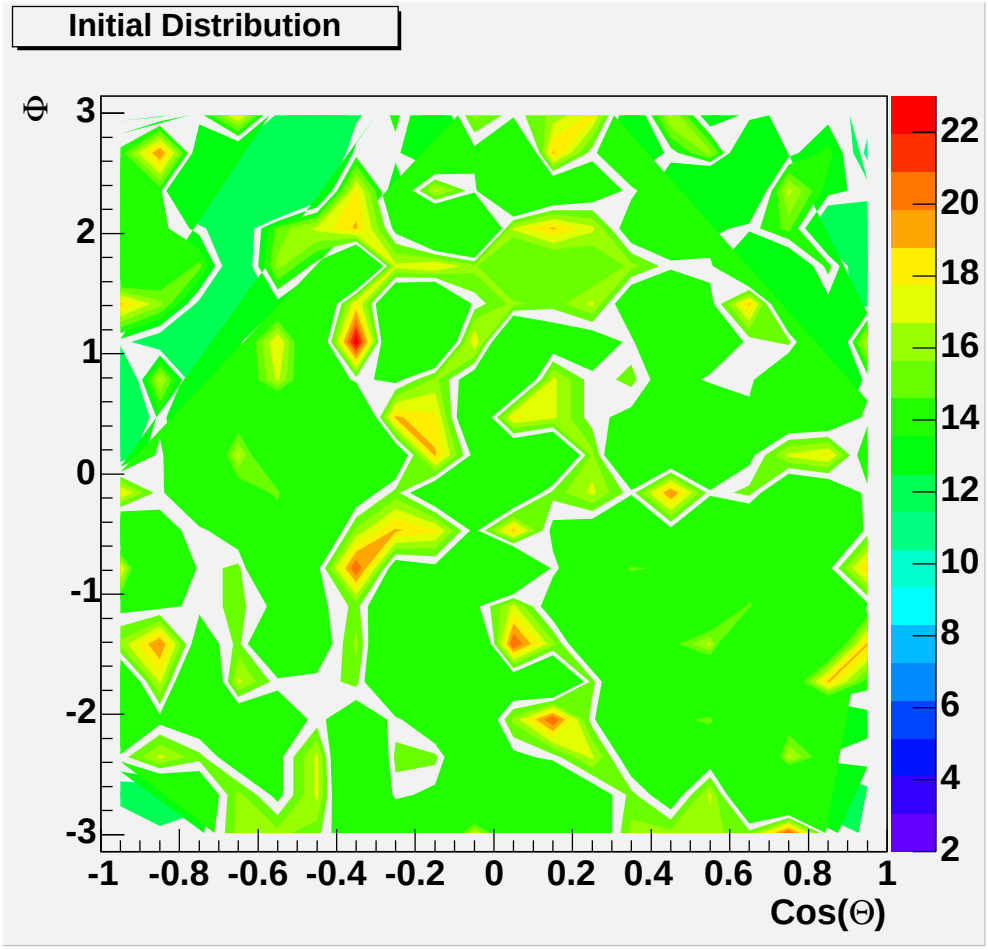


Figure 6.1: Initial Directions

## 6.2 Different Magnetic Field Models

### 6.2.1 Bisymmetric Galactic Magnetic Field Model

As previously stated, we have been using the ASS (axisymmetric) model of the galactic magnetic field. In order to make sure our results are consistent with both models, we ran some simulations using the BSS (bisymmetric) model of the field as well. We randomly generated 5000 particles of $10^{20}$ eV at the earth's surface, as we can see in Figure 6.7.

We then tracked the particles, once again, out to 100 kpc and recorded their final postions on the sky, obtaining Figure 6.8.

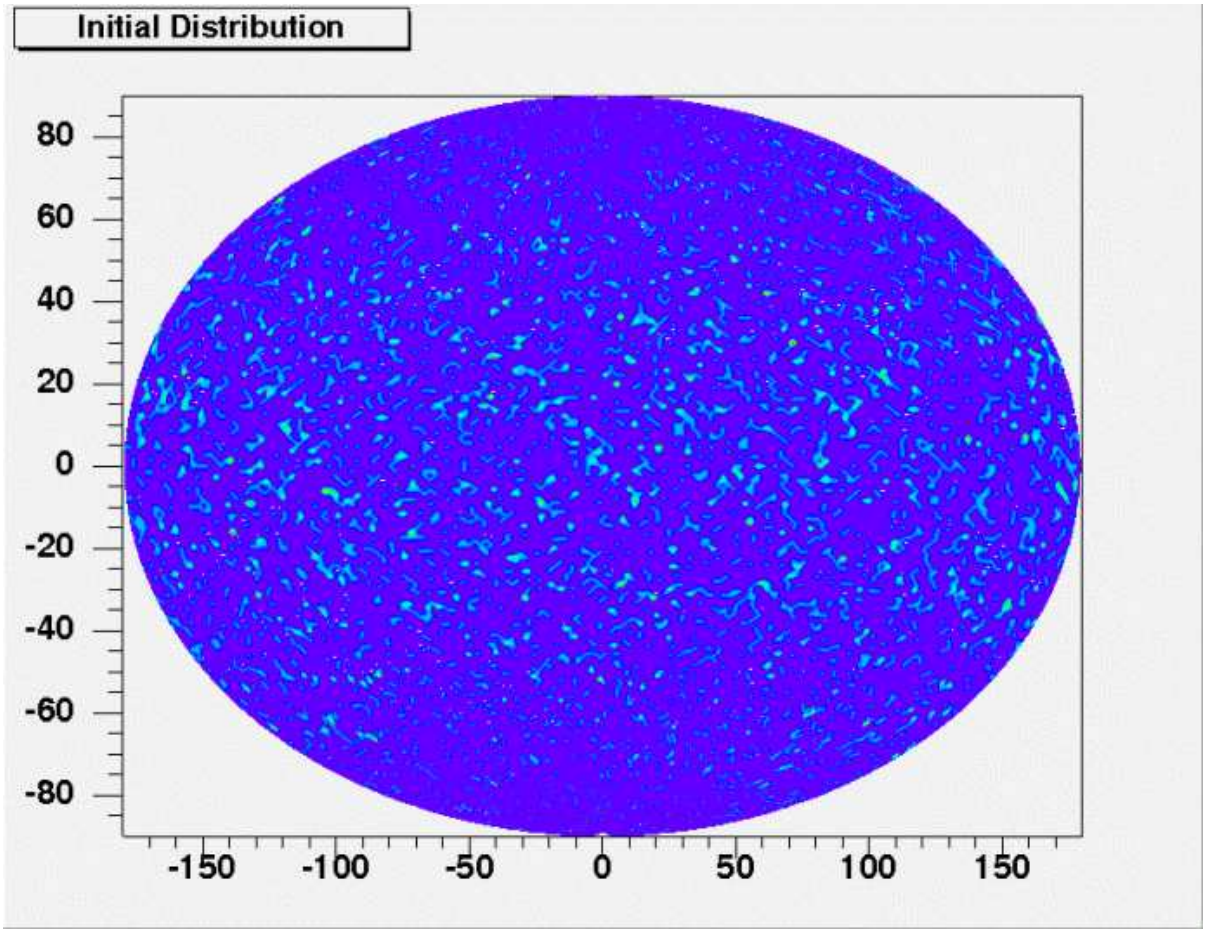


Figure 6.2: Initial Directions – 10 EeV

As we can see, the clustering of particles is similar in both models, though different enough to warrant running them both if we were looking for the direction of the clustering. However, since the power spectra scan the skies only looking for size of clusters, and the clustering is on order of the same size in both simulations, we can proceed choosing to run one or the other (in our case, the ASS model).

### 6.2.2 Extragalactic Magnetic Field Modeling

As has been discussed before, we are upper and lower limits on the extragalactic magnetic field. The upper limit is 1 nG, and the lower limit will be $10^{-12}$ G. Though even the upper limit seems small, we cannot discount the effect of the field outright, since the particles will be in contact with it for longer distances than they

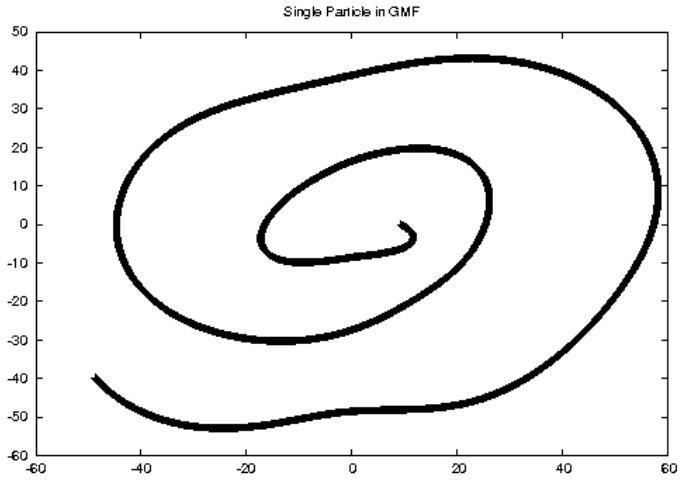


Figure 6.3: Single Particle Trajectory

will in the GMF. And, so, we generated 5000 particles, each with energy $10^{20}$ eV, and recorded their initial positions, as seen in Figure 6.9.

We then first applied the ASS model of the GMF. After the particle reached r = 25 kpc (around the edge of our galaxy), we turned on a constant EGMF. The first one tried was an upper limit of the EGMF ($B_{EGMF} \simeq 1$ nG). After 100 kpc in this field, we recorded the positions again, obtaining Figure 6.10.

We then tried a lower limit EGMF after 25 kpc, meaning that the EGMF would be a constant value of $\simeq 0.001$ nG out to 100 kpc. This yielded the final directions visible in Figure 6.11.

If we turn off the EGMF, and keep the GMF on all the way out to 100 kpc, we find the final directions of particles to be what we see in Figure 6.12.

Obviously, the GMF provides the greatest bending, with little additional bending coming from the EGMF. We will therefore focus on the GMF as we proceed.

## 6.3 Error Bars

In order to understand the results accumulated from the simulations, we must know how accurate they are. From simulation to simulation, results will always

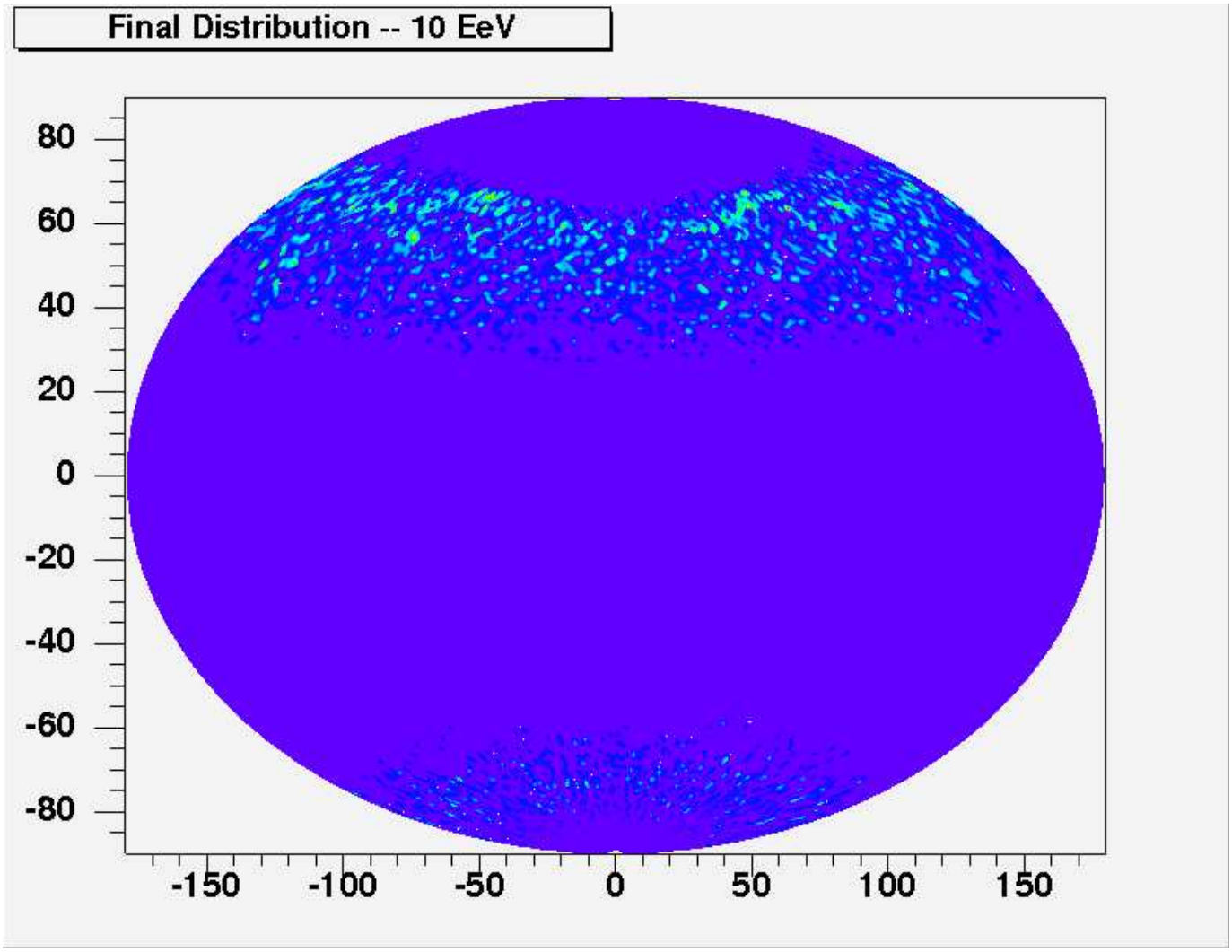


Figure 6.4: Final Positions – Aitoff

vary, and it is this variance we must quantify if we are to be sure that our results are conclusive. There are two ways we have done this here: the first is to simply run a large number of simulations, then compute the root-mean-square (RMS) of the results obtained and use that as the error bar; the second is to smear the points obtained in a Gaussian fashion.

The first method is the more straightforward of the two, both to understand and to execute. First, the simulation is run with $10^5$ particles of $E = 10^{20}eV$. We track each particle through the galactic magnetic field out to a spherical "shell" of 500 kpc. We do not take the extragalactic magnetic field into account here, since

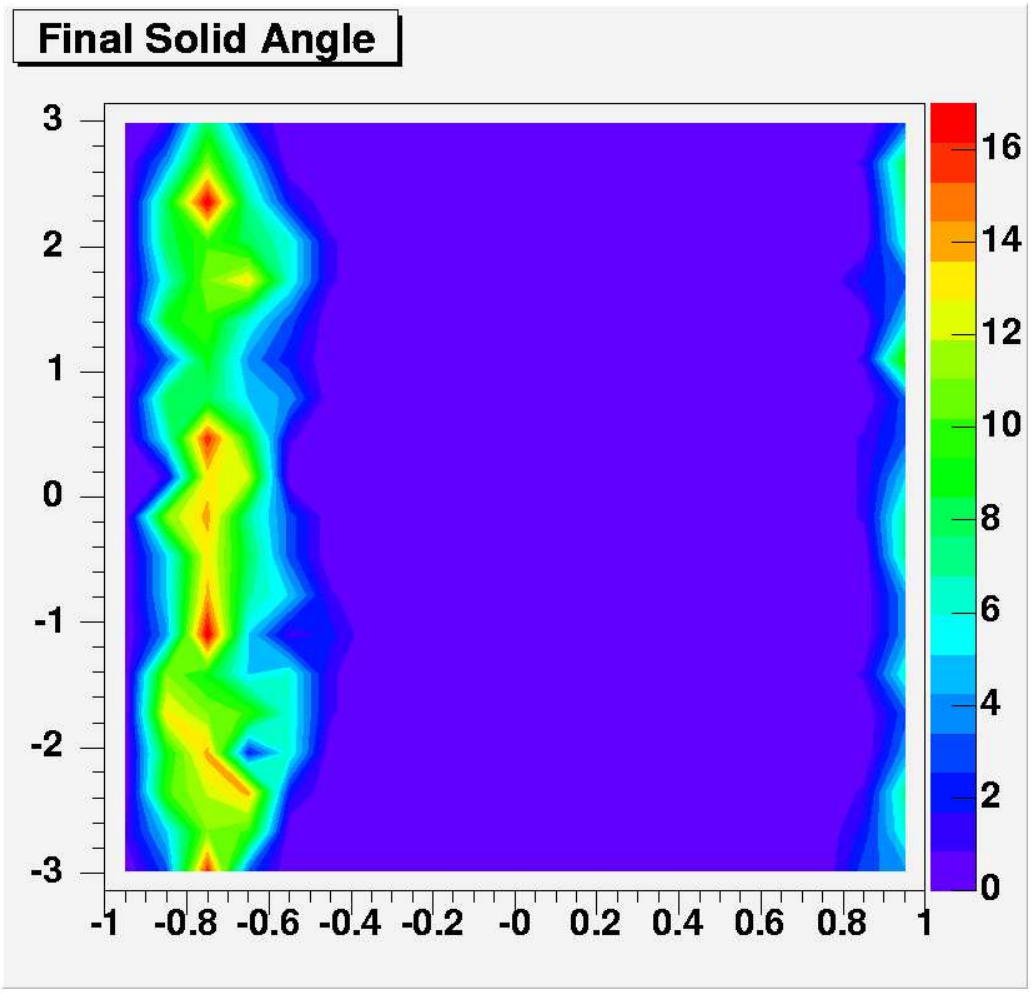


Figure 6.5: Final Directions at 100 kpc for E = $10^{19}$ eV

it is relatively insignificant, but rather extend the galactic magnetic field out past the galactic halo and usual cutoff of 20 kpc. This effectively makes the field constant, at a value on the order of $|B| \simeq 1$ $\mu$G. After finding the final positions of each particle, we compute the power spectrum of the distribution as previously discussed. In order to find the root-mean-square (RMS) deviation, we repeat this process 100 times, using 100 randomly-assigned homogeneous starting distributions. We keep track of each final distribution's $C_l$ values, then find the RMS by the usual method:

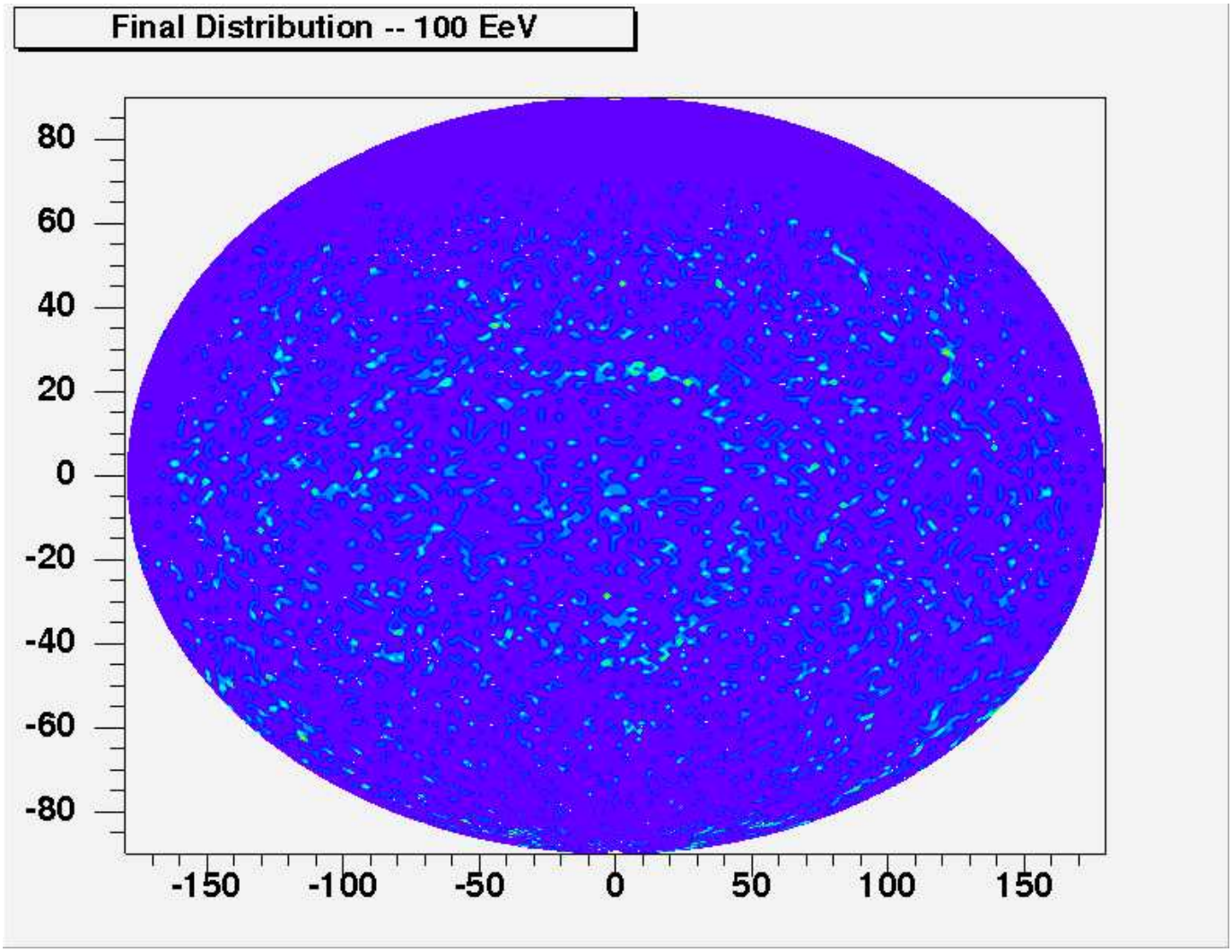


Figure 6.6: Final Directions at 100 kpc for E = $10^{20}$ eV

$$\sigma_{rms} = \sqrt{\frac{\sum_{trial=1}^{n} C_l}{n}} \tag{6.1}$$

where n is the total number of trials.

The second method involves taking each point in the aforementioned final distribution and smearing it a little bit in a Gaussian fashion. In order to do this, we first generate a Gaussian distribution of numbers from 0 to 1. We then assume the error in the angular measurement to be of order $\leq 1.5^o$. We finally have a simple equation to smear the final distribution:

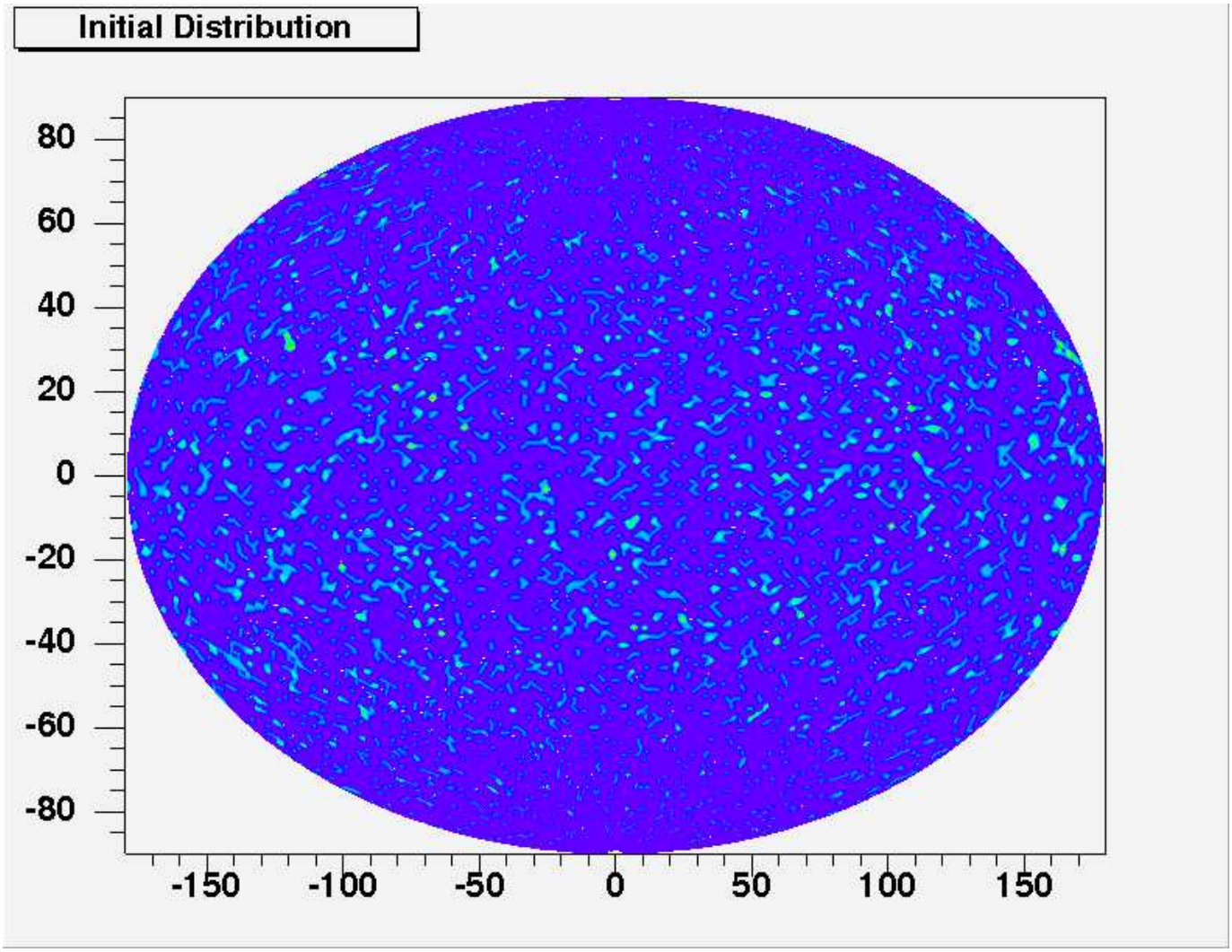


Figure 6.7: Initial Directions for E = $10^{20}$ eV – BSS Model

$$\theta_{new} = \theta_{old} + (\Delta\theta * y) \tag{6.2}$$

where y is the Gaussian-generated point. By doing this over and over and looking at the RMS of the distribution of points obtained, we have another way to estimate the error inherent to the distribution.

The error bar calculations were integrated into the power spectra calculations and yielded the following graphs:

The error bars of Figure 6.13 are on the order of $10^{-5}$ and are obviously negli-

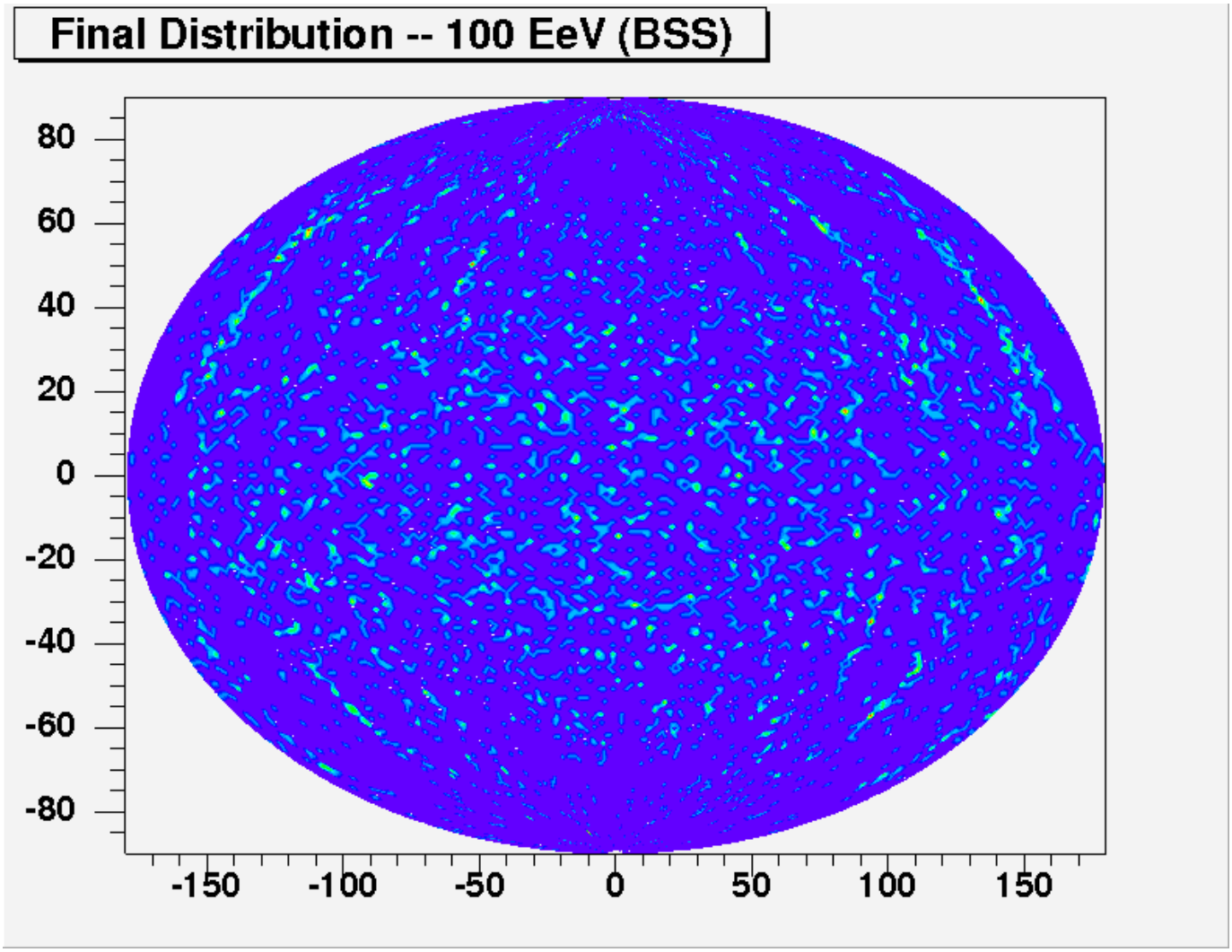


Figure 6.8: Final Directions at 100 kpc for E = $10^{20}$ eV – BSS Model

gible.

Since these are on the same order, we can assume all error bars negligible in the calculations to follow.

## 6.4 Weighting the Final Distributions

Given an initial distribution of particles, we divided up the earth's surface into equally-sized solid angle bins. We then found out which bin each particle belonged in, and assigned its position to be the center of that bin. And so we have a starting

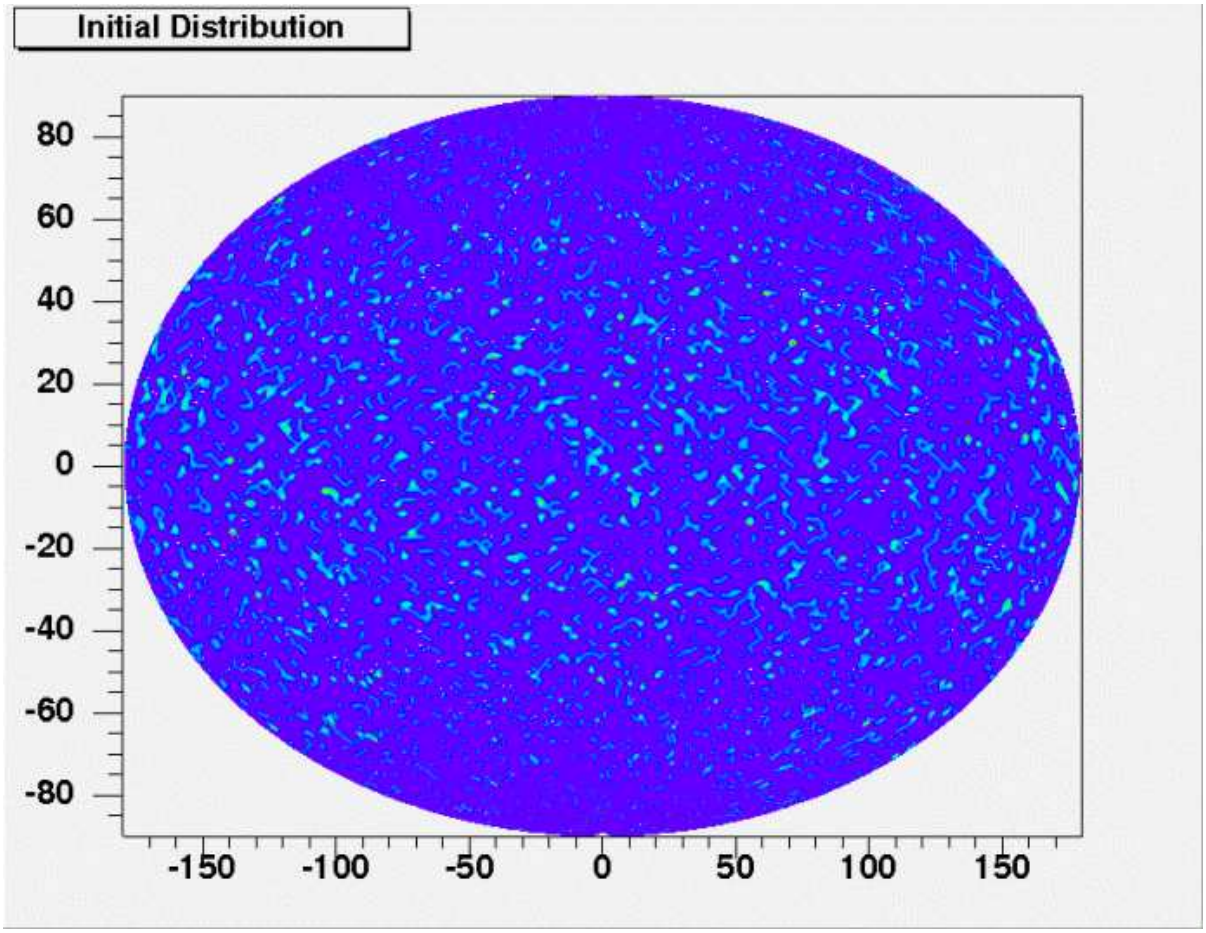


Figure 6.9: Initial Directions for 5000 Particles of E = $10^{20}$ eV

distribution consisting of roughly equal numbers of particles in each solid angle bin.

The size of the starting bins is determined by the angular resolution of the Pierre Auger Observatory, which is between $1^o$ and $2^o$. So,

$$d\Omega = 2\pi(1 - \cos 2^o) \tag{6.3}$$

where $d\Omega$ is equal to the area of each solid angle bin. Another way to say this is that the number of bins corresponds directly to the angular resolution of the bins as:

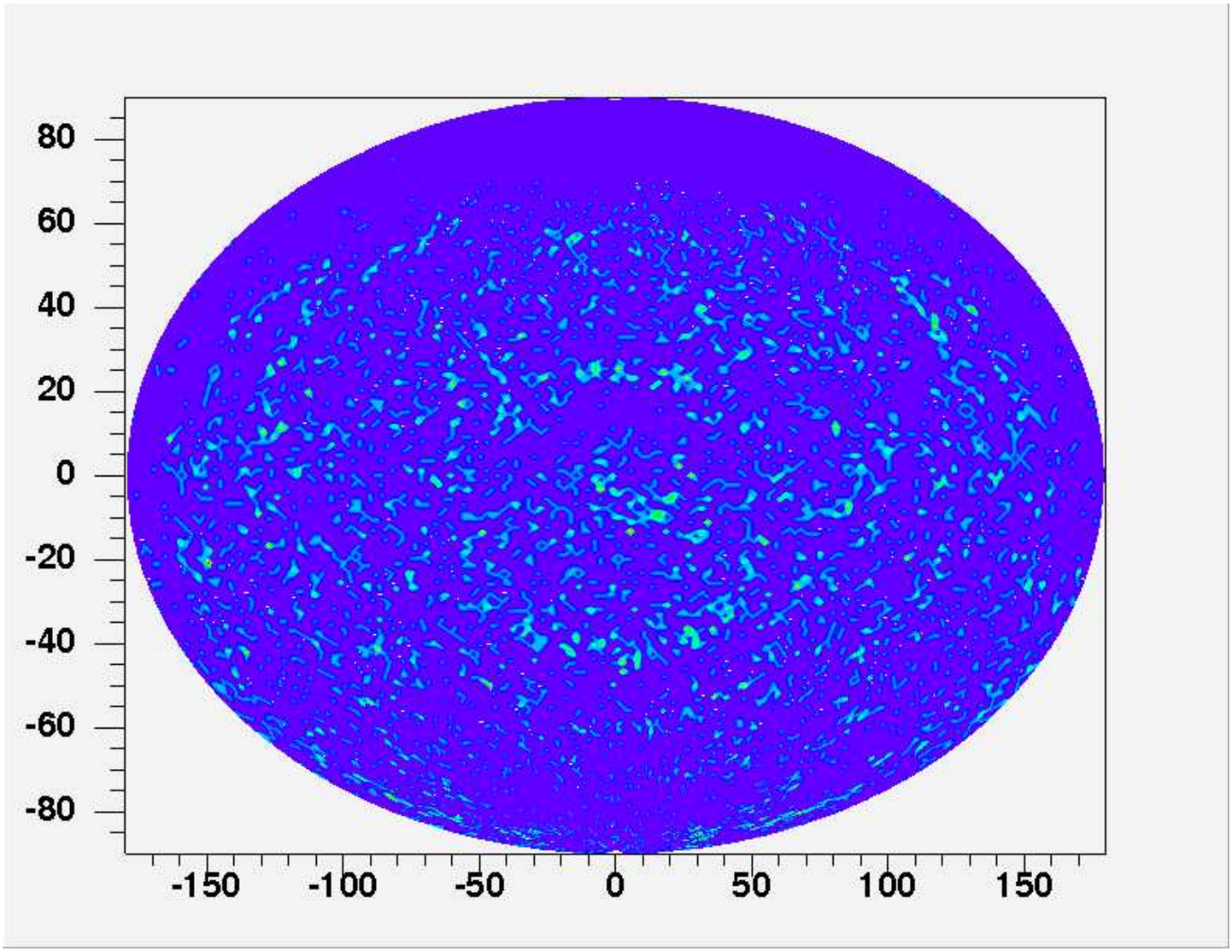


Figure 6.10: Final Directions for 5000 Particles of E = $10^{20}$ eV – Upper Limit of EGMF

$$n_{bins} = \sqrt{\frac{2}{1 - \cos\alpha}} \tag{6.4}$$

where $\alpha$ is the angular resolution. For $\alpha = 1^o$, $n_{bins} = 115$. For $\alpha = 2^o$, $n_{bins} = 57$. In order to match up the angular resolution of the solid angle bins with the angular resolution of the PAO, then, we chose to form 60 equally-sized bins for $\cos\theta$ and $\phi$, meaning we wound up with 3600 total initial starting bins.

We can see, then, that, if we are to begin with 5000 particles, there should be an average of 5000/3600 particles per bin, or roughly 1.4, which is what we've

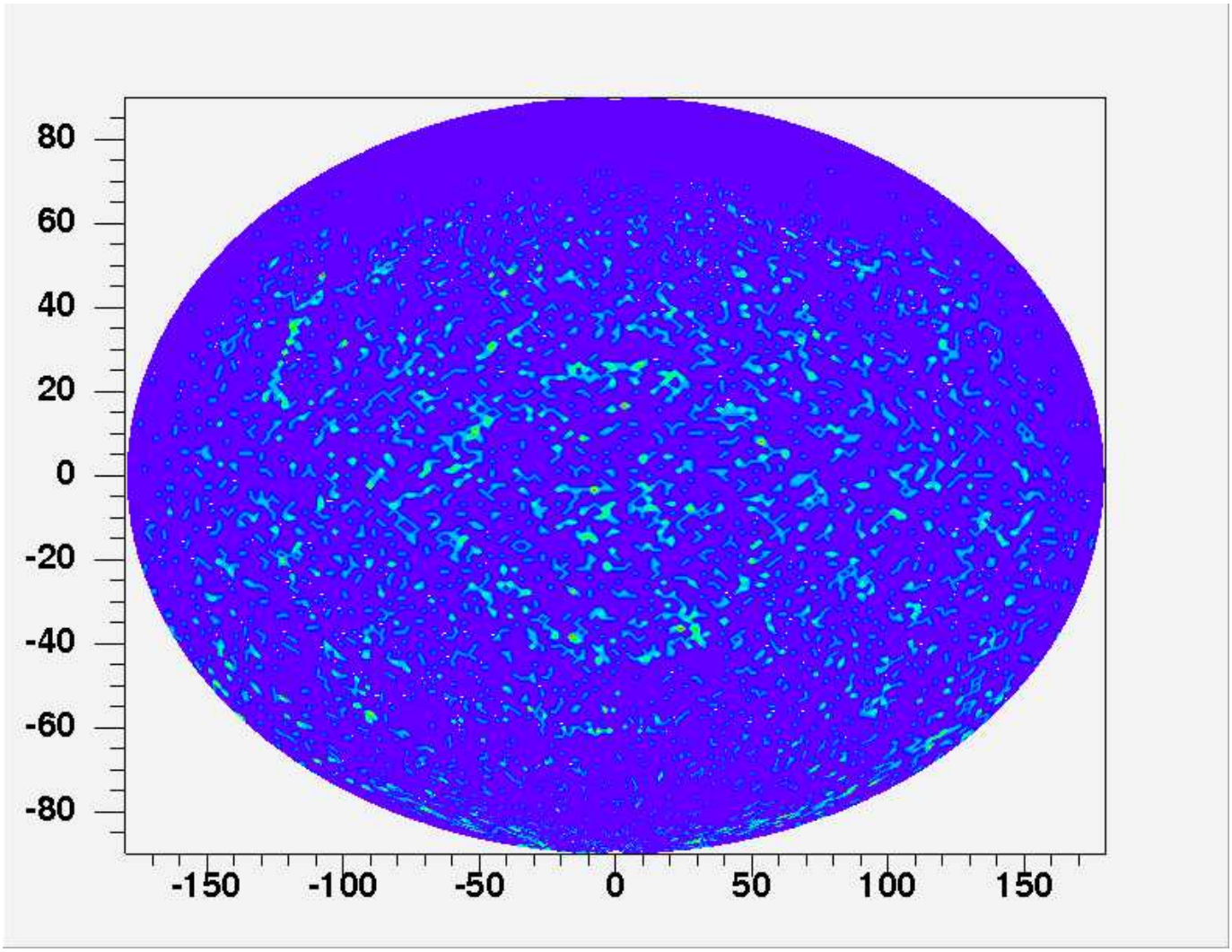


Figure 6.11: Final Directions for 5000 Particles of E = $10^{20}$ eV – Lower Limit of EGMF

obtained in Figure 6.15.

Once the initial positions have been set, we tracked the particles out to a "shell" at a certain distance, and record their final positions on the sky. Once again, we divided up the sky into equally-sized solid angle bins, and found out which bin each particle has ended up in. Again, we assign the center of that bin to be the particle's final coordinate.

Obviously, after the particles have undergone bending due to the GMF for long distances, they are no longer going to be equally spaced. As such, there will no

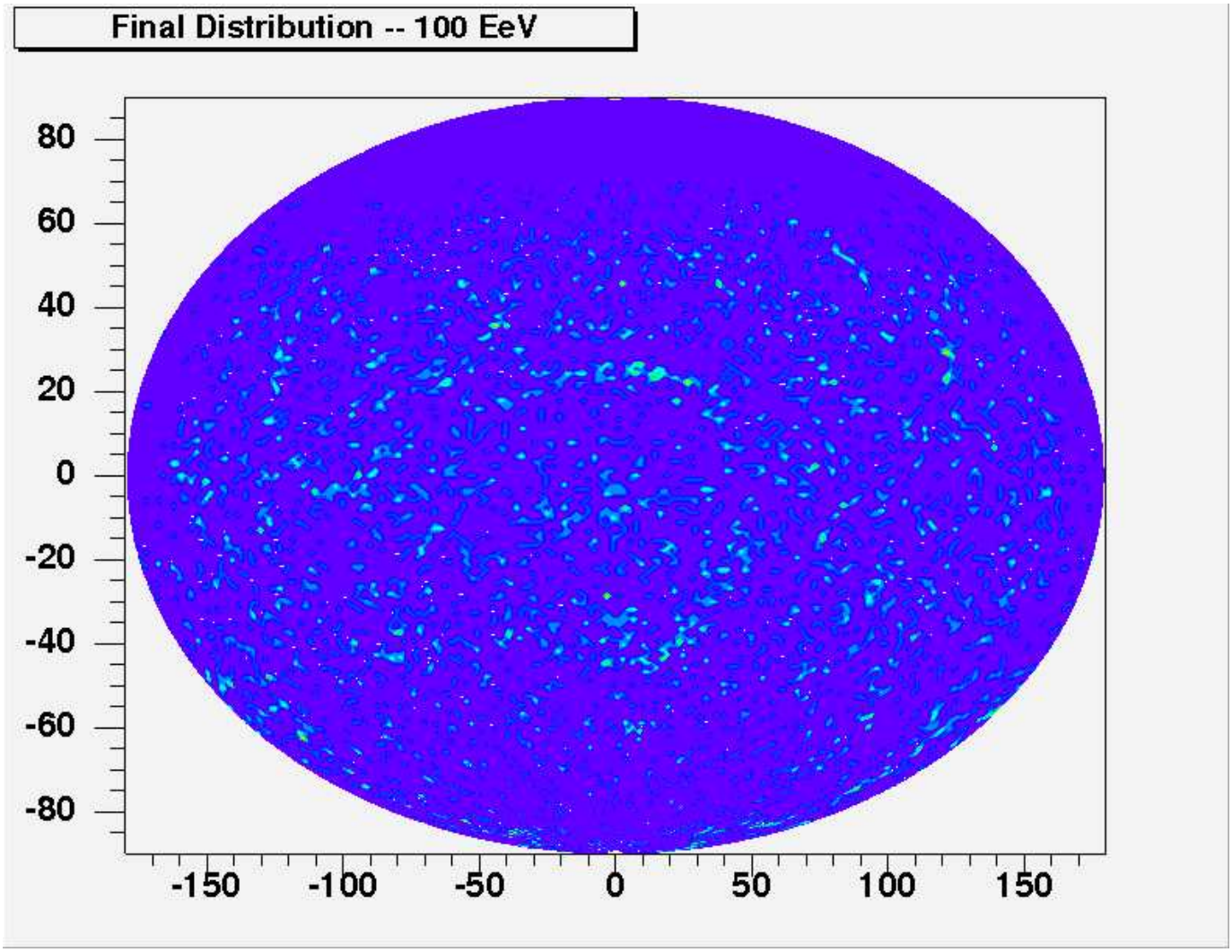


Figure 6.12: Final Directions for 5000 Particles of E = $10^{20}$ eV – Only GMF

longer be equal numbers of particles in each bin in the final distribution. Instead, there will be clustering in some places, and no particles in others. If there are no particles in a particular bin, we ignore it, since a particle from there won't be detected at the earth's surface. Otherwise, we simply count up the numbers of particles in each bin, and use them as weights. For example, if one of the final bins turns out to have 20 particles clustered in it, that bin will have a weight of 0.05. This means that, were a single particle to come from that bin, it would be smeared into 20 initial bins on the earth's surface, with each of those bins inheriting 0.05 of that initial particle. In this manner, we can find the probable distributions at the

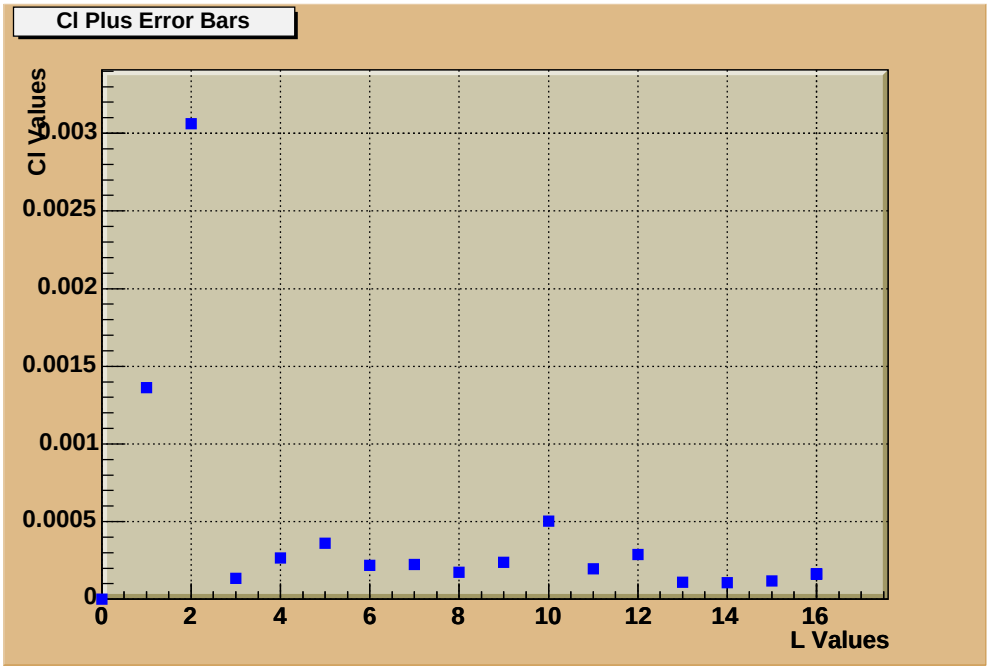


Figure 6.13: Gaussian Smear Error Bars

earth's surface of any distribution of sources on the sky, so long as we've discovered the weighted values of the bins at the distance they are from us.

With this in mind, we have chosen the following distributions on which to focus: (1) an isotropic distribution of sources, (2) the distribution of nearby galaxies, taken from the Tully-Fisher catalogue [40], and (3) the distribution of nearby AGNs [39].

## 6.5 Isotropic Distribution

In order to see what the power spectrum from an isotropic distribution of sources will likely appear to be at the earth's surface, we then take the final generated distribution of weights assigned to bins and assign those weights to the initial distribution of bins. These weights are the ones that will be passed to the power spectrum calculation, in order to find out what the weighted power spectrum of an isotropic distribution of sources would look like at the earth's surface.

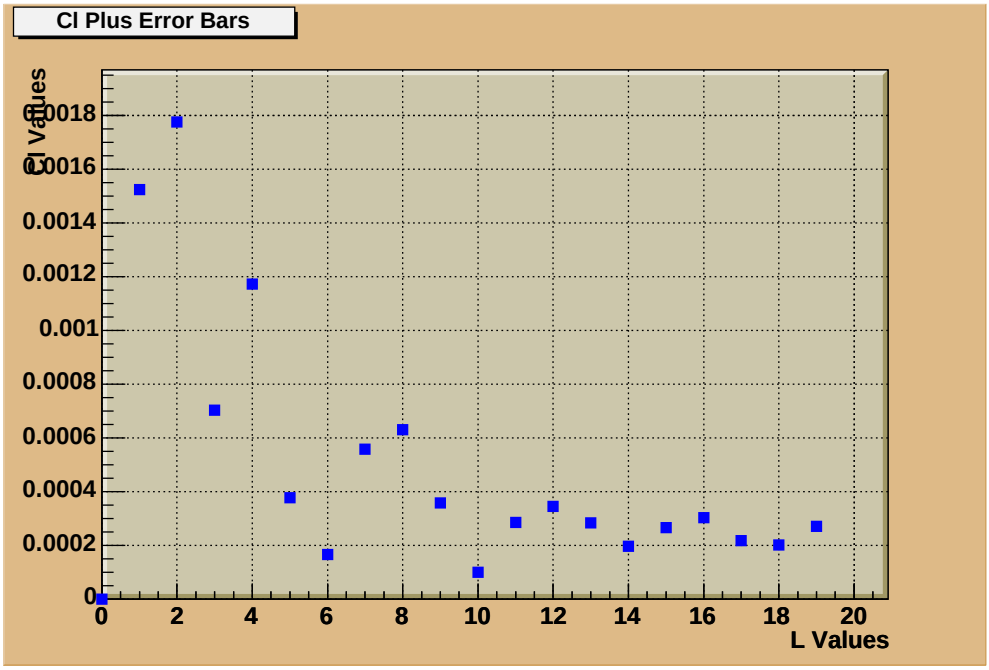


Figure 6.14: Multiple Trial Error Bars – 1000 Trials

For an isotropic distribution of sources corrected for detector exposure, then, we find a relatively dipolar power spectrum with fewer lower order signatures, as seen in Figure 6.16.

## 6.6 Different Primaries

Since the composition of the UHECR primary is still a matter of debate, we also tried following the trajectories of other primary particles. Specifically, we tried iron nuclei, electrons, and gamma rays.

As expected, the gamma rays were not bent at all by the magnetic field, since they are uncharged (see Figures 6.17 and 6.17).

In contrast, the electrons and iron nuclei are both noticeably bent, as we can see in Figures 6.19 and 6.20.

Since the gamma rays were not bent at all, there was no need to see how the weighting process would change the initial distribution of points at the earth's

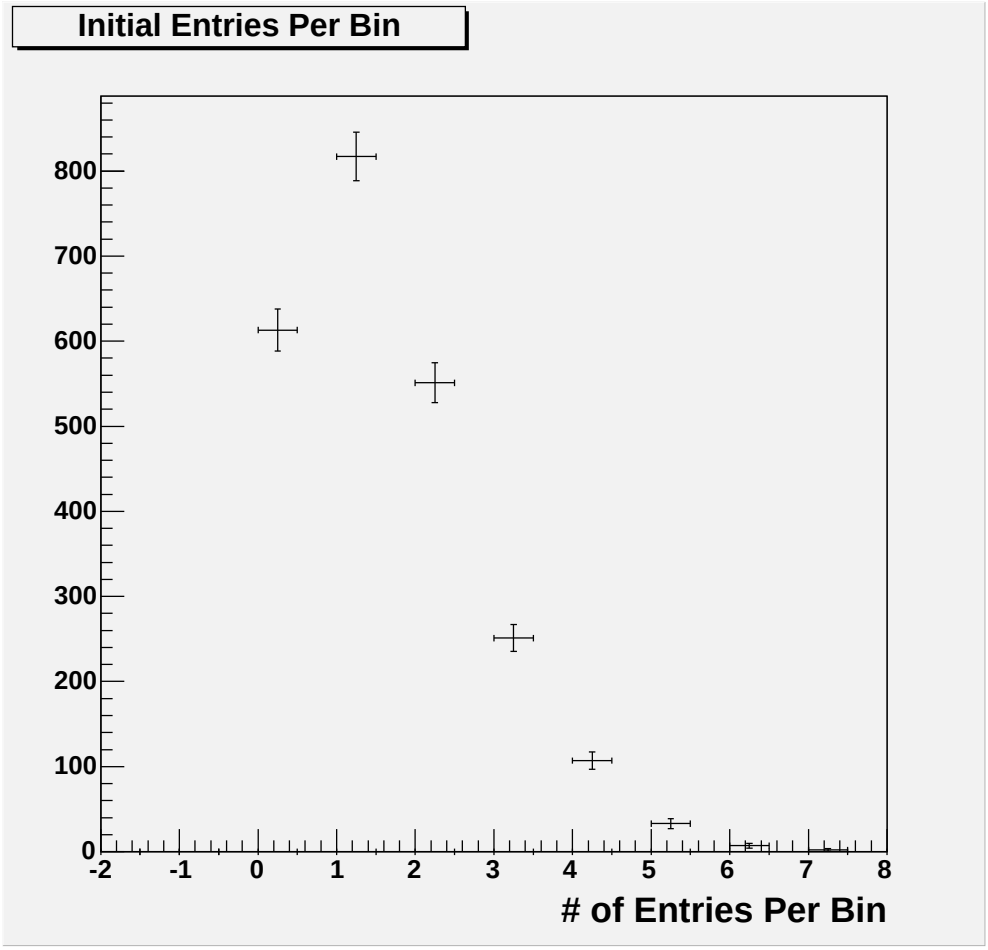


Figure 6.15: Initial Entries Per Bin

surface. The electrons' final positions appeared to be so similar to the protons', as expected, that repeating the weighting process seemed redundant. However, the iron nuclei were bent more even than the protons, and so the final positions and weights associated therewith were recorded. Assuming an isotropic distribution of sources once again, we then calculated the weighted power spectrum for iron nuclei.

The iron nuclei appear different than the protons previously analyzed, in that their lower order moments appear to be enhanced in places when compared to the lower order moments of the proton primaries. This can be seen more easily in Figure 6.22.

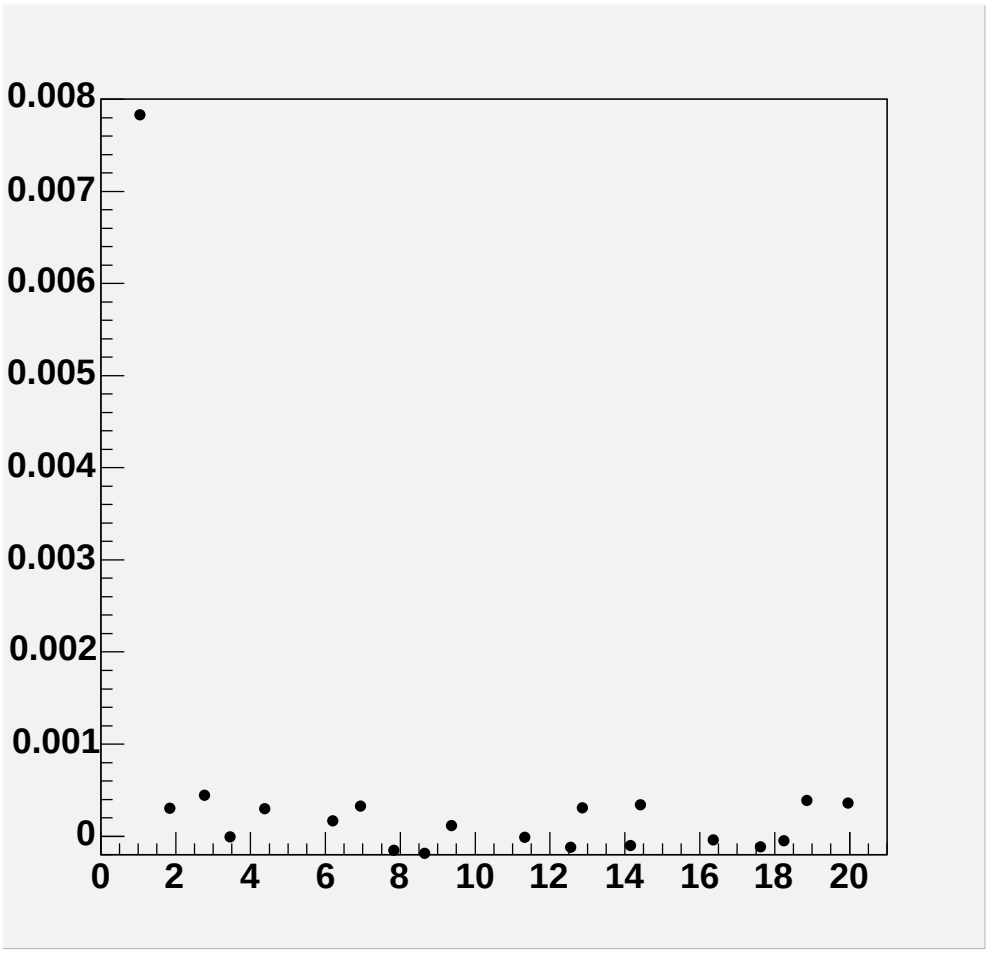


Figure 6.16: Weighted Power Spectrum for an Isotropic Source Distribution

## 6.7 Comparison to AGN Distribution

Since the appreciable bending due to the GMF only occurs within 100 kpc, we can reapply the weights calculated at that distance and find a new power spectrum (see Figure 6.23).

Obviously, there appears to be an enhancement of the $l = 1$ value, indicating a possible dipole distribution of arrival directions at the Earth's surface. Iron nuclei also display this enhancement, as we can see in Figure 6.24.

Again, comparing the two results on the same plot with a log scale displays the enhancement of the bending and clustering experienced by the iron nuclei, as can be seen in Figure 6.25.

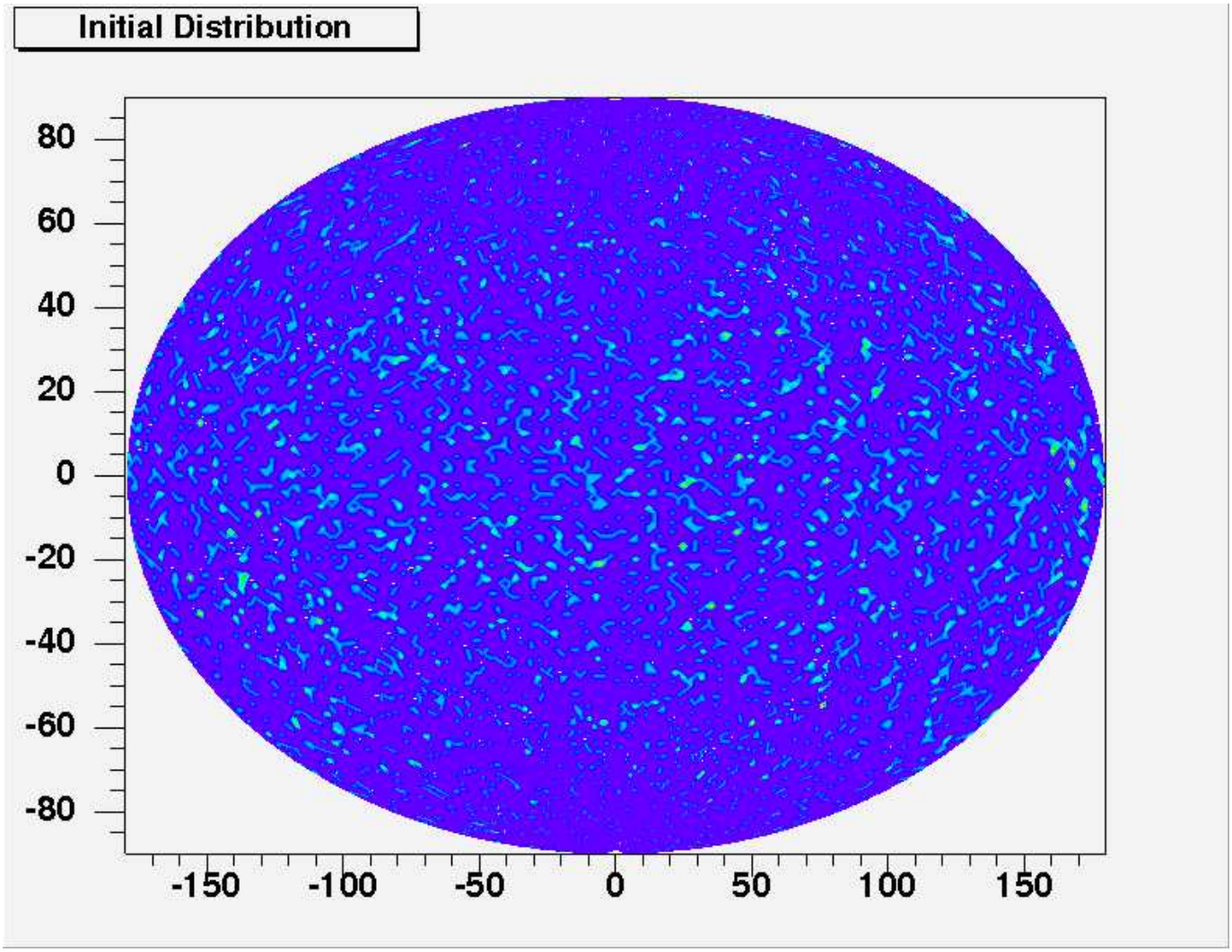


Figure 6.17: Initial Directions for Gamma Rays

## 6.8 Comparison to Matter Distribution

Alternately, we can consider all galaxies from the Tully-Fisher catalogue [40] within 50 Mpc to be possible sources, weight them the same way, and obtain Figure 6.26.

Once again, there appears to be a dipole-like enhancement, though this time it appears even more pronounced. The iron nuclei, in particular, seem to be the most affected, as can be clearly seen in Figure 6.28.

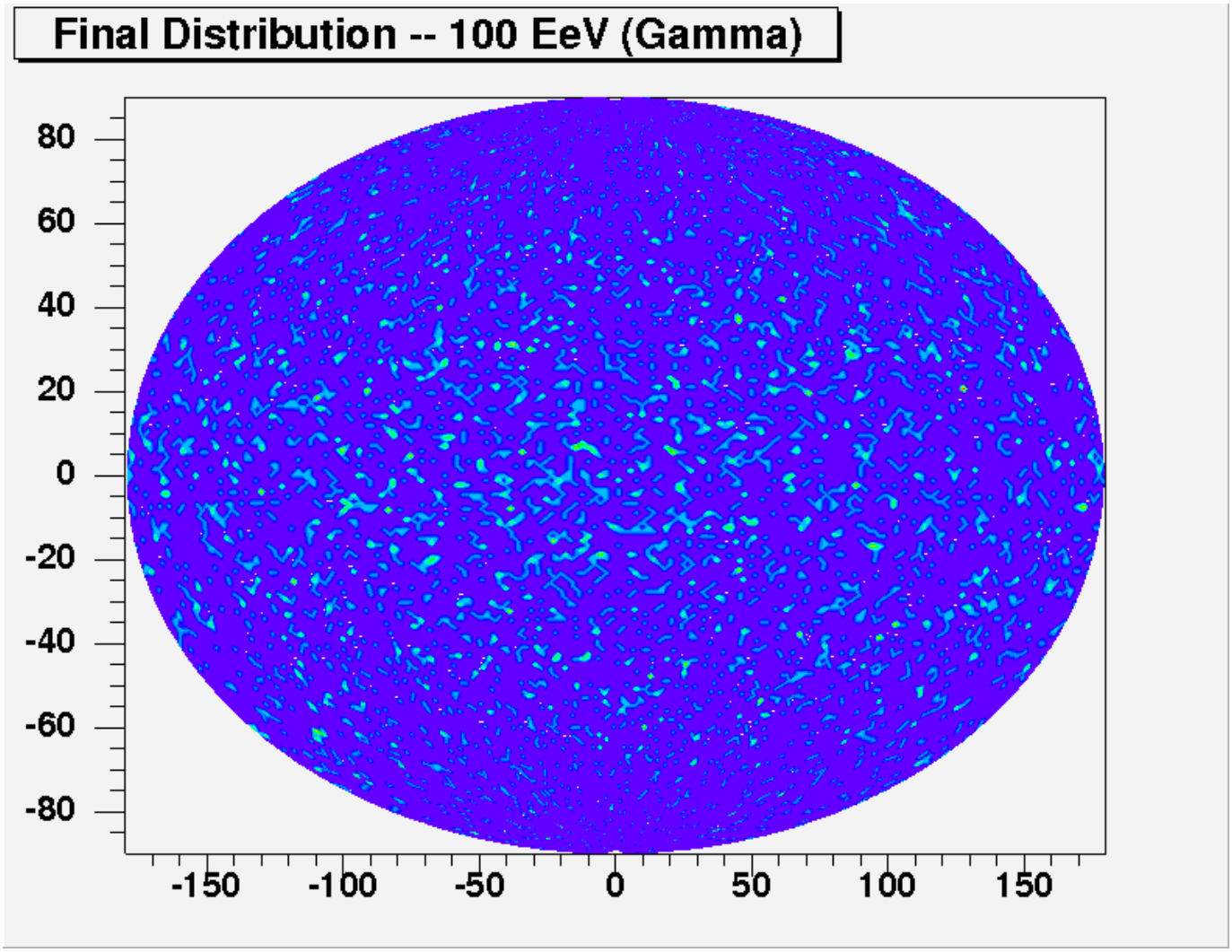


Figure 6.18: Final Directions for Gamma Rays at 100 kpc

## 6.9 Comparison to PAO Data

The PAO has been collecting data for the last few years, yielding an event list with over 800,000 values thus far. Using all values, we have calculated the power spectra for the data collected at different energy cuts, after correcting for the exposure of the detector as previously discussed. We concentrate on particles of $10^{19}$ eV and higher, obtaining Figure 6.29 for the $2140$ events recorded. If instead we only look at post-GZK events only, we obtain Figure 6.30 for the 34 events obtained to this date.

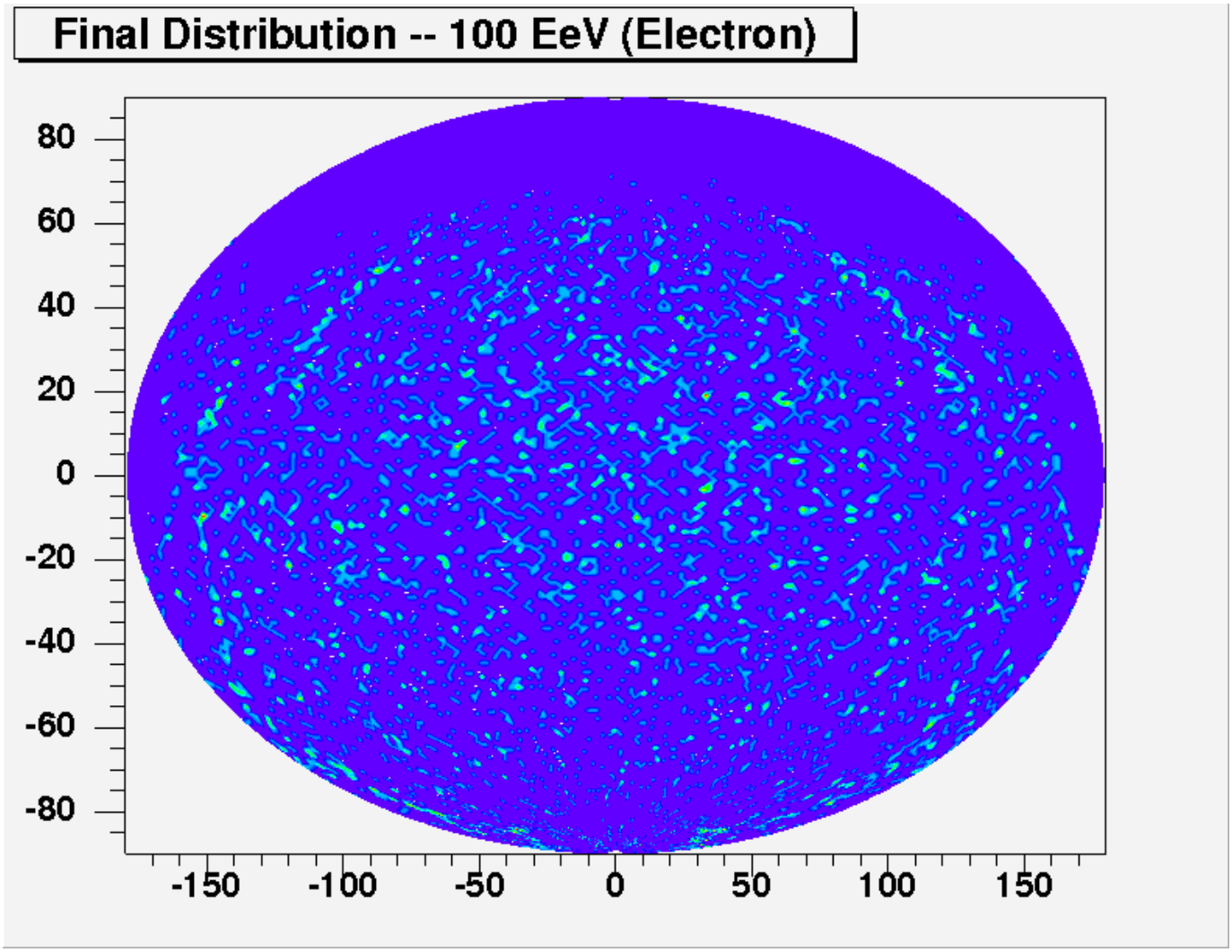


Figure 6.19: Final Directions for Electron Primaries at 100 kpc

The obvious dipole moment confirms our thoughts of how the data will look on half the sky, which is what we saw in Figure 4.8.

## 6.10 Conclusions

The results obtained for the higher energy particles detected appear to coincide with the results obtained for nearby galaxies and AGNs very well. However, as previously shown, since the results of the data are for only half the sky, the dipole moment is enhanced greatly. The fact that the dipole moment is not as pronouced

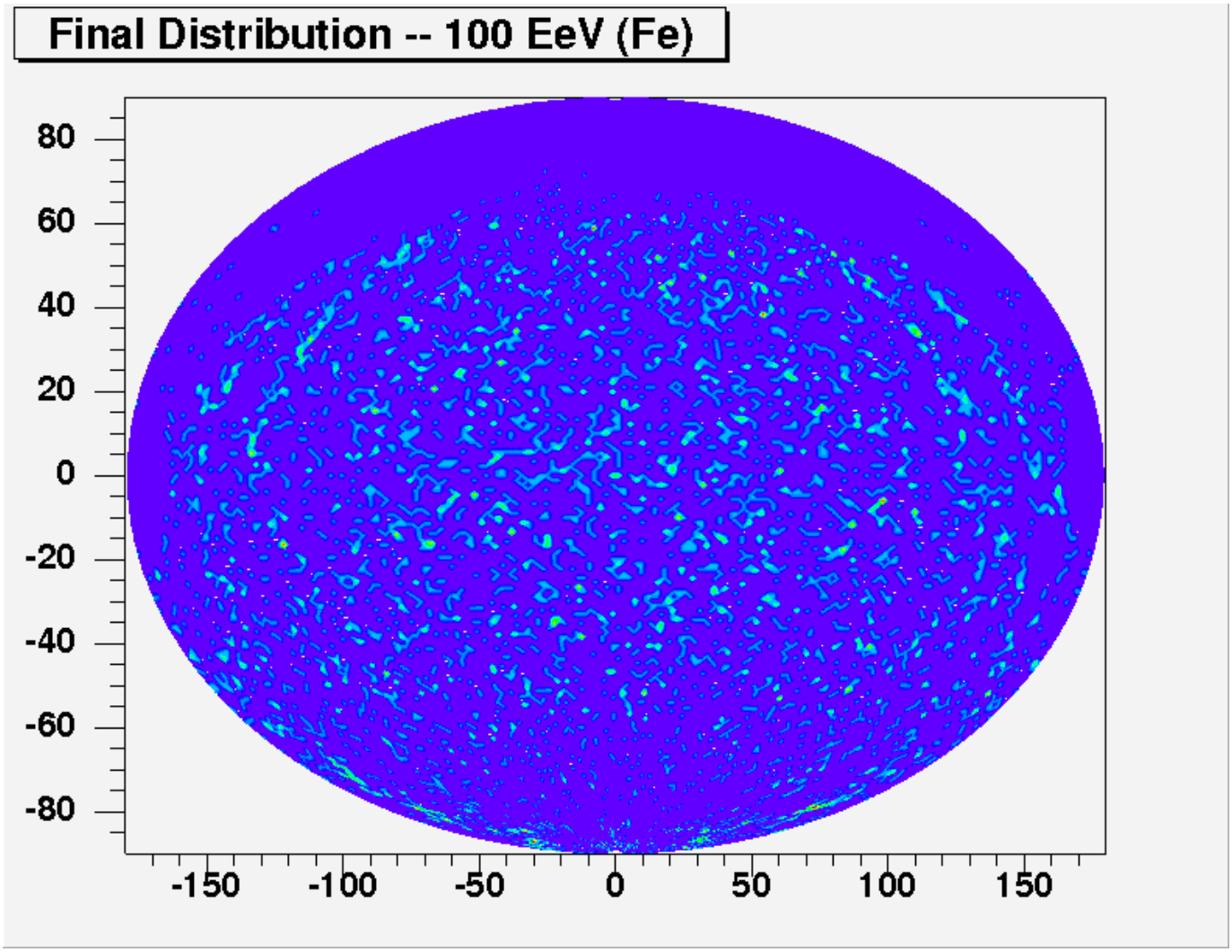


Figure 6.20: Final Directions for Iron Nuclei at 100 kpc

as we saw for iron nuclei coming from the nearby matter distribution can allow us to draw some tentative conclusions about the composition of these particles. Namely, it appears likely at this point that the majority of the particles incident on the earth's surface are lighter than iron nuclei, or, more to the point, protons. As for the particles' origins, we can only definitively conclude whether or not these particles are indeed resultant from AGN acceleration, or the acceleration of some other galactic origin, once the proposed Northern site of the PAO is constructed.

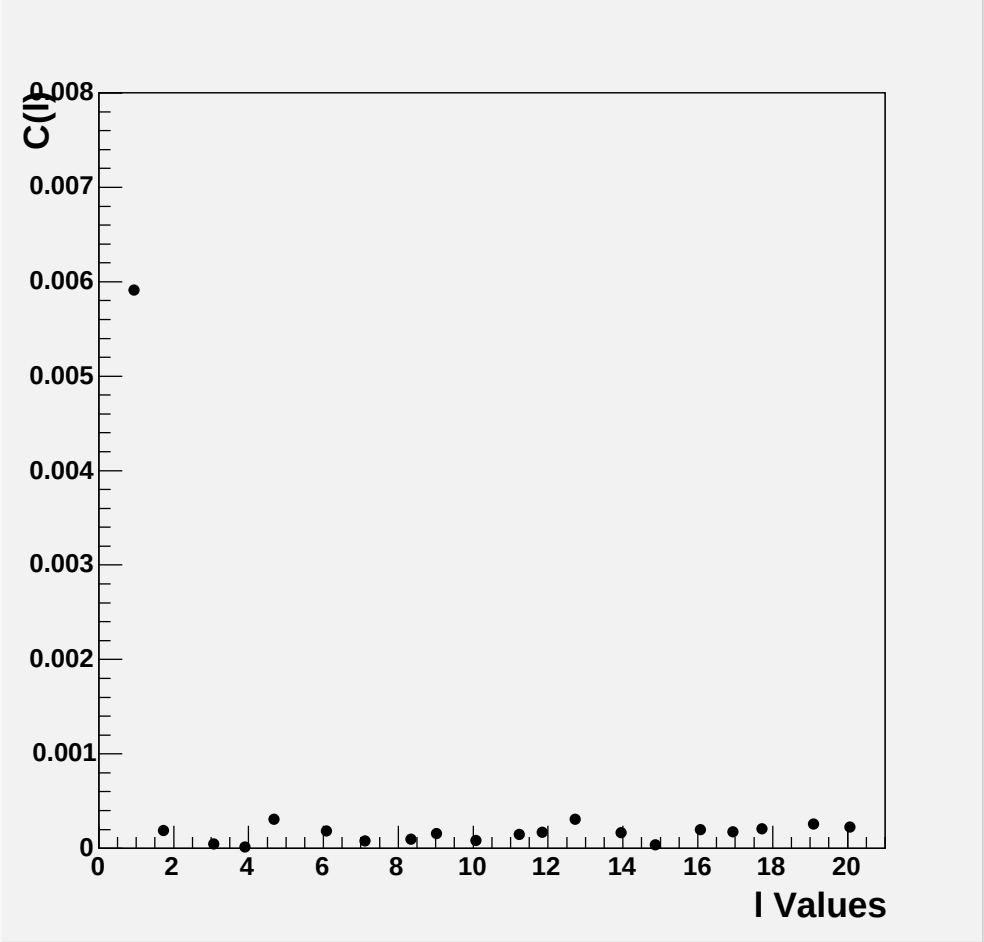


Figure 6.21: Weighted Power Spectrum for an Isotropic Source Distribution – Iron Nuclei

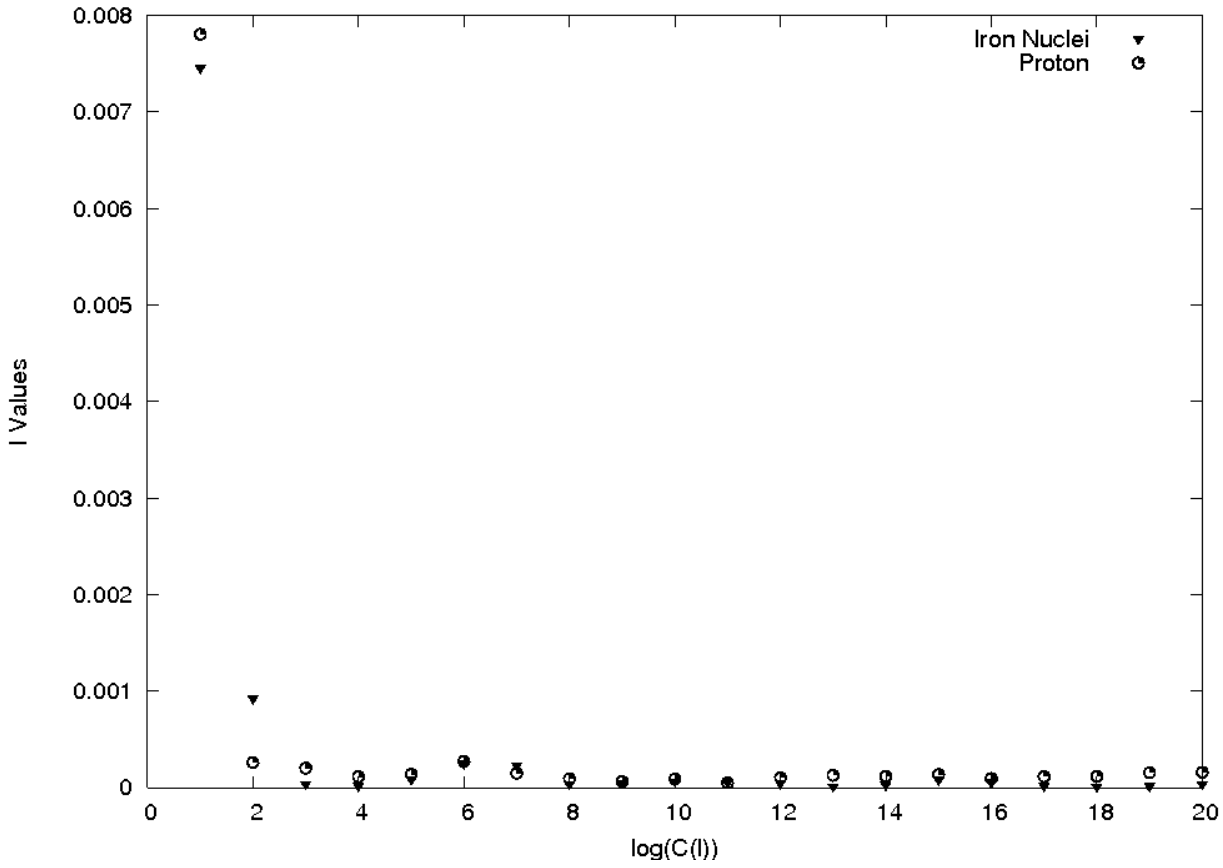


Figure 6.22: Weighted Power Spectrum for an Isotropic Source Distribution – Iron Nuclei vs. Protons

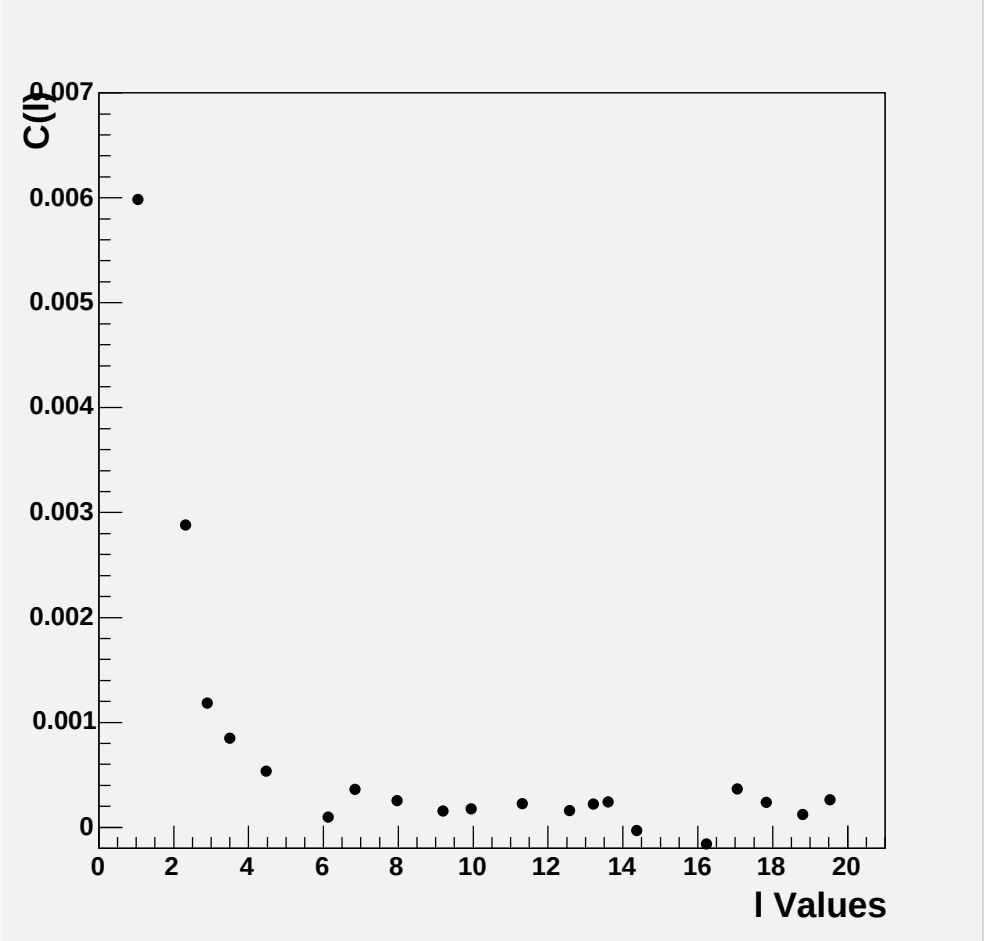


Figure 6.23: Weighted Power Spectrum for the AGN Distribution

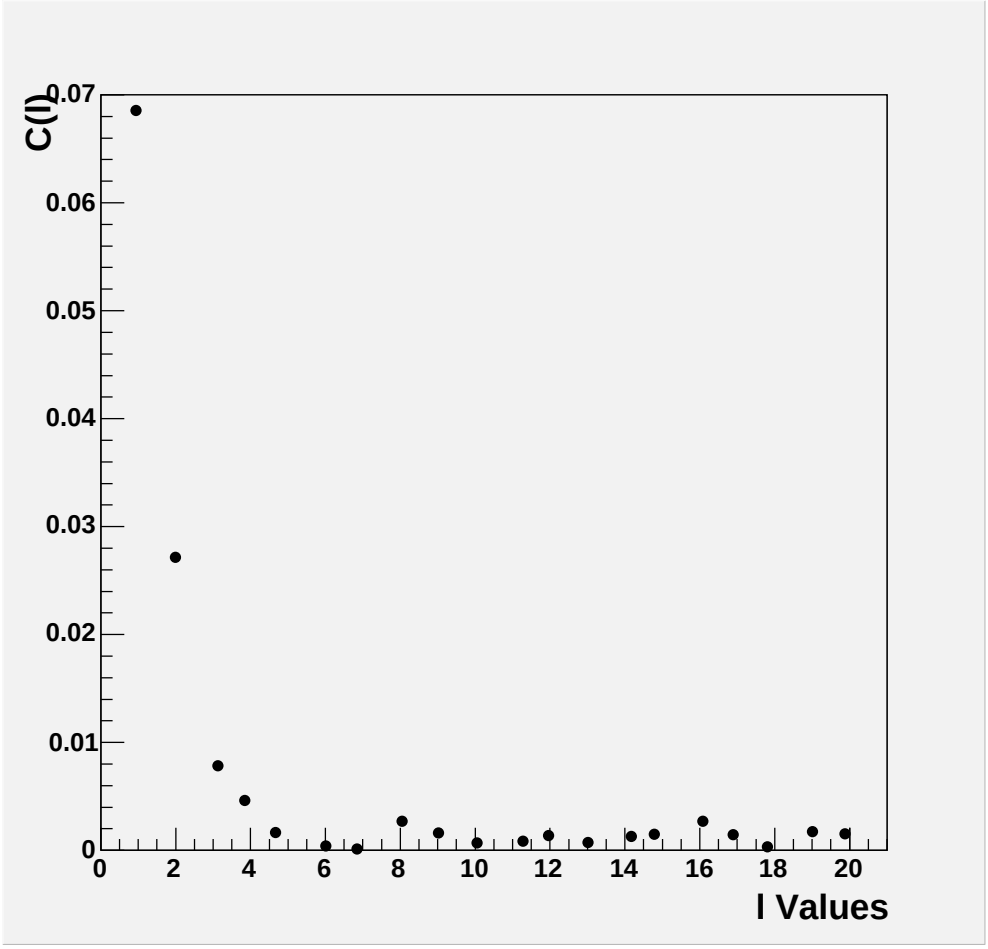


Figure 6.24: Weighted Power Spectrum for the AGN Distribution – Iron Nuclei

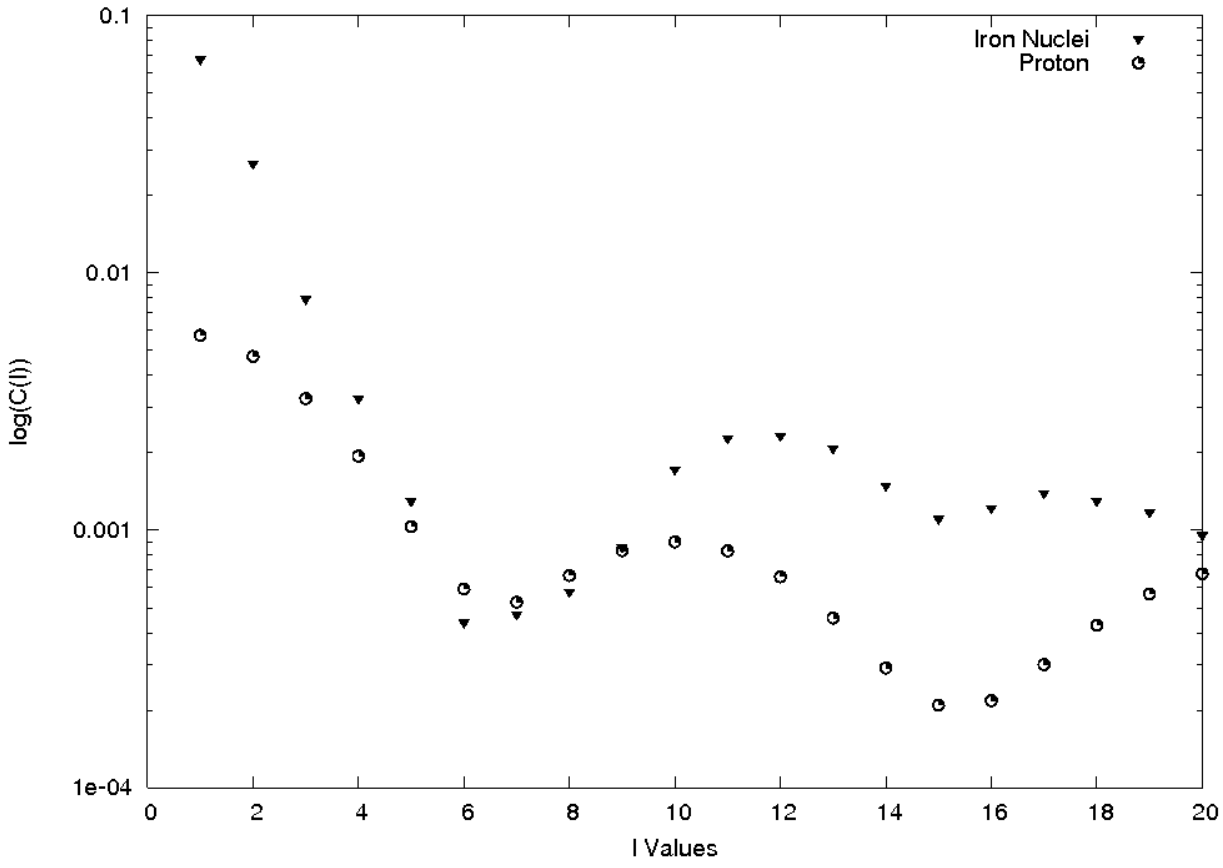


Figure 6.25: Weighted Power Spectrum for the AGN Distribution – Iron Nuclei vs. Protons

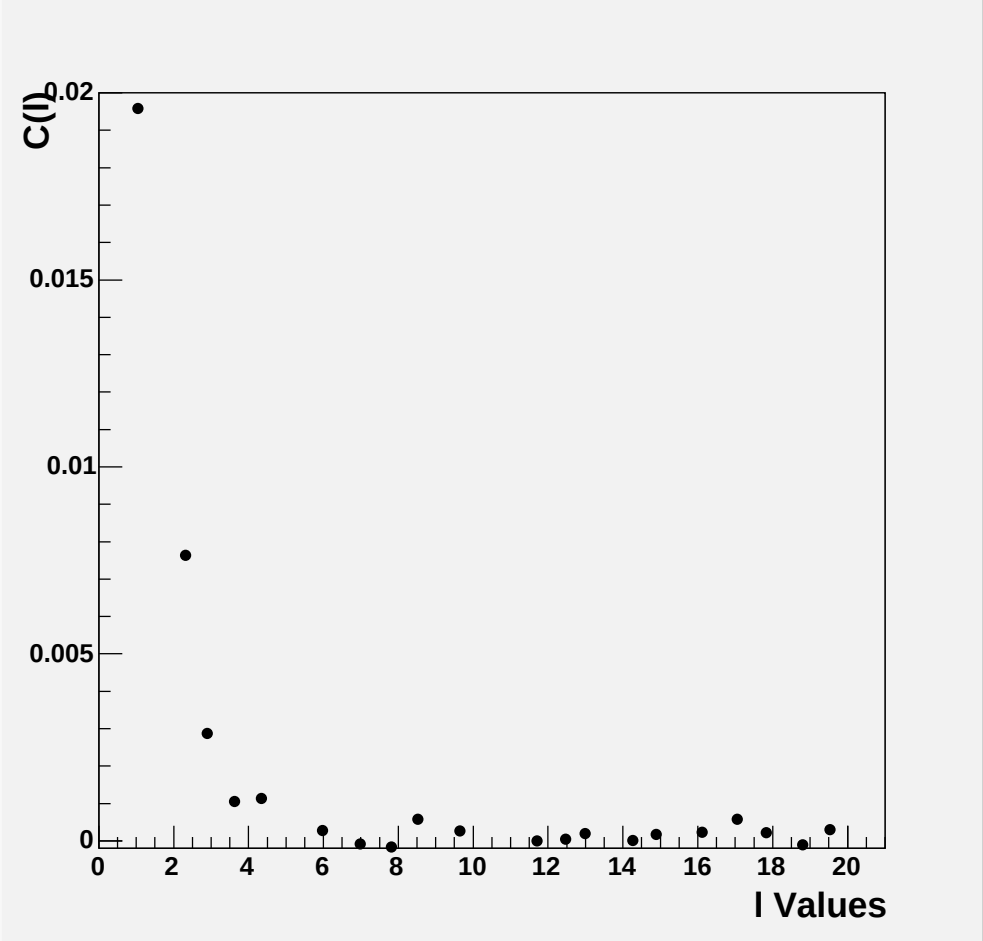


Figure 6.26: Weighted Power Spectrum for Nearby Matter Distribution

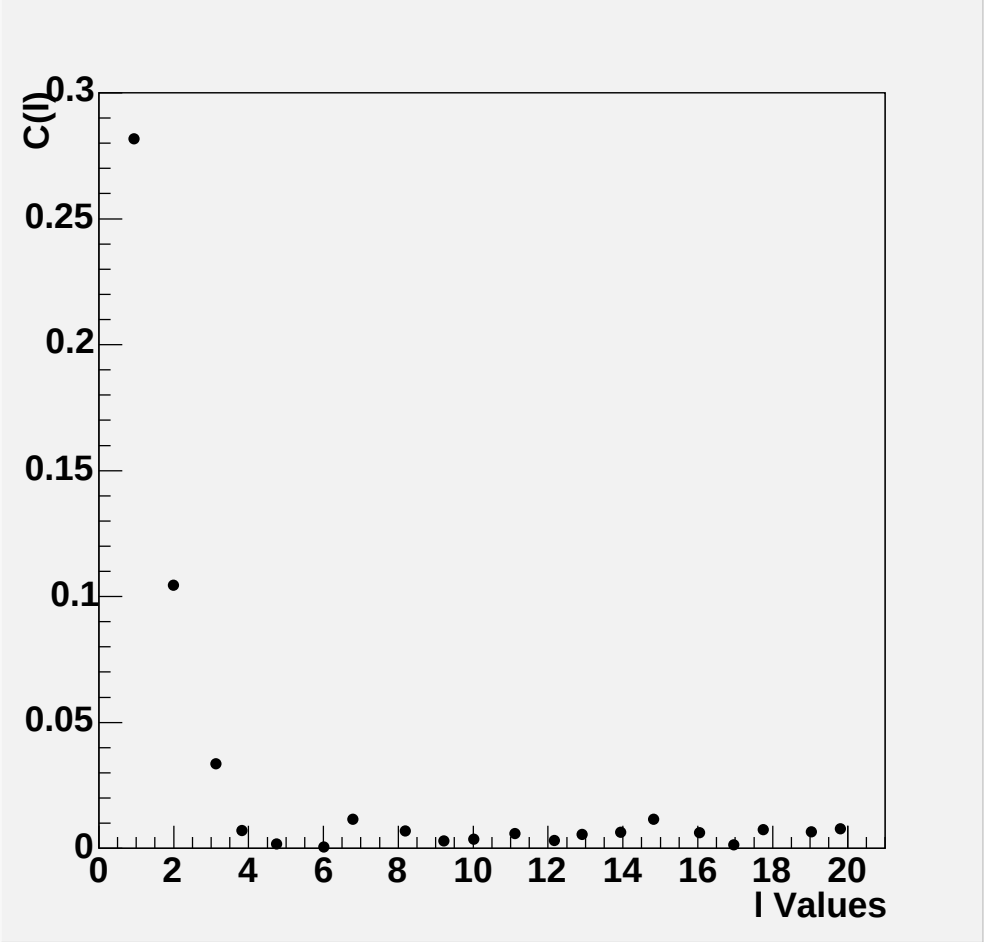


Figure 6.27: Weighted Power Spectrum for Nearby Matter Distribution – Fe Nuclei

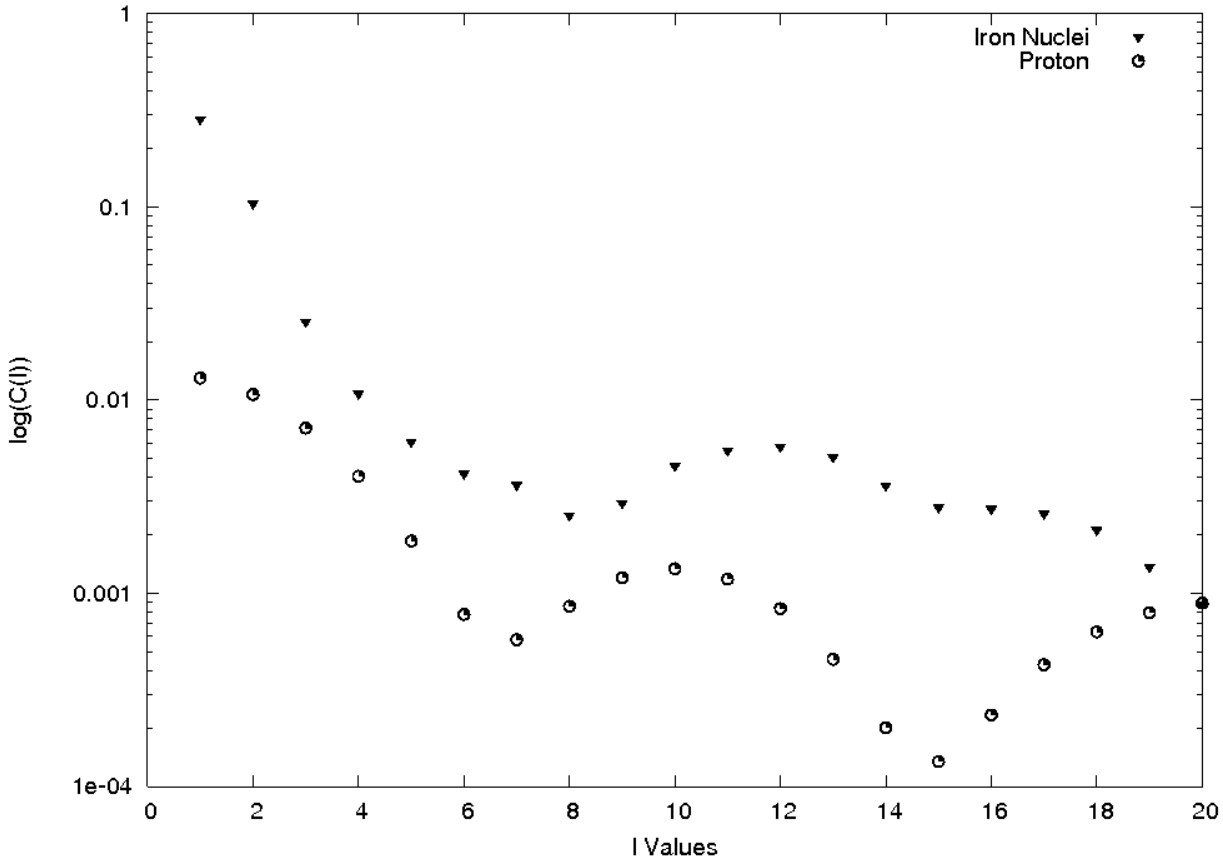


Figure 6.28: Matter Distribution – Iron Nuclei vs. Protons

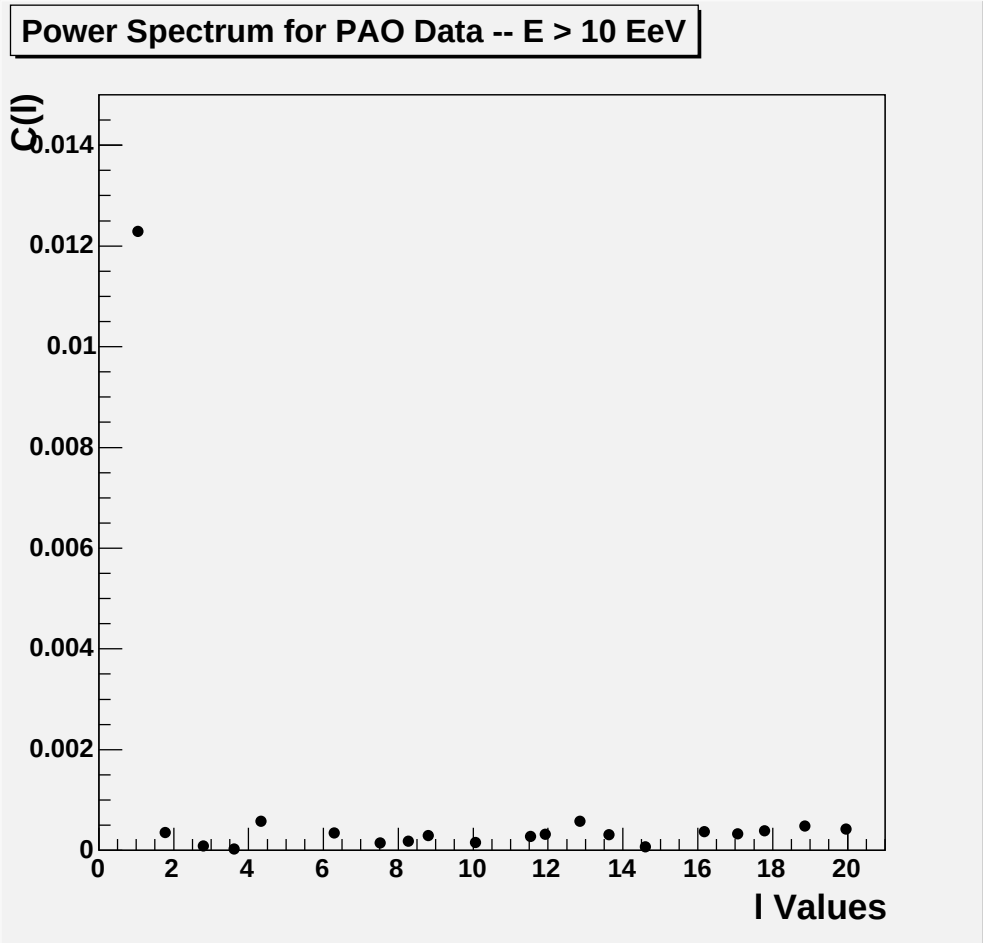


Figure 6.29: Power Spectrum for PAO Data with E above 10 EeV

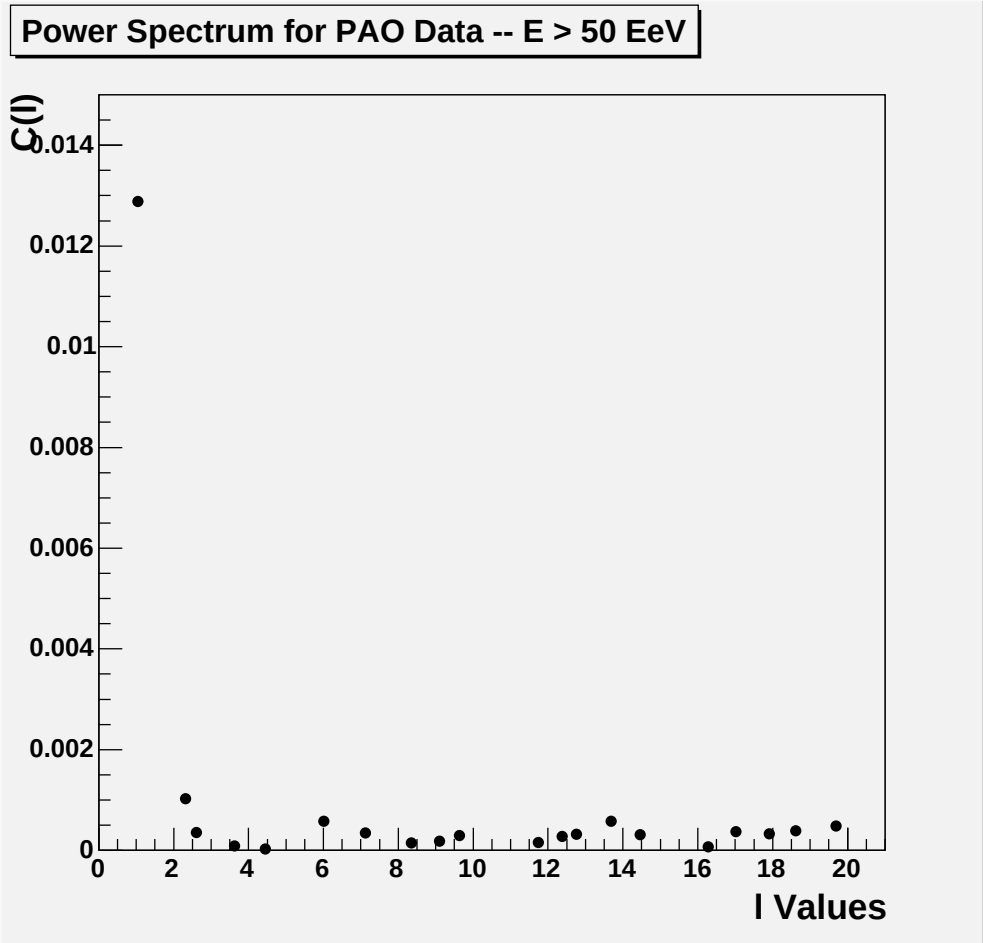


Figure 6.30: Power Spectrum for Post-GZK PAO Data

# Chapter 7: Summary

## 7.1 Conclusions and Discussion

The PAO hopes to provide the data we will need to ascertain the origins and compositions of the highest energy cosmic rays. By being the largest cosmic ray experiment ever built, the PAO will be the first to provide enough statistics to meaningfully analyze the arrival directions of these UHECR. In addition, the hybrid nature of the experiment will make it the first that can utilize the pros of both detection methods, while helping to alleviate the cons. These data, and the analysis thereof, will be groundbreaking in the study of cosmic rays of the highest energy.

A deeper understanding of the fields through which these charged particles travel is also integral to understanding their origins. By modeling different magnetic fields, we have discovered that the galactic magnetic field (GMF) provides the most significant bending of the trajectories of the particles, even when they travel through large expanses of space, since the extragalactic magnetic field is so much smaller.

By tracking particles through the GMF, we have discovered the relative probabilities of the detections of UHECR from various points on the celestial sphere. We have applied these probabilities to possible source distributions, in order to more realistically simulated what UHECR would look like if coming only from these sources. Calculating the angular power spectra of the events (both simulated and actually detected) has provided us with a powerful tool by which to analyze the

clustering of particles on the earth's surface.

Although the results obtained by calculating these power spectra look consistent with AGNs or nearby galaxies as source distributions, the extra dipole moment inherent to a half-sky exposure, such as the PAO currently has, adds in an uncertainty that fundamentally undermines the capabilities of large-scale anisotropy analysis. In the absence of clear point-like sources, construction of a detector in the Northern hemisphere will be necessary in order to know the origins of UHECRs with any confidence.

# References


[1] K. Greisen, End to the Cosmic-Ray Spectrum?, Phys. Rev. Lett. 16, 748 (1966).

[2] Z. T. Zatsepin and V. A. Kuz'min, Upper Limit of Spectrum of Cosmic Rays, JETP Lett. 4, 78 (1966).

[3] L. Anchordoqui, C. Hojvat, T. McCauley, T. Paul, S. Reucroft, J. Swain, A. Widom, arXiv:astro-ph/0305158, (2003).

[4] See N.W. Evans, F. Ferrer, S. Sarkar, Astropart. Phys. 17, 319 (2002).

[5] P. Kronberg, Rep. Prog. Phys. 57, 325 (1994).

[6] P. Sommers, Astropart. Phys. 14, 271 (2001).

[7] V. F. Hess, Observations in Low Level Radiation During Seven Free Balloon Flights, Phys. Z. 13, 1084 (1912).

[8] C. D. Anderson, Early Work on the Positron and Muon, Am. J. Phys. 29, 825 (1961).

[9] D. Griffiths, Introduction to Elementary Particles, John Wiley and Sons, Inc., (1987).

[10] P. Auger, Extensive Cosmic-Ray Showers, Reviews of Modern Physics 11, 288 (1939).

[11] P. Bassi, G. Clark, and B. Rossi, Distribution of Arrival Times of Air Shower Particles, Phys. Rev. 92, 441 (1953).

[12] J. Linsley, Evidence for a Primary Cosmic-Ray Particle with Energy 1020 eV, Phys. Rev. Lett. 10, 146 (1963).

[13] T. Hara, S. Kawaguchi, S. Mikamo, M. Nagano, K. Suga, G. Tanahashi, K. Uchino, and H. Akiyama, Acta Phys. Acad. Sci. Hung. 29, 361 (1970).

[14] H. E. Bergeson, G. L. Cassiday, T. W. Chiu, D. A. Cooper, J. W. Elbert, E. C. Loh, D. Steck, W. J. West, J. Boone, and J. Linsley, Measurement of Light Emission from Remote Cosmic-Ray Air Showers, Phys. Rev. Lett. 39, 847 (1977).

[15] J. Cronin, T. Gaisser, and S. Swordy, Cosmic Rays at the Energy Fontier,Sci. Amer. 276, 44 (1997).

[16] M. S. Longair, High Energy Astrophysics, Cambridge Univ. Press, (1981).

[17] The High Resolution Fly's Eye Collaboration, A Study of the Composition of Ultra High Energy Cosmic Rays Using the High Resolution Fly's Eye, Astrophys. J. 622, 910 (2005).

[18] E. Fermi, On the Origin of the Cosmic Radiation, Physical Review 75, 1169 (1949).

[19] L. O. Drury, Acceleration of Cosmic-Rays, Contemp. Phys. 35, 232 (1994).

[20] F. W. Stecker and M. H. Salamon, Photodisintegration of Ultra-High-Energy Cosmic Rays: A New Determination, Astrophys. J. 512, 521 (1999).

[21] G. Bertone, C. Isola, M. Lemoine, and G. Sigl, Ultrahigh energy heavy nuclei propagation in extragalactic magnetic

elds, Phys Rev D 66, 103003 (2002).

[22] L. Bergstrom and A. Goober, Cosmology and Particle Astrophysics, John Wiley and Sons, Inc., (1999).

[23] J. Wdowczyk, A. W. Wolfendale, and W. Tkaczyk, Primary Cosmic Gamma-Rays Above 1012 eV, J Phys A 5, 1419 (1972).

[24] J. Abraham, et. al. [Pierre Auger Collaboration], Nuclear Instrumentation and Methods, A 523, 50 (2002).

[25] See N.W. Evans, F. Ferrer, S. Sarkar, Astropart. Phys. 17, 319 (2002).

[26] V. F. Hess, Observations in Low Level Radiation During Seven Free Balloon Flights, Phys. Z. 13, 1084 (1912).

[27] M. Prouza, R. Smida, The Galactic magnetic field and propagation of ultra-high energy cosmic rays, A. and A., 410, 1 (2003).

[28] R. Beck, A. Brandenburg, A. Shukurov, D. Sukorov, ARAA (1996).

[29] T. Stanev, Astrophysical Journal, 479, 290 (1997).

[30] R. J. Rand, A.G. Lyne, MNRAS, 268, 497 (1994).

[31] J.P. Vallee, MNRAS, 264, 665 (1993).

[32] Y. Sofue, M. Fujimoto, ApJ, 265, 722 (1983).

[33] J.L. Han, J. Chin, Astron. and Astrophys., 2, 293 (2002).

[34] Review of Particle Physics, J. Phys., G 33, p.262 (July 2006).

[35] A.M. Hillas, Annual Review Astron. Astrophys.22, 425 (1984).

[36] E.O. Fluckiger, E. Kobel, D.F. Smart, M.A. Shea, Proc. 22nd Int. Cosmic Ray Conf. (Dublin), 3, 648 (1991).

[37] J.W. Bieber, P.A. Evenson, Z. Lin, Antarctic J., 27, 318 (1992).

[38] P. Lipari, T. Stanev, Proc. Int. Cosmic Ray Conf. (Rome) 1, 516 (1995).

[39] Veron-Cetty Catalogue, Veron & Cetty, Veron, 1998, VVII/207, http://cdsweb.u-strasbg.fr/cgi-bin/Cat?VII/207

[40] Tully-Fisher Catalogue, Tully 1988, VII/45, http://vizier.u-strasbg.fr/viz-bin/VizieR; “Nearby Galaxies Atlas”, R. Tully and J. Fisher, Cambridge Univ. Press (1987)

# Vita

Megan McEwen was born outside Chicago, Illinois, but raised in the Bay Area of Northern California. After attending high school in San Francisco, she moved to Manhattan to study at Columbia College in Columbia University. She obtained her Bachelor of Arts degree, with a major in astrophysics, in June, 1999.

Directly after graduating from college, she moved to Baton Rouge, Louisiana, to work with James Matthews on the Pierre Auger Observatory. While with Dr. Matthews, and the PAO, she has worked on flat-fielding fluorescence detectors, monitoring water levels inside Cerenkov detectors, atmospheric monitoring, and, most recently, anisotropy studies. She will receive her degree of Doctor of Philosophy in physics at the December, 2007 commencement.